Spring 2018

Lewis Acids in the Secondary Coordination Sphere for Kinetic Enhancement Toward Reduction of Nitrite

Kyle T. Burns
Western Washington University, kyletaylorburns@gmail.com

Lewis Acids in the Secondary Coordination Sphere for Kinetic Enhancement Toward Reduction of Nitrite

By

Kyle T. Burns

Accepted in Partial Completion
of the Requirements for the Degree
Master of Science

ADVISORY COMMITTEE

Chair, Dr. John D. Gilbertson

Dr. John M. Antos

Dr. Margaret L. Scheuermann

GRADUATE SCHOOL

Dr. Gautam Pillay, Dean

MASTER'S THESIS

In presenting this thesis in partial fulfillment of the requirements for a master's degree at Western Washington University, I grant to Western Washington University the non-exclusive royalty-free right to archive, reproduce, distribute, and display the thesis in any and all forms, including electronic format, via any digital library mechanisms maintained by WWU.

I represent and warrant this is my original work, and does not infringe or violate any rights of others. I warrant that I have obtained written permissions from the owner of any third party copyrighted material included in these files.

I acknowledge that I retain ownership rights to the copyright of this work, including but not limited to the right to use all or part of this work in future works, such as articles or books.

Library users are granted permission for individual, research and non-commercial reproduction of this work for educational purposes only. Any further digital posting of this document requires specific permission from the author.

Any copying or publication of this thesis for commercial purposes, or for financial gain, is not allowed without my written permission

Kyle T. Burns

June 1, 2018

Lewis Acids in the Secondary Coordination Sphere for Kinetic Enhancement Toward Reduction of Nitrite

A Thesis

Presented to

The Faculty of

Western Washington University

In Partial Fulfillment

Of the Requirements for the Degree

Master of Science

by

Kyle T. Burns

June 2018

Abstract

Metal complexes utilizing the redox non-innocent pyridinediimine ligand scaffold have been shown to form ligand centered radicals. The reduction potential of the ligand-based redox sites is effectively uncoupled from the secondary coordination sphere, allowing for installation of bioinspired secondary sphere motifs to tune reactivity, without attenuating the reductive ability of the metal center. This thesis aims to explore the utility of this ligand design by installing various functionality, reminiscent of those found in Nature, into the secondary coordination sphere, such as Lewis acidic residues, polarized active sites, and allosteric docking sites. Installation of a pendant benzo-15-crown-5 ether moiety, capable of encapsulating redox-inactive Na^+ ions, has been shown to entice corresponding counter ions in close-proximity to the metal center, with modest shifts in reduction potential (< 30 mV). The rate of reactivity on anions of interest was investigated, and in the case of NO_2^- reduction to NO, initial rate analysis revealed an acceleration in anion reduction attributed to encapsulating the Na^+ ion, which causes an increased effective concentration of NO_2^- near the metal center, primed for reactivity. Preliminary results of installing redox activity into a tripodal ligand scaffold have been presented. These novel ligand scaffolds have shown ligand centered redox activity when utilizing a redox-inactive Zn^{2+} metal. The synthesis of a family of "base-safe" pyridinediimine ligand scaffolds featuring the dibenzoylpyridine backbone have been presented. These ligands will be stable in the presence of organic superbases, which are necessary for the envisioned tandem catalytic cycle for the reduction of CO_2 to CO.

Acknowledgments

Research Advisor:	Dr. John D. Gilbertson
Thesis Committee:	Dr. John M. Antos
	Dr. Margaret L. Scheuermann
Research Group Members:	Audrey Cheung, Walker Marks, Doug Baumgartner, Wyatt Parks, Jade Porubek, and Kris Aguayo
Former Group Members:	Josh Ziegler, Yubin Kwon, Jillian Adams, Andrew Breuhaus-Alvarez, and Mayra Delgado
Instrument Technicians:	Dr. Hla Win-Piazza, Sam Danforth, and Charles Wandler
X-ray Crystallographer:	Dr. Lev Zakharov
Mossbauer:	Dr. Takele Seda
Financial Support:	National Science Foundation

Western Washington University Department of Chemistry

Table of Contents

page

List of Figures and Schemes

List of Tables and Equations

List of Experimental Figures

List of Abbreviations

Å	Angstrom
MeCN	Acetonitrile
Atm	Atmosphere
b15c5	benzo-15-crown-5 ether
CV	Cyclic Voltammogram
DCM	Dichloromethane
DNIC	Dinitrosyl Iron Complex
μ_{eff}	Effective Magnetic Moment
e^-	Electron
EtOH	Ethanol
FT-IR	Fourier Transform Infrared
h	Hour
δ	Isomer shift
MeOH	Methanol
nm	nanometer
NMR	Nuclear Magnetic Resonance
ORTEP	Oak Ridge Thermal Ellipsoid Plot
ppm	parts per million
*p*H	potential of hydrogen
H^+	Proton
PDI	Pyridinediimine
ΔE_Q	Quadrupole Splitting
THF	Tetrahydrofuran
NEt_3	Triethylamine
UV-Vis	Ultraviolet-Visable
V	Volts

Chapter 1 – Introduction

1.0 Small Molecule Activation

An active area of chemical research is small molecule activation, which typically targets abundant gases (H_2, N_2, CO_2, NH_3, etc.) or small polyatomic ions (NO_3^-, ClO_4^-, etc.) that are relatively unreactive under normal conditions to transform them to useful molecules.[1] The use of these molecules as synthons, synthetic starting materials, has applications in every aspect of chemical industry, including renewable energy (hydrogen storage, Fisher-Tropsch, Haber-Bosch, etc.), environmental protection (remediation of greenhouse gasses and environmental pollutants), and pharmaceuticals (chemical feed stocks).

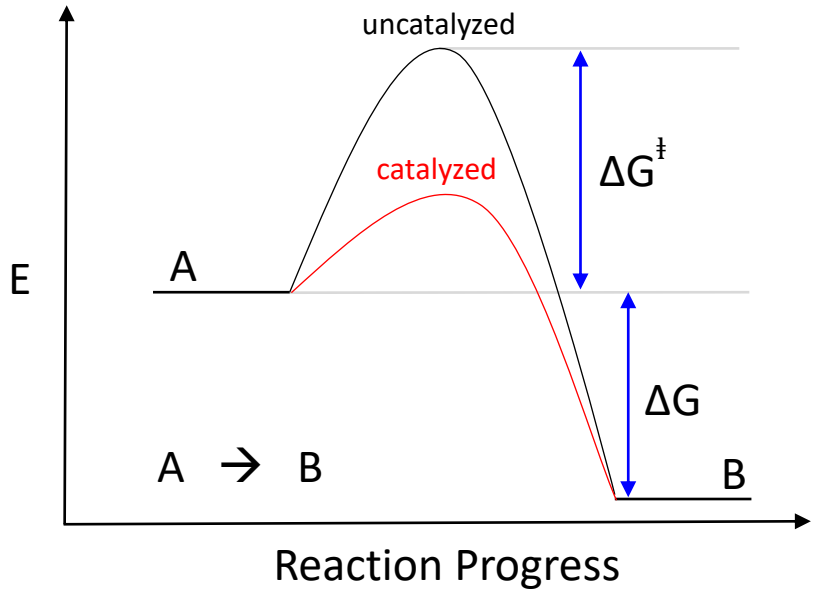

Figure 1.1 Generic reaction coordinate diagram of thermodynamically favorable chemical transformation.

The difficulty in performing many of these small molecule transformations lies in the high activation energy necessary to reach the transition state of the desired reaction. The use a

catalyst can lower this activation barrier, increasing the rate of transformation relative to the uncatalyzed reaction, as depicted above in Figure 1.1. Among current industrial methods, there are two main classes of catalysis, heterogeneous and homogeneous.

Heterogeneous catalysis occurs at the interface of two phases of matter, such as gas/solid or gas/liquid interfaces. Notable examples include; the Haber-Bosch process, in which N_2 and H_2 are transformed over a potassium promoted iron catalyst forming NH_3 for use as fertilizers;[2] or catalytic converters in cars, where toxic gaseous combustion products are passed over platinum-group metal catalysts to complete oxidation, such as CO to CO_2 which is no longer toxic.[3] Since heterogeneous catalysts are often solid-state structures, they can be difficult to characterize structurally, and their reactivity can be wildly different at various crystal facets and features, where single atom active site reactivity will differ from step edges, and so on.[4] These challenges make it difficult to finely tune these catalysts since local behavior deviates from the bulk solid behavior.

Homogeneous catalysis, on the other hand, is typically easier to study in a systematic manner, as catalysis occurs within the same phase. Most often both the catalyst and substrate are dissolved in a solvent, meaning both can be analyzed by solution phase-amenable techniques, such as UV-Vis or NMR, allowing for probing of chemical bonding, electronic structure, etc. Fine tuning and optimization of the catalyst through careful synthetic design is possible.[5] However, with a near limitless number of variables that could be included in this design taking inspiration from Nature, which has had billions of years to solve these same problems, seems an obvious place to start.

1.1 Metalloenzymes

In Nature, roughly 65% of catalytic transformations of small molecules are performed by metalloenzymes (proteins with transition metal active sites that can facilitate these chemical transformations under relatively mild conditions) under ambient temperature and pressure.[6] One example is nitrogenase, the enzyme responsible for the first step in nitrogen fixation, which is vital in Nature's life cycle. Nitrogenase-containing biological organisms can "fix" N_2 into usable forms, such as ammonia.[7] The importance of this transformation is apparent when considering how this is achieved industrially. The Haber-Bosch process (Fig. 1.2) is used by the chemical industry to synthesize ammonia, necessitating extremely high temperatures and pressures (300-550˚C, 100-300 atm).[8] This one process accounts for about 1.2% of the world's energy consumption in order to sustain the agricultural demand for fertilizer.[9,10]

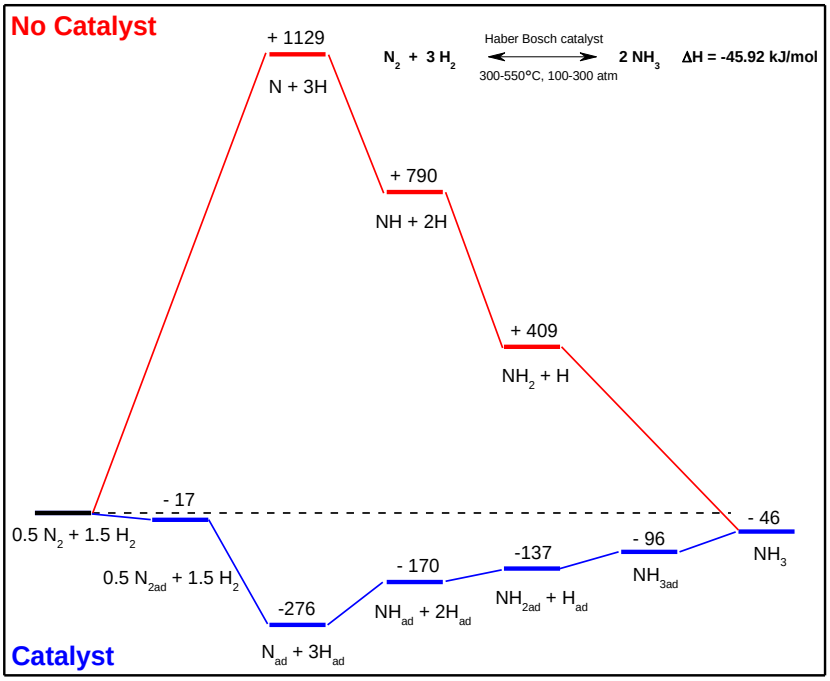

Figure 1.2 Energy diagram of Haber Bosch process. Energies displayed are in kJ/mol.

Organisms capable of this transformation can fix this inert gas into these usable forms under relatively mild conditions; atmospheric pressure, ambient temperature and biological pH. If a homogeneous catalyst was developed that could function under similar conditions, a major dent in the energy consumption of this one chemical process could be made.

In emulating metalloenzymes, it is important to understand the key features that can aid in the understanding of the specific tasks they are able to perform, from transportation of molecules; as in the case of hemoglobin (Hb) binding and transporting O_2,[11] to facilitation of redox chemistry; as in the case(s) of carbon monoxide dehydrogenase (CODHase)[12] and nitrite reductase (NiR).[13] The active site(s) of metalloenzymes are known to contain two microenvironments vital to catalytic function, known as the primary and secondary coordination sphere(s)[14] (Fig 1.3).

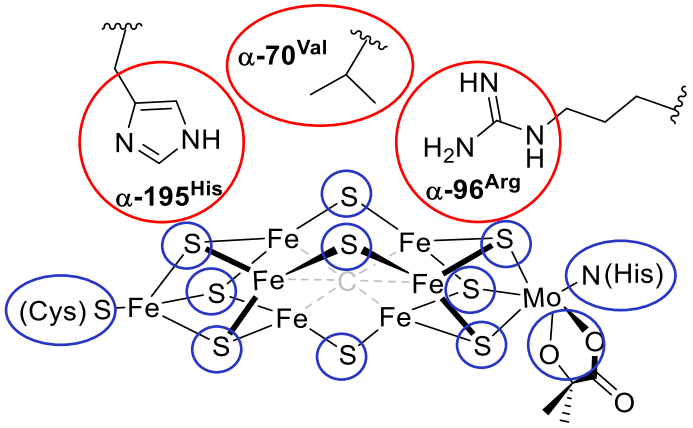

Figure 1.3 Active Site of FeMo-cofactor of Nitrogenase. Examples of primary and secondary coordination sphere shown in blue and red, respectively.

The primary coordination sphere (circled in blue, Fig. 1.3) is defined by the ligands or solvent molecules directly bound to the metal atom(s). The identity of these ligands are responsible for

the structural and spectroscopic characteristics of active sites, and can facilitate specific reactivity through their coordination geometries, including specific coordination of substrate binding (axial binding of O_2 on heme), and facilitation of fast electron transfer reactions through imposed "entatic" states ($Cu^{II/I}$ electron transfer in blue copper proteins).[15]

The secondary coordination sphere (circled in red, Fig. 1.3) is made up of groups in close proximity that interact with the primary sphere to tune the selectivity. These secondary sphere interactions can include, proximal protonated residues that can act as proton shuttles, hydrogen bond donors/acceptors that can serve to stabilize reactive intermediates, and or nucleophilic residues to facilitate bond cleavage/formation. The primary and secondary spheres are vital features of the overall function of a metalloenzyme.

1.2 Synthetic Model Systems

Due to the importance of the primary and secondary coordination sphere(s) in metalloenzymes, it is difficult to study and characterize the active site through isolation from the surrounding protein structure, as this compromises their reactivity and function.[16] These difficulties lead researchers to develop biomimics, synthetic metalloenzyme analogues, to aid in the understanding of these active sites.[17] Biomimetic compounds can supplement these investigations by exploring small pieces of the overall picture, and the design of these compounds aim to mimic metalloenzyme active sites in one of two ways, either structurally or functionally.

Structural mimics are often developed by bioinorganic chemists attempting to understand the native metalloenzyme active site by replicating its features as closely as possible, including

the identity of metal centers, bound ligands and secondary coordination sphere interactions, and can serve to reconcile structural data and investigate reaction mechanisms.[18] These complexes are typically easier to access synthetically than the native metalloenzyme, and are more easily characterized, giving insight into features of the native active site that are masked by the surrounding protein, such as structure or reaction intermediates. A comparison of the FeFe Hydrogenase active site and a structural mimic can be seen in Figure 1.4, the development of which helped to elucidate features of the native active site, an example being the structural change between the reduced (H_{red}) and oxidized (H_{ox}) forms of the active site during H^+ uptake and H_2 generation.[19] The binding of a hydridic species could not be determined through protein crystallography, as the size of these light atoms is on the order of the wavelength of the X-rays in the copper source, meaning the identity cannot be unambiguously determined.

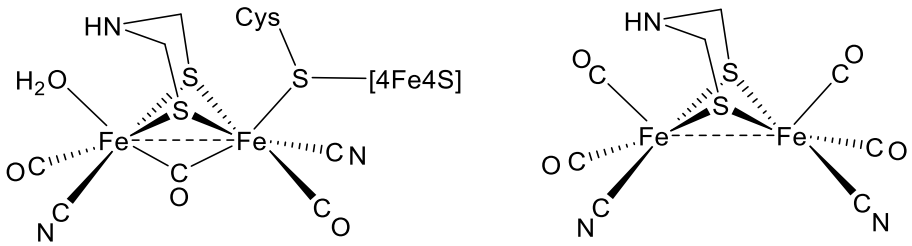

Figure 1.4 Metalloenzyme Structural Mimic. a) Hydrogenase Active Site and b) Structural Hydrogenase mimic developed by M. Y. Darensbourg et al.[20]

Functional mimics are the second type of biomimic commonly developed by inorganic chemists. The mimicry approach is slightly different as structural mimics are studied to determine information about the native active sites, functional mimics often aim to use features of the primary and secondary coordination sphere identified as vital for reactivity and incorporate similar, modular features into a complex design to perform a specific function or reaction.[21] Often

these functional mimics don't resemble the native active sites, and in some cases the metal centers can be vastly different from the native protein, leading to novel and exciting chemistry. Careful design of the ligand framework can allow for careful tuning of the primary and secondary coordination sphere(s) of these complexes to investigate how this affects reactivity.

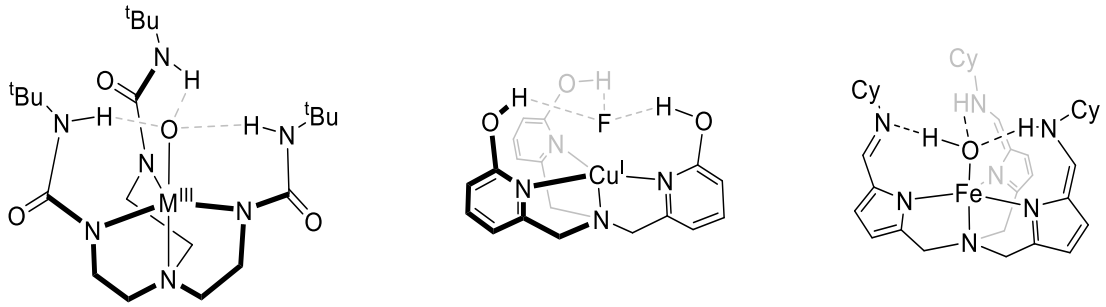

Figure 1.5 Metalloenzyme Functional Mimics. Examples of H-bond donor and acceptor ligand frameworks by a) Borovik,[21] b) Szymczak,[22] and c) Fout.[23]

Among common ligand scaffolds used in the field, there are two that are relevant to this work. The first is referred to as a tripodal ligand, examples of which can be seen in Figure 1.5. This tetra-dentate ligand binds with a trigonal bipyramidal geometry, where the central tertiary nitrogen occupies an axial position, and the three nitrogen "arms" binding in the equatorial positions, forming a chemical "tripod."[24] This serves to leave the other axial coordination site open for substrate binding. By modulating the groups extending from the equatorial nitrogens, functionality can be positioned into the secondary coordination sphere, tuning the reactivity and/or selectivity of a given complex. Common chemical motifs utilized in the secondary sphere of tripodal metal-ligand complexes are hydrogen bond donors/acceptors, commonly utilized by research groups such as Borovik (UC Irvine),[14,21] Szymczak (University of Michigan)[22] and Fout (University of Illinois).[23,25] There are a couple major limitations of this ligand however, such as

the small number of labile coordination sites (limiting substrate binding modes), and limited redox chemistry of these complexes, as oxidation states are limited to those available to the metal center.

A second common ligand scaffold, which much of the work described in this thesis is focused on, is known as the pyridinediimine (PDI) scaffold (Fig. 1.6). This PDI backbone consists of three pre-organized, coplanar nitrogens that form a tri-dentate ligand to bind a single metal center.[26] In five-coordinate metals, this leaves two open coordination sites, often with a square pyramidal geometry. With more than one accessible coordination site, there are more possibilities for substrate binding.

Pyridinediimine ligands are highly modular (similar to the tripodal scaffold) since it is possible to add functional groups that are synthetically feasible as the imine arms, allowing variation of the secondary coordination sphere of the complex. The main benefit of this ligand is the redox non-innocence of the pyridinediimine backbone. These ligands can participate in the storage and release of electrons, separate from the metal center, so the oxidation states of the metal do not necessarily limit the redox chemistry available to the complex.[27]

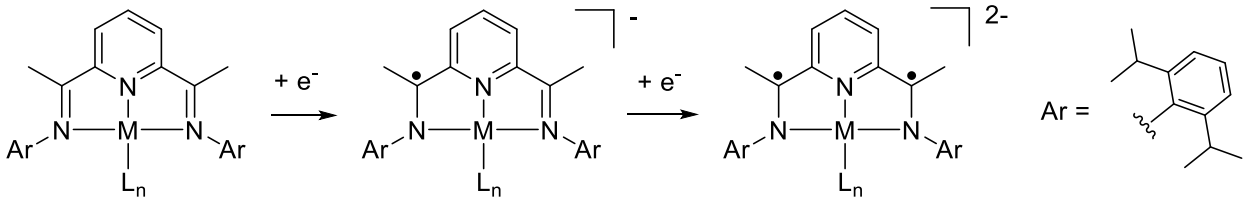

Figure 1.6 Redox-activity of pyridinediimine scaffold. Shown here are three (of the four) oxidation states available to these compounds.

Use of iron (II) pyridinediimine complexes in the Gilbertson group has allowed for the development of several interesting compounds through modulation of the imine arms (aka tuning the secondary coordination sphere), including an iron (II)-hydroxo moiety stabilized by a hydrogen bond in the secondary coordination sphere,[28] a series of highly reduced iron (II) carbonyl compounds with protonated amines in the secondary coordination sphere,[29] and even a ligand based reduction of CO_2 on an iron (II) center with subsequent release of the CO.[30]

1.3 Nitrogen Cycle

As mentioned earlier, the nitrogen cycle is a biological life cycle, describing how Nature takes nitrogen based small molecules from one form to another to be incorporated into biologically relevant nitrogen containing species, such as amino acids and nucleic acids.[31] The most abundant form of nitrogen is dinitrogen gas (N_2) and unfortunately, in its elemental form it is largely unusable for biological application. N_2 must first be converted into usable forms, so-called reactive nitrogen species, and this transformation requires a large amount of energy due to the high activation barrier of dinitrogen attributed to both the strength of the N,N triple bond (226 kcal/mol), and the large HOMO-LUMO gap (22.9 eV).[32] This chemical stability is precisely why N_2 is commonly used as an inert gas to perform chemical reactions under. It is extremely difficult to get N_2 to participate in chemical reactions, as the triple bond must first be broken. Nature has had a substantial amount time to work on this problem, and all the transformations from unreactive dinitrogen to reactive nitrogen species are collectively known as nitrogen fixation.

Abiotically, nitrogen can be fixed through nitrification when lightning strikes. This high energy reaction yields oxidized forms of nitrogen such as NO and NO_2, more commonly referred to as NO_x species, with can be further oxidized to NO_2^- and NO_3^-.[33] This pathway is believed to be the source of reactive nitrogen species early in earth's existence, and is still extremely important in the tropics where there are high incidents of lightning storms, estimated to produce approximately 5 Tg yr^{-1}.[34] In most of the world however, the dominant method of natural nitrogen fixation is through biotic pathways, estimated to produce 85 Tg yr^{-1}.[35]

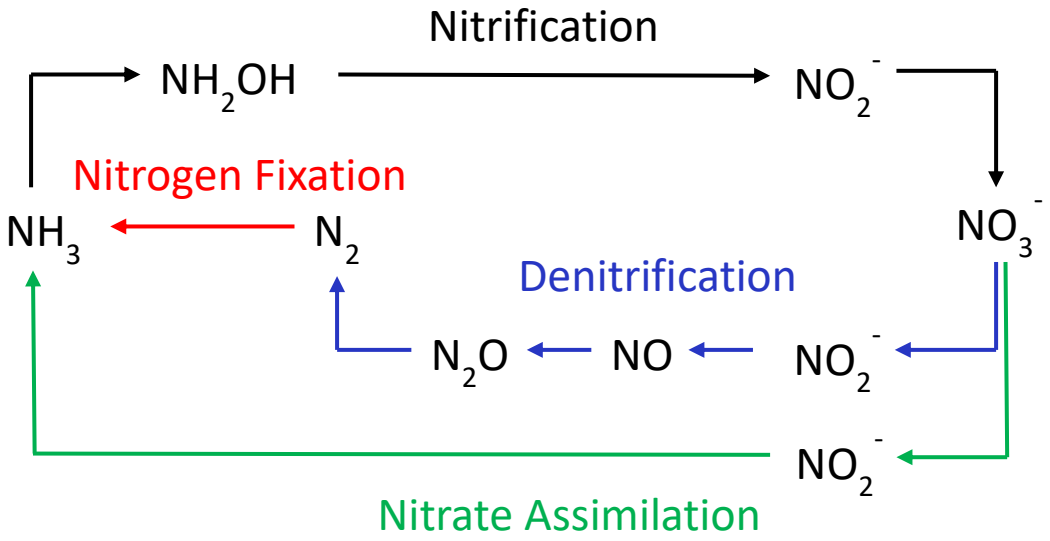

Figure 1.7 Nitrogen Cycle

Biotic nitrogen fixation can be broken into four main pathways, depicted in Figure 1.7.[36] The first of which, somewhat confusingly referred to as nitrogen fixation, is more aptly labeled ammonification (Fig 1.7, red). This is the process of reducing N_2 to ammonia (NH_3) or ammonium (NH_4^+), which are the readily usable forms of nitrogen.[37] Ammonification is carried out by diazotrophs, which are bacteria and cyanobacteria capable of fixing nitrogen for their use and

able to grow without the need of externally fixed nitrogen. Diazotrophs accomplish this through nitrogenase, a metalloenzyme containing either an iron-molybdenum, iron-vanadium or iron-iron active site, allowing them to anaerobically reduce N_2 into ammonia. Many plant species rely on absorbing excess ammonia/ammonium produced by the diazotrophs from the soil through their roots to incorporate where needed.

The second path is nitrification (Fig. 1.7, black), which consists of oxidizing the ammonia to nitrite (NO_2^-) and further into nitrate (NO_3^-). These steps are carried out by ammonia-oxidizing bacteria (AOB) through use of ammonia monooxygenase (AMO) and hydroxylamine oxidoreductase (HAO),[38] followed by nitrite-oxidizing bacteria (NOB) through use of nitrite oxidoreductase. AOB such as *Nitrosomonas* and NOB, such as *Nitrospira*, often dwell in soil or marine environments and carry out nitrification in order to couple the redox chemistry to ATP synthesis for the growth of the bacteria.[13]

The third path is nitrate assimilation (Fig 1.7, green), which is the uptake of nitrate and ammonium by plants and fungi for assimilation into amino acids. Nitrate is absorbed through the roots, where nitrate is first transformed to nitrite by nitrate reductase, and then converted to useable ammonium by nitrite reductase.[39]

The fourth path is denitrification (Fig. 1.7, blue), which is typically performed in anaerobic conditions to use the nitrogen containing species as electron acceptors in the absence of O_2. The conversion of NO_3^- back into N_2 makes use of multiple metalloenzymes, going from NO_3^- to NO_2^- (formed by nitrate reductase), NO_2^- to NO (formed by nitrite reductase), NO to N_2O (formed by

nitric oxide reductase) and finally to N_2O to N_2 (formed by nitrous oxide reductase), closing the nitrogen cycle.

1.4 Nitrite Reductase

The use of multiple, distinct metalloenzymes throughout the nitrogen cycle illustrates the importance of their understanding. However, development of synthetic methods to mimic the nitrogen cycle necessitates focus on individual steps rather than the entire pathway. To emulate and improve upon the features present in these metalloenzymes, each must be analyzed in detail. The denitrification pathway is desirable to study as nitrite and nitrate contamination of water sources is of great environmental concern,[40] and the work of this thesis will focus on one step in the denitrification, the reduction of NO_2^- to NO.

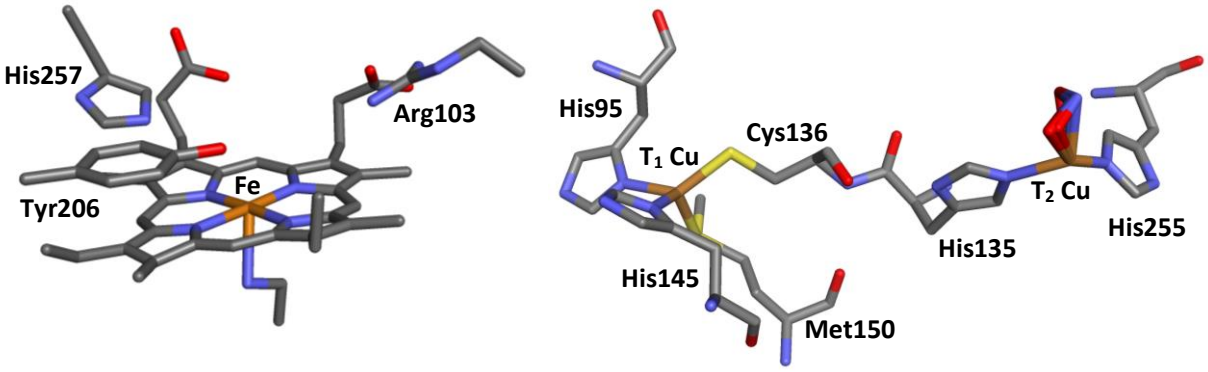

Figure 1.8 Nitrite reductases present in Nature, Cytochrome-cd_1 NiR active site (left)[41] and T_1 & T_2 copper NiR active site (right).[42]

Nature has developed a family of enzymes known as nitrite reductases (NiRs) to facilitate this transformation.[13,42] Two distinct forms are known, containing either iron in the form of heme cd_1 chromophores, or copper based active sites, seen in Figure 1.8. Both catalyze the one-

electron, two-proton reduction of nitrite to nitric oxide and water, eq. 1. The focus of this thesis involves iron, so further discussion will be on the iron containing NiR.

$$NO_2^- + 2H^+ + 1\,e^- \longrightarrow NO + H_2O \quad E° = 0.983\,V\,vs.\,NHE \qquad (\mathbf{1})$$

The exact mechanism of nitrite reduction by NiRs is unknown, as it isn't clear how nitrite binds to the metal. The majority of structurally characterized iron (II) porphyrin complexes favor the nitrogen-bound nitro form,[43–46] however DFT calculations have indicated that hydrogen bonding through a pendant histidine can help to overcome the energy difference between the nitro and nitrito isomer forms.[47] These data taken together indicate two likely mechanisms (Scheme 1.1).

Scheme 1.1 Two proposed mechanisms of biological nitrite reduction by FeNiR.

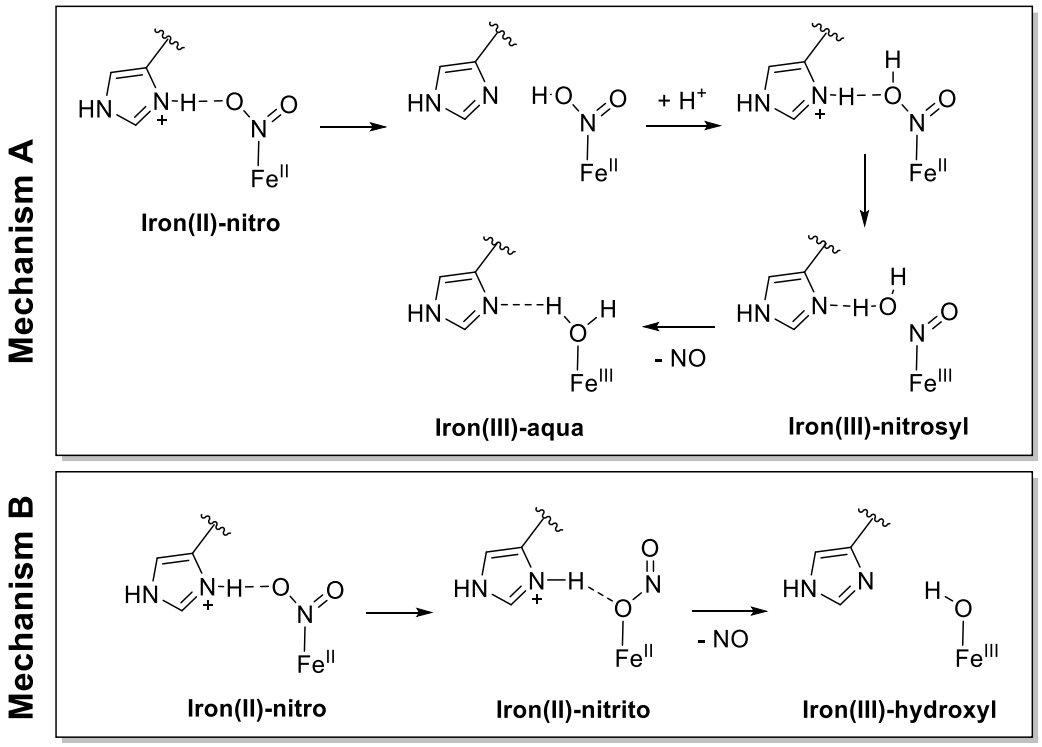

In mechanism A, nitrite first binds as an iron(II)-nitro, stabilized by a nearby protonated histidine residue. After two proton transfer steps, the nitrite is reduced, breaking the N-O bond, leaving an iron(III)-nitrosyl and forming water. After liberation of NO, the water binds to the iron to produce an iron(III)-aqua species. Mechanism B starts as the same iron(II)-nitro form, where the N-bound nitrite undergoes a linkage isomerization to form an O-bound iron(II)-nitrito stabilized by the previously discussed protonated histidine residue. Finally, the N-O bond is cleaved, liberating NO and leaving the NiR as an iron(III)-hydroxyl.

Scheme 1.2 Synthetic Model of Nitrite Reductase Developed by Fout et al.

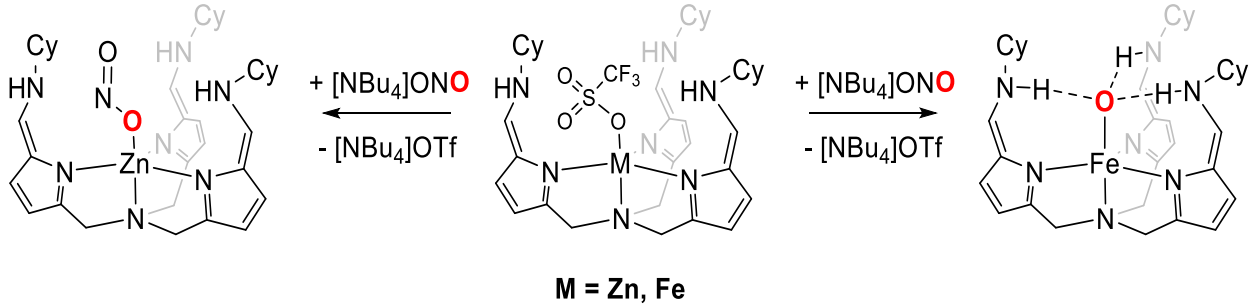

Through use of synthetic model systems, it may be possible to elucidate the mechanism of the native NiR active sites. An example of a model system developed by Fout et al. can be seen in Scheme 1.2. While a non-heme iron complex, it contains analogous motifs found in the NiR active ite, including an iron(II) center and hydrogen bond donors built into the ligand framework. This compound is proposed to reduce nitrite by forming an intermediate iron(II)-nitrito before forming the iron(III)-oxo stabilized by the pendant hydrogen bond donors. The iron(II)-nitrito was proposed based on the crystal structure of the redox-inactive zinc analogue, featuring he Zn-ONO nitrito binding mode. The iron analogue likely goes through this same binding mode during nitrite reduction, giving experimental evidence for Mech. B of the iron containing NiRs (Scheme 1.1).

1.5 Redox Inactive Metals

As briefly mentioned in Section 1.1, secondary coordination sphere interactions are extremely important in metalloenzyme function. In addition to hydrogen bonding interactions, the presence of Lewis acids is another important secondary sphere motif, most notably in the function of photosystem II (PSII), which facilitates the oxidation of water seen in eq. 2.[48]

$$2\ H_2O \longrightarrow O_2 + 4\ H^+ + 4\ e^- \quad E° = 1.23\ V\ vs\ NHE \qquad (\mathbf{2})$$

In the heart of PSII is the oxygen evolving complex (OEC), which consists of a tetra-manganese-oxo cluster, with a dicationic calcium ion (Figure 1.9a).[49] The presence of the Ca^{2+} ion is known to be necessary for its activity towards water oxidation.[50] This reaction is incredibly important as the oxygen formed by plants is vital for all aerobic organisms.

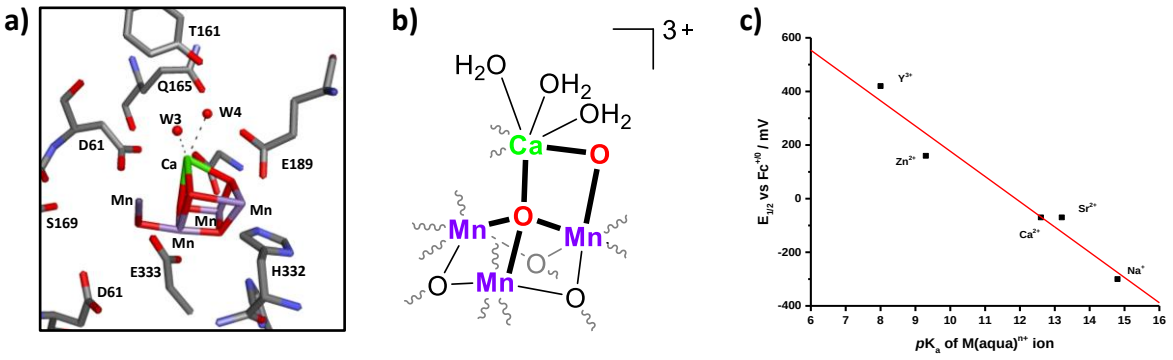

Figure 1.9 a) Active site of OEC in PSII (PDB 5V2C), b) Synthetic biomimic of the OEC featuring tri-manganese cluster and redox-inactive Lewis acids (ligand scaffold omitted for clarity, represented by grey bonds) and c) Redox dependence of tri-manganese cluster on Lewis acid, plot of $E_{1/2}$ vs pK_a of the $M(aqua)^{n+}$ ion, graph adapted from Agapie et. al.[51]

It is known that removal of the Ca^{2+} from the native enzyme, or exchange for other alkali metals (besides Sr^{2+}), completely shuts down the activity of the OEC.[52] To give further insight into the role of the Lewis acid in the native enzyme, a synthetic analogue featuring a Mn-cluster and various Lewis acids in the secondary sphere was developed, (Figure 1.9b).[51] By comparing the reduction potential to the pK_a of the M-OH_2 adduct, it was evident why only Ca^{2+} and Sr^{2+} allowed for the function of the OEC, (Figure 1.9c). The Lewis acidity of Ca^{2+} and Sr^{2+} serve to tune the reduction potential of the Mn active site, and lower the pK_a of the water molecule (W3) to facilitate water oxidation.

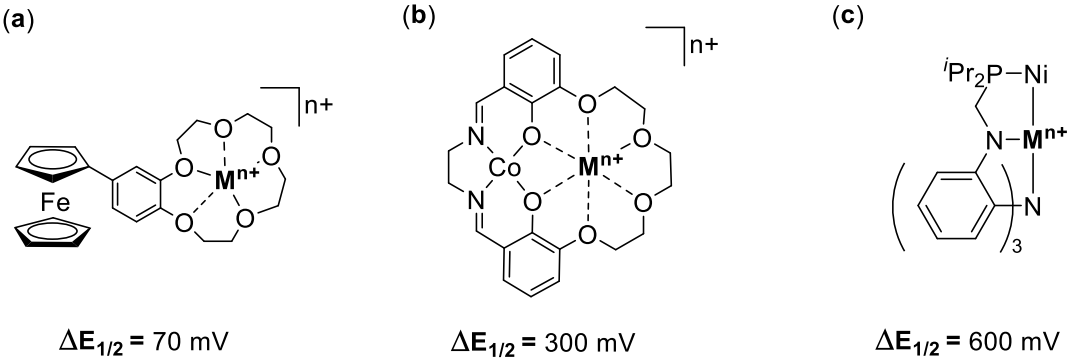

Figure 1.10 Examples of redox-active complexes featuring redox-inactive metals to tune reduction potential. $\Delta E_{1/2}$ values represent the shift in the metal-based reduction potential upon Lewis acid encapsulation.

Other synthetic systems featuring redox-inactive metals have been developed to tune the reduction potential of the redox-active site. Examples can be seen in Figure 1.10, including a benzo-15-crown-5 ether appended ferrocene (Fig 1.10a),[53] a cobalt-salen complex with a tethered crown ether motif (Fig 1.10b),[54] and a tripodal bimetallic metalloligand system (Fig 1.10c).[55] Each demonstrate a valuable utility of secondary sphere Lewis acid interactions, in that the reactivity of the complex can be tuned through interactions with redox-inactive metals.

1.6 Project Goals

The work discussed in this thesis can be split into four projects, each with specific aims and goals meant to investigate the features discussed above found in metalloenzymes; **a)** append a crown ether moiety to the iron-pyridinediimine ligand scaffold to position sodium salts into the secondary coordination sphere. This allows close-proximity to the highly reduced Fe-PDI core, increasing the effective concentration of these reactive anions near the metal site, emulating Lewis acid effects present in the OEC. **b)** Investigate the enhanced reaction kinetics of nitrite reduction by these $^{b15c5}Fe(PDI)(CO)_2$ complexes attributed to the effect of encapsulating the $NaNO_2$ close to the reactive metal site. **c)** Investigation into installing the redox non-innocent behavior of the pyridinediimine complexes into the tripodal ligand scaffolds. This can lead to redox active metal-ligand complexes where electron transfer reactions are no longer strictly limited to the available redox states of the metal, expanding on synthetic tools available in the development of biomimics. **d)** Design of new ligands amenable to a tandem catalyst system for CO_2 reduction using a renewable hydride source.

Chapter 2 – Synthesis and Characterization of Fe(PDI) Complexes.

2.0 Synthesis of Pyridinediimine Scaffolds (1-3)

As discussed in Chapter 1, the PDI ligand has been shown to be the foundation of many redox-active complexes.[56] By carefully choosing the pendant groups, it is possible to introduce a wide range of functionality into the secondary coordination sphere of the metallated PDI complexes. This chapter will discuss the synthesis of several iron (II) pyridinediimine complexes with varying secondary sphere functionality, providing hydrogen bonding donors, crown ethers for alkali metal ion binding and steric bulk.

Synthesis of the starting ligand (2,6-^{i}Pr-C_6H_3)N=C(CH_3)C_5H_3N(CH_3)C=O) (**1**), is typically formed with 2,6-diacetylpyridine and 2,6-diisopropylaniline which forms a Schiff-base via acid catalysis in methanol. Reducing the temperature to 273 K using an ice bath avoids the double addition product, leaving one free carbonyl for the installation of desired functional groups. The desired product is precipitated in the freezer overnight and filtered to yield ligand **1**.

Scheme 2.1 Generalized Schiff-Base synthesis of PDI ligands. Ar = 2,6-diisopropylaniline.

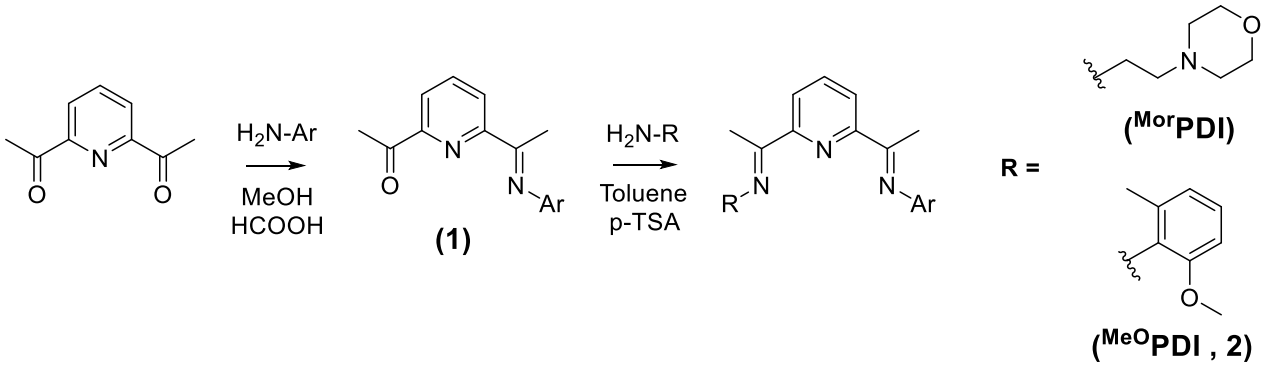

Scheme 2.1 depicts the syntheses of two representative asymmetric PDI ligands. Typical reactions are run on a 2.00 g scale of compound **1**, 0.02 g of para-toluene sulfonic acid (PTSA) as an acid catalyst and 1 eq. of the second amine or aniline arm which are added to a 250 mL round bottom flask along with a stir bar and 150 mL of toluene. The solution is refluxed overnight on a Dean-Stark apparatus to remove the water formed in the reaction to drive the reaction to completion. The solution is cooled to room temperature and the solvent is removed on a Roto-Vap. 40 mL of acetonitrile is added to the flask and placed in the freezer to precipitate out the desired product.

2.1 Synthesis and Characterization of Fe(^{L}PDI)X_2 (4FeX_2)

There are two ways of forming the metallated PDI complex. If the ligand featuring both imino functional groups was formed through use of a Dean-Stark apparatus, the ligand is brought into a N_2-filled glovebox and a slight excess of 1 eq. of either $FeCl_2$ or $FeBr_2$ is added to the ligand and dissolved in a 7:1 mixture of DCM/THF and stirred for 6 hours to form Fe(^{L}PDI)X_2 (Scheme 2.2) The solution is then filtered through celite to filter out unreacted metal and the solution is carefully layered with pentane to crystallize out the desired product.

Scheme 2.2 Metallation of PDI complexes to form Fe(^{L}PDI)X_2, (X = Cl^- or Br^-).

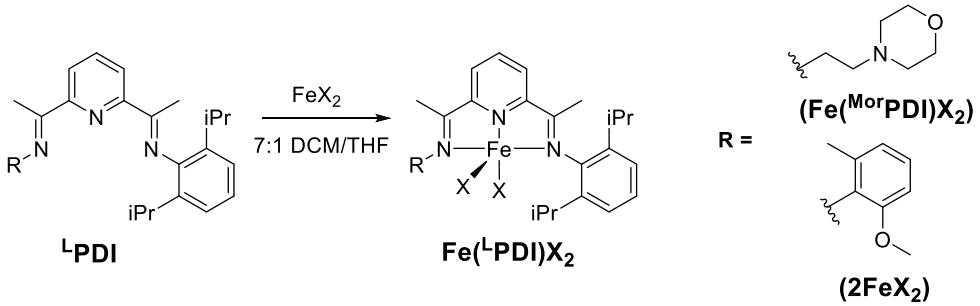

While this method of metalation is fairly straightforward, there are instances where the formation of the asymmetric ligand is not amenable to the Dean-Stark method, leading to difficulties in isolation of the final metallated product. In these cases, a metal templated Schiff-base condensation is employed for a single pot synthesis of the final Fe(^{L}PDI)X_2 product. For example, the installation the benzo-15-crown-5 ether arm into the secondary coordination sphere of the PDI complex is achieved using a metal templated approach. As much of the work presented in this thesis is on this complex, further discussion of the synthesis of these compounds will focus on synthesis of compound **3FeX$_2$**, though other complexes can be synthesized in a similar fashion.

By pre-coordinating compound **1** with FeX_2 (X = Cl^-, Br^-) in ethanol at 50˚C for 30 mins under an N_2 atmosphere, a new complex **1FeX$_2$** is quickly formed as evidenced by a color change from a yellow to pale blue solution. This indicates coordination with the FeX_2, which was originally a dark orange powder. This complex acts as a template for the Schiff-base to form between **1FeX$_2$** and the amine arm. One equivalent of 4'-aminobenzo-15-crown-5 ether, dissolved in minimal acetonitrile, is transferred by syringe into the flask and allowed to stir at 78˚C overnight under N_2 forming the desired product, **3FeX$_2$,** as seen in Scheme 2.3.

Scheme 2.3 Generalized Metal Templated Schiff-Base Condensation of Fe(^{b15c5}PDI)X_2.

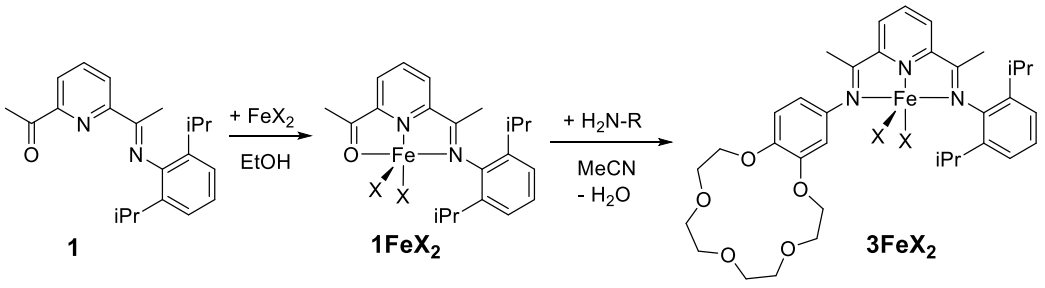

Depending on the identity of X, the solution becomes dark forest green (X = Cl^-) or cobalt blue (X = Br^-). The solvent is removed under vacuum and **3FeX₂** is purified inside an N_2-filled glovebox. The solid is re-dissolved in dichloromethane and filtered through celite. The resulting solution is layered with pentane to form X-ray quality crystals of the desired product. An ORTEP view of **3FeCl₂** can be seen in Figure 2.1.

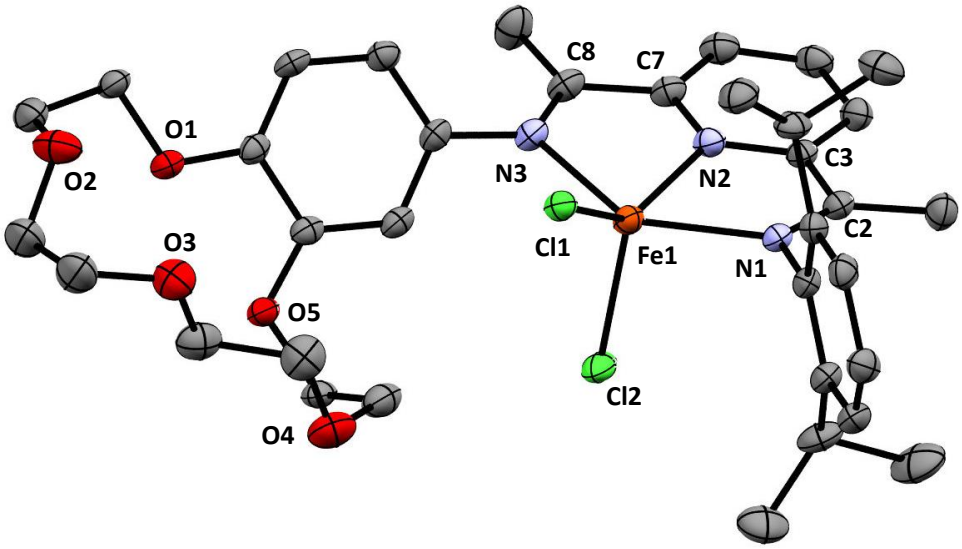

Figure 2.1 Solid state structure at 30% probability of **3FeCl₂**. The H atoms have been omitted for clarity. Selected bond lengths (Å): Fe(1)-N(1), 2.252(4); Fe(1)-N(2), 2.116(4); Fe(1)-N(3), 2.233(3); C(2)-N(1), 1.288(7); C(8)-N(3), 1.295(7); C(2)-C(3), 1.480(7); and C(7)-C(8), 1.486(8). Selected bond angles (˚): Cl(1)Fe(1)N(2), 140.3(1); and N(1)Fe(1)N(3), 144.2(1).

The Fe center is five-coordinate and to determine the coordination geometry, the τ_5 value is calculated according to eq. 3, where α and β are the two largest bond angles around the Fe center obtained from the crystal structure.[57]

$$\tau_5 = \frac{\beta - \alpha}{60°} \qquad \beta \geq \alpha \tag{3}$$

The values of τ_5 range from 0 (square pyramidal) to 1 (trigonal bipyramidal) as seen in Figure 2.2. A τ_5 = 0.065 in **3FeCl$_2$** corresponds to a distorted square pyramidal geometry, where the three nitrogens of the PDI backbone and one chlorine form the basal plane and the other chlorine lies in the apical position.

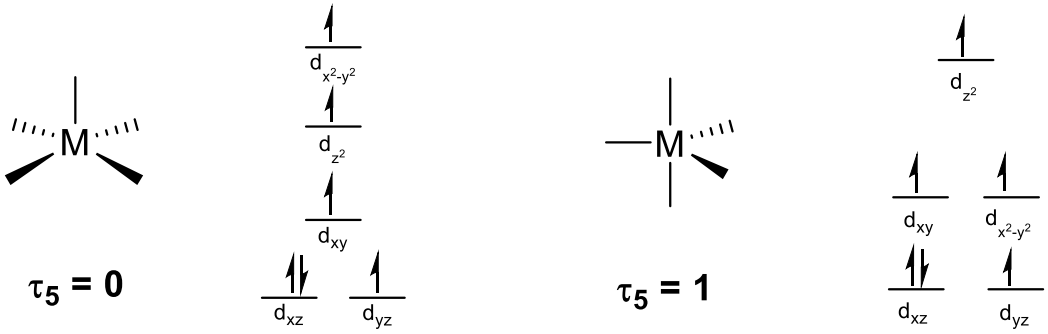

Figure 2.2 Geometry index (τ_5) of five-coordinate metal centers and d-orbital manifolds.

Fe^{2+} is a d^6 metal, meaning there are 6 electrons in the d-orbital manifold of the complex. As seen in Figure 2.2, five-coordinate Fe(II) compounds where the d-orbitals are filled according to Hund's rule lead to high spin Fe(II) complexes. In complexes with a square pyramidal geometry, this leads to paramagnetic species with 4 unpaired electrons (S = 2). Paramagnetic species can be difficult to analyze by NMR due to the local magnetic field generated by the unpaired electrons, causing peak broadening wide chemical shift ranges in the NMR spectrum. The spectral window must be set to a wider range, for instance from 100 ppm to -50 ppm, in order to capture the resonances of the compound. The ^{1}H NMR spectrum of **3FeCl$_2$** can be seen in Figure 2.3,

however there are no chemical assignments in this spectrum due to the difficulty in accurately assigning peaks of paramagnetic species.

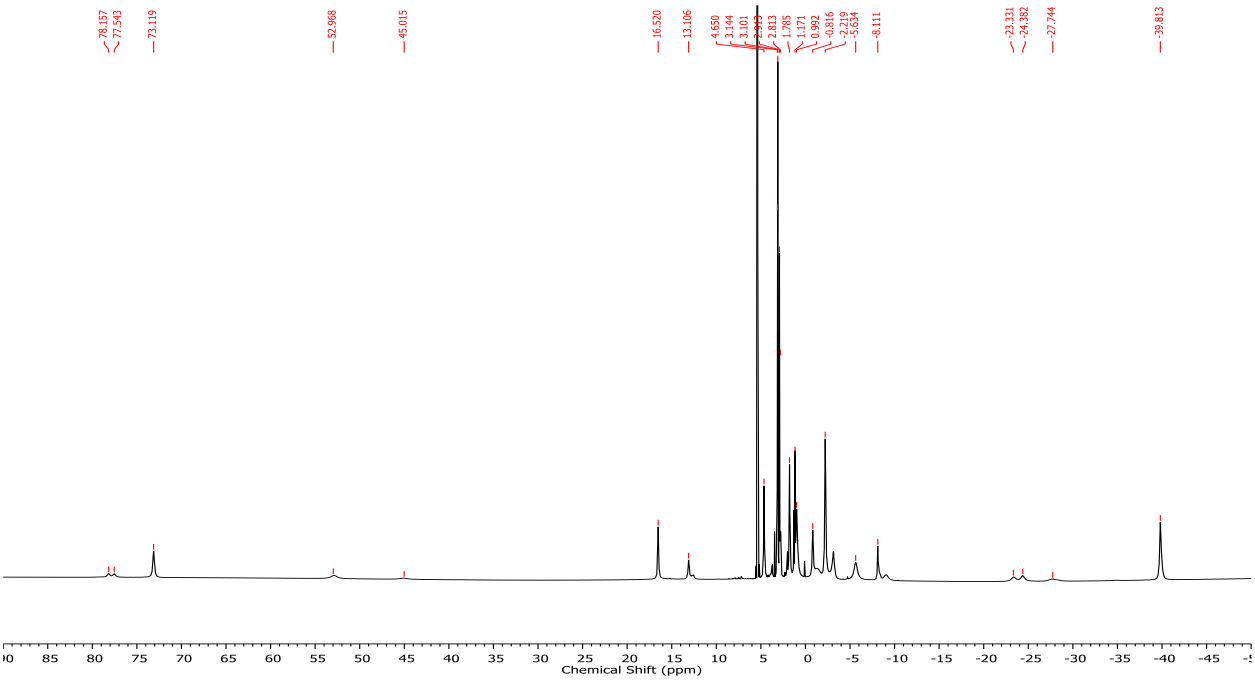

Figure 2.3 ^{1}H NMR Spectrum of **3FeCl$_2$** in CD_2Cl_2 (500 MHz).

Since these paramagnetic complexes are not easily characterized through NMR spectroscopy, other characterization techniques must be employed. Magnetic susceptibility measurements can be taken in the solid state via an Evans' balance,[58] and solution phase measurements can be obtained through NMR.[59] The measured μ_{eff} of **3FeCl$_2$** in the solid state and in solution are 5.74 μ_B and 5.43 μ_B respectively, consistent with a high spin Fe(II) complex (S = 2). In Fe complexes, Mössbauer spectroscopy can be utilized to measure properties of ^{57}Fe in the sample, giving insight into the oxidation state and symmetry about the Fe center. Room temperature zero-field Mössbauer parameters (Isomer shift, δ = 0.87(1) mm/s, Quadrupole

splitting, ΔE_Q = 1.49(2) mm/s) of **3FeCl$_2$** also confirm the assignment of a high spin Fe(II) center,[60] as seen in Figure 2.4.

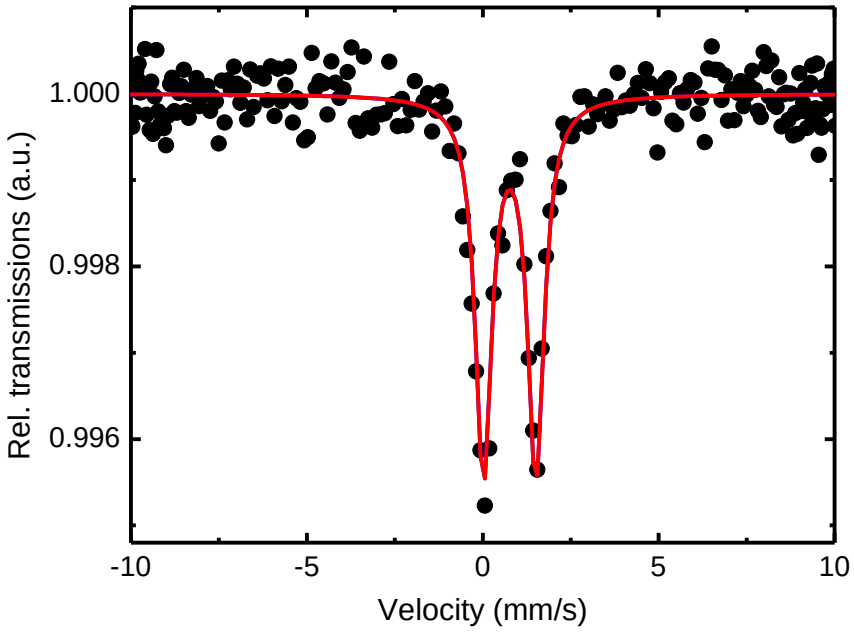

Figure 2.4 Room Temperature Zero-field Mössbauer Spectrum of **3FeCl$_2$**. Isomershift, δ = 0.87(1) mm/s, Quadrupole splitting, ΔE_Q = 1.49(2) mm/s, Line width, Γ = 0.56(3) mm/s.

2.2 Synthesis and Characterization of Fe(^{L}PDI)(CO)$_2$

With the Fe^{2+} center incorporated into the ligand backbone and the crown ether installed into the secondary coordination sphere, the backbone can be reduced by two electrons. This was achieved inside an N_2-filled glovebox by charging a Fisher-Porter tube with **3FeCl$_2$**, 5% w/w NaHg as a reductant, 15 mL of dichloromethane and a stir bar. The tube was sealed with a pressure gauge, brought outside of the box and pressurized with 40 psi CO. Stirring overnight, the Na^0 in the amalgam will reduce the backbone and precipitate out as Na^+ along with the halogens previously bound to the iron (eq. 4). These coordination sites are replaced by CO leading to the doubly reduced compound **3Fe(CO)$_2$**. The mirror symmetry of the pyridinediimine backbone

upon reduction is depicted through use of dotted lines, indicating conjugation through the backbone.[61]

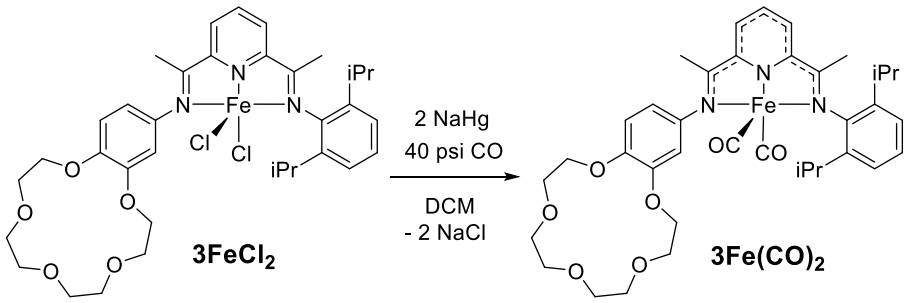

(**4**)

Following removal of the solvent and CO atmosphere, the compound is then re-dissolved in diethyl ether, filtered through celite and X-ray quality crystals were obtained by slow evaporation of the ether inside the glovebox. Solid state IR of this new compound shows two new peaks at 1948 and 1886 cm^{-1}, corresponding to ν_{CO}, seen in Figure 2.5.

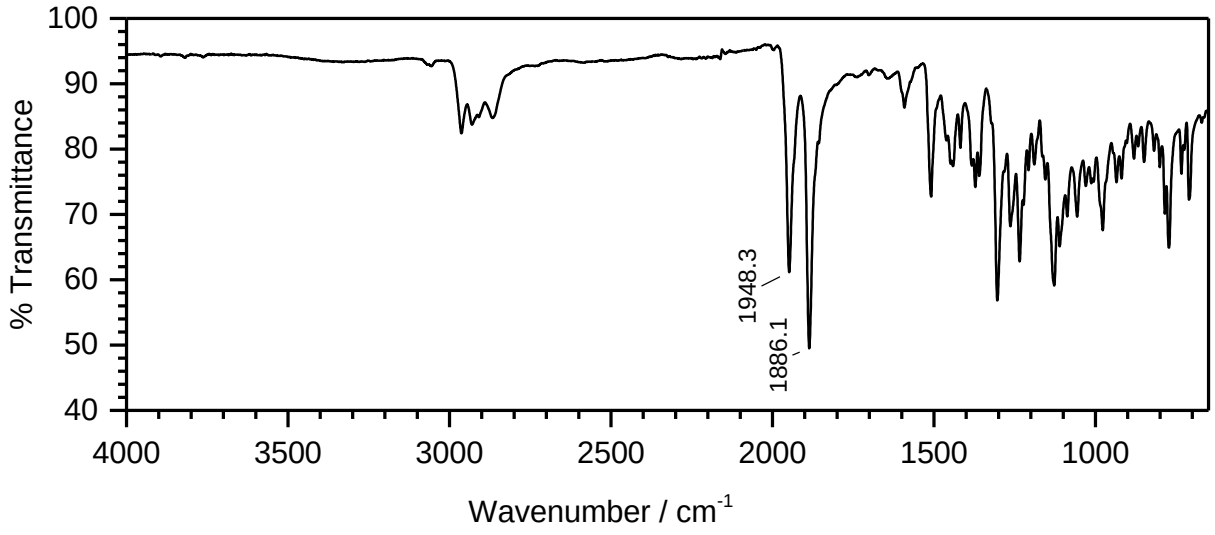

Figure 2.5 Solid FT-IR (ATR) Spectrum of **$3Fe(CO)_2$**.

Unlike **3FeCl$_2$** which was paramagnetic (S = 2), **3Fe(CO)$_2$** is diamagnetic (S = 0) as evidenced in the ^{1}H (Figure 2.6) and ^{13}C NMR (Figure 2.7), where the resonances of the newly diamagnetic compound are within a normal spectral window.

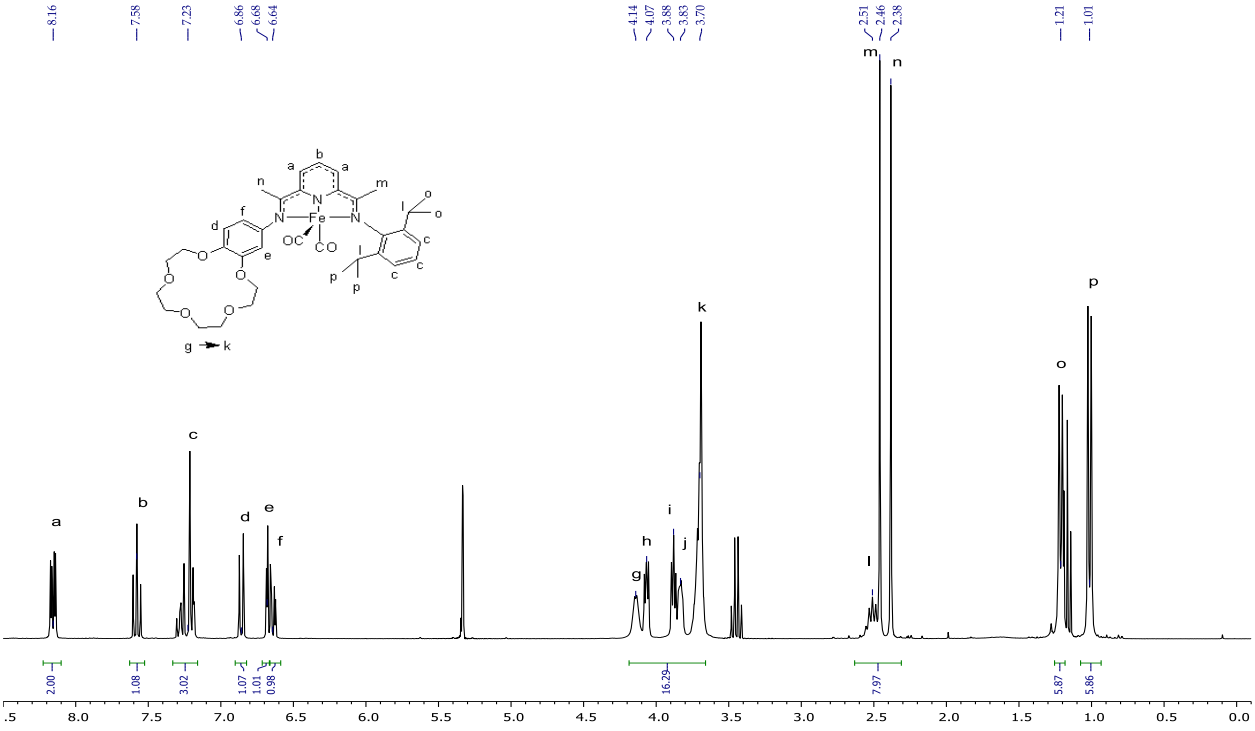

Figure 2.6 ^{1}H NMR Spectrum of **3Fe(CO)$_2$** in CD_2Cl_2 (500 MHz)

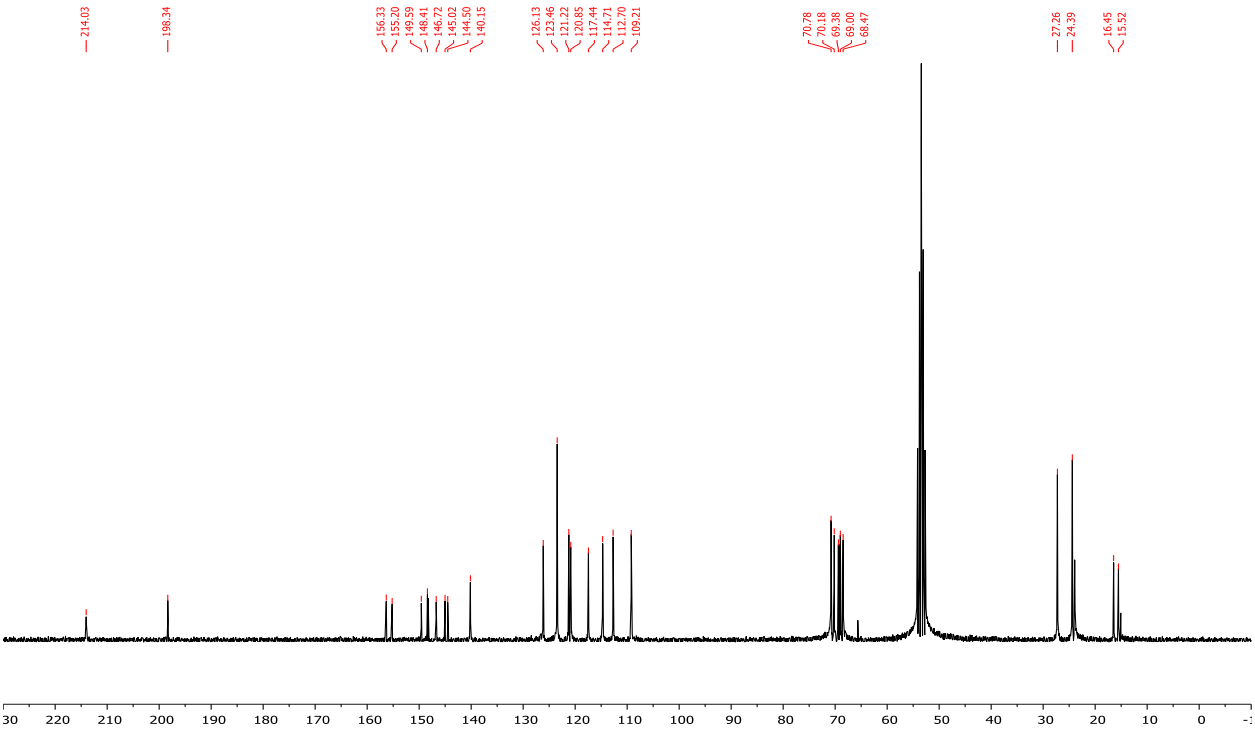

Figure 2.7 ^{13}C NMR Spectrum of **3Fe(CO)$_2$** in CD_2Cl_2 (125 MHz)

3Fe(CO)$_2$ is diamagnetic due to the CO ligands, which are known to be a strong field ligands.[62] The pi-back bonding of the Fe_{HOMO} into the CO_{LUMO} causes larger d-orbital splitting relative to the halogen case. This energy gap between the d-orbitals is larger than the electron pairing energy, and electrons fill the d-orbitals in a non-Hunds' rule fashion. The energetic cost to pair electrons is smaller than promotion to these higher energy orbitals. In Fe(II) complexes like these, this leads to diamagnetic compounds (S = 0).

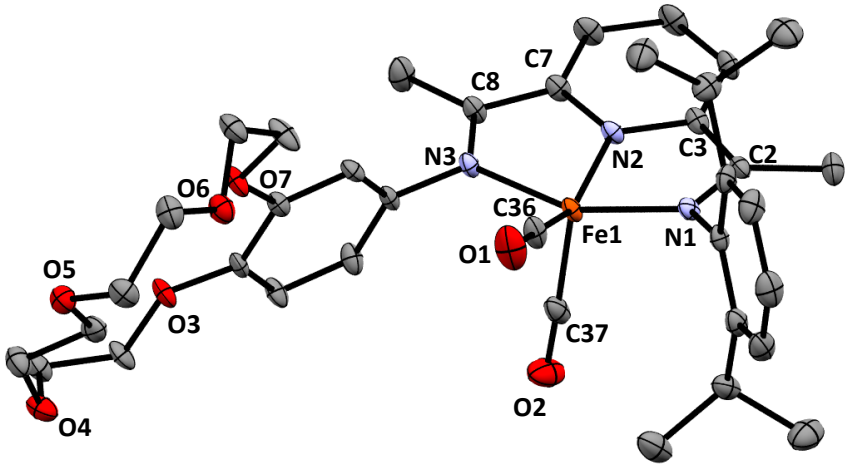

Figure 2.8 Solid state structure at 30% probability of **3Fe(CO)$_2$**. The H atoms have been omitted for clarity. Selected bond lengths (Å): Fe(1)−C(36), 1.784(5); Fe(1)−C(37), 1.783(5); Fe(1)−N(1), 1.943(4); Fe(1)−N(2), 1.840(3); Fe(1)−N(3), 1.936(4); C(2)−N(1), 1.324(5); C(8)−N(3), 1.325(5); C(7)−C(8), 1.427(6); and C(2)−C(3), 1.436(7). Selected bond angles (°): N(2)Fe(1)C(36), 148.4(2); N(1)Fe(1)N(3), 156.3(2); and C(36)Fe(1)C(37), 97.7(2).

An ORTEP view of the solid-state crystal structure of **3Fe(CO)$_2$** can be seen in Figure 2.8, where the iron center has maintained a five-coordinate square pyramidal geometry (τ_5 = 0.13), with the CO ligands replacing the halogens from the previous compound. One confirmation of the doubly reduced state of the ligand backbone can be observed by looking at the bond lengths of the C_{imine}-N_{imine} and C_{imine}-C_{ipso} bonds between the structure of **3FeCl$_2$** and **3Fe(CO)$_2$**. As previously mentioned, if the electron density in this doubly reduced state lies primarily on the PDI backbone, resonance through the backbone should cause the C_{imine}-N_{imine} bonds to elongate as they have lost some of their double bond character, where the C_{imine}-C_{ipso} bonds should contract a bit as they have gained some double bond character, as depicted in Figure 2.9.[61]

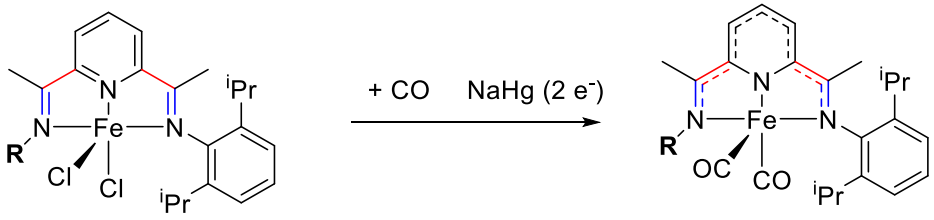

Figure 2.9 Mirror symmetry assignment of doubly reduced PDI backbone. C_{imine}-N_{imine} bonds (blue) elongate upon reduction while C_{imine}-C_{ipso} bonds (red) contract.

These bond lengths determined from the crystal structures of **3FeCl$_2$** and **3Fe(CO)$_2$** confirm the C_{imine}-N_{imine} bonds have elongated (1.295(7) Å and 1.288(7) Å → 1.325(5) Å and 1.324(5) Å), and the C_{imine}-C_{ipso} bonds have contracted (1.486(8) Å and 1.480(7) Å → 1.427(6) Å and 1.436(7) Å).

The room temperature Mössbauer spectrum of **3Fe(CO)$_2$** is shown in Figure 2.10. The given parameters (δ = - 0.088(3) mm/s and ΔE_Q = 1.126(4) mm/s) are consistent with a low spin Fe(II) center.[27] The lower relative isomer shift between **3FeCl$_2$** and **3Fe(CO)$_2$** is due to the electron withdrawing nature of the CO ligands, which causes the isomer shift of low spin Fe(II) complexes to show up closer to 0 mm/s, and these data are consistent with other reported low spin Fe(II) compounds.[29,30,63]

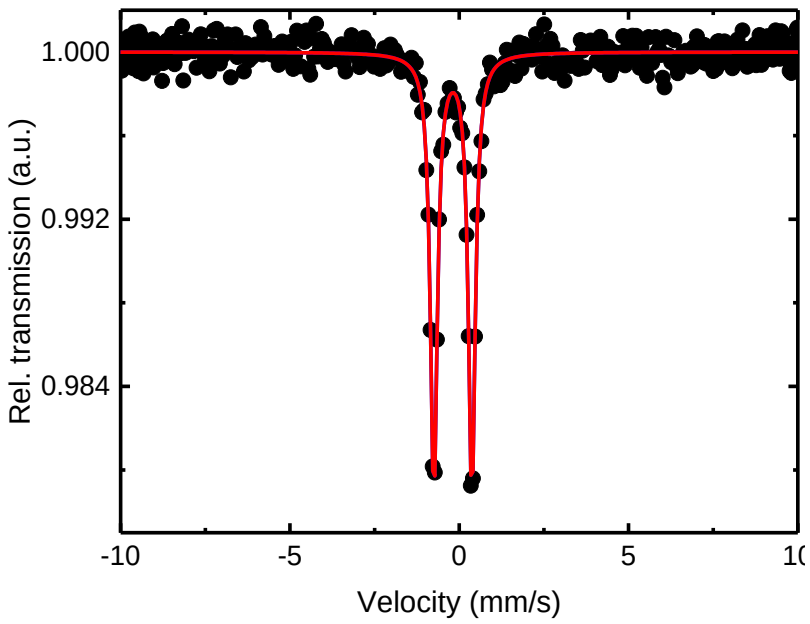

Figure 2.10 Room Temperature Zero-field Mössbauer Spectrum of **3Fe(CO)$_2$**. Isomershift, δ = - 0.088(3) mm/s, Quadrupole splitting, ΔE_Q = 1.126(4) mm/s, Line width, Γ = 0.246(5) mm/s.

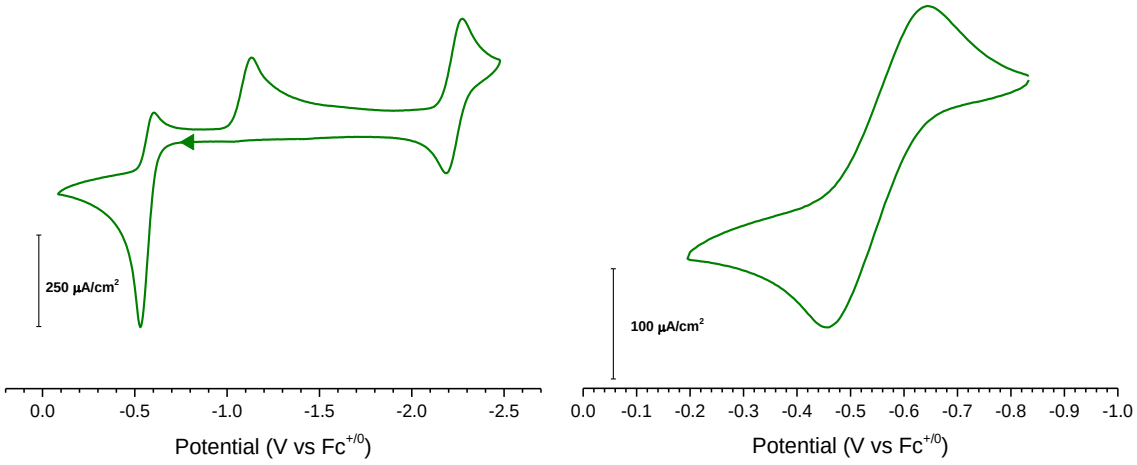

Figure 2.11 Cyclic Voltammograms of 1 mM **3Fe(CO)$_2$** in MeCN (left) and DCM (right). WE: glassy carbon, RE: Ag/$AgNO_3$, CE: Pt wire. 100 mM $TBAPF_6$.

Electrochemical studies of **3Fe(CO)$_2$** are consistent with other FePDI complexes, showing three electrochemical events in acetonitrile (Figure 2.11, left). The open circuit potential of

3Fe(CO)$_2$ lies at -0.78 V vs $Fc^{0/+}$, and running the potential positive shows an oxidative event centered at -0.53 V. In acetonitrile this event is irreversible, likely due to coordination of MeCN post-oxidation. This new complex is structurally dissimilar and upon the return sweep, is more difficult to re-reduce, giving rise to the reduction event centered at -1.15 V. When electrochemical analysis is run in non-coordinating solvents like dichloromethane, the oxidation event becomes fully reversible (Figure 2.11, right). Scanning further negative, there is a fully reversible reductive event at -2.20 V vs $Fc^{0/+}$, assigned to a reduction by a third equivalent of electrons onto the ligand backbone. These data are consistent with previously reported FePDI complexes.[63]

2.3 Synthesis and Characterization of [Fe(^{b15c5}PDI)$(CO)_2$Na][X] (X = PF_6^-, BPh_4^-)

With the empty crown complex synthesized and characterized, we moved onto encapsulating sodium salts with various anions to probe the hypothesis that allosteric-like docking could facilitate reactivity by positioning the anion close to the iron center. As a baseline, encapsulation started with $NaBPh_4$, as BPh_4^- is a non-coordinating, relatively unreactive anion in which we could probe the property changes in **3Fe(CO)$_2$** caused by encapsulation of the Na^+ in the crown ether. $NaPF_6$ was also chosen for the same reasons, however discussion will focus on the BPh_4^- salt ($NaPF_6$ data are included in the experimental). Typical encapsulation experiments were performed by charging a scintillation vial with **3Fe(CO)$_2$** and the Na^+ salt in acetonitrile, then stirring overnight. The solvent was removed under vacuum, the solid was re-dissolved in dichloromethane and filtered through celite to remove the excess salt. X-ray quality crystals were obtained by layering pentane on a saturated solution of **[3Fe(CO)$_2$Na][BPh$_4$]** in DCM.

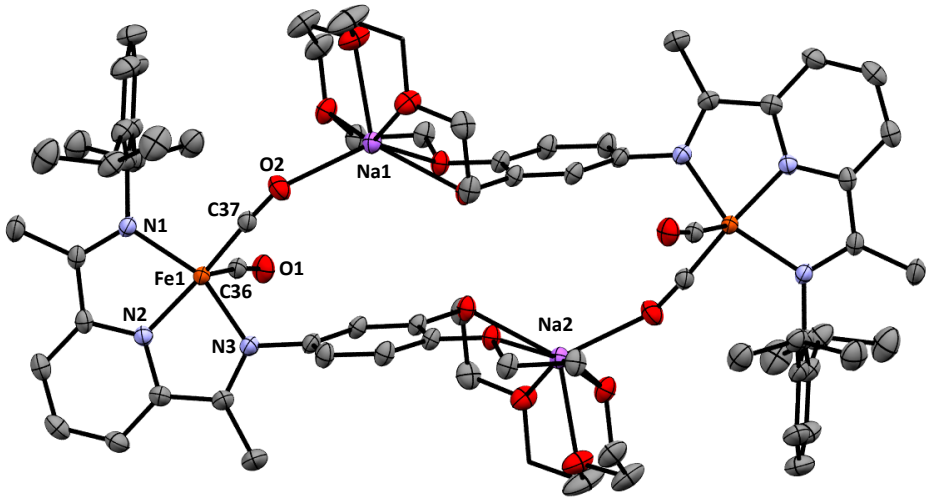

Figure 2.12 Solid state structure of symmetric unit at 30% probability of **[3Fe(CO)2Na][BPh$_4$]**. The H atoms and BPh_4^- counter ions have been omitted for clarity. Selected bond lengths (Å): Fe(1)−C(36), 1.776(3); Fe(1)−C(37), 1.770(2); Fe(1)−N(1), 1.966(2); Fe(1)−N(2), 1.847(2); Fe(1)−N(3), 1.945(2); C(2)−N(1), 1.323(2); C(8)−N(3), and

1.324(2). Selected bond angles (°): C(36)Fe(1)C(37), 97.1(1); N(2)Fe(1)C(37), 152.35(9); and N(1)Fe(1)N(3), 155.42(7).

The ORTEP view of the solid state crystal structure of **[3Fe(CO)$_2$Na][BPh$_4$]** is given in Figure 2.12. The compound crystallizes as a centrosymmetric dimer where the equatorial CO ligand of one molecule interacts with the encapsulated Na^+ of the other. The distorted square pyramidal geometry around the iron center is maintained (τ_5 = 0.05).

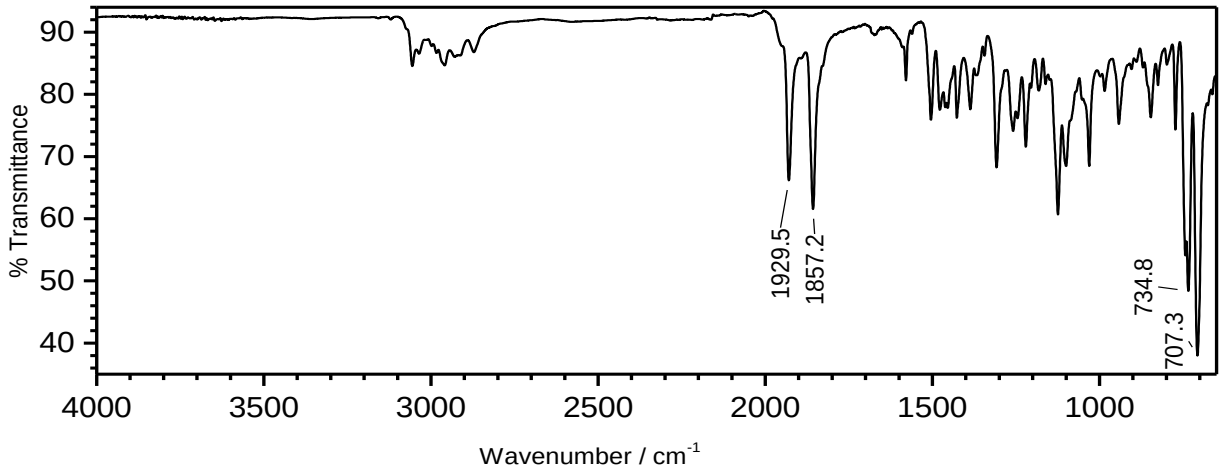

Figure 2.13 Solid FT-IR (ATR) Spectrum of **[3Fe(CO)$_2$Na][BPh$_4$]**.

The interaction between the Na^+ and CO shifts the ν_{CO} to lower wavenumbers (1929 and 1857 cm^{-1}, Figure 2.13), however this is a solid-state phenomenon, as the dimer does not exist in solution. The CO peak in the ^{13}C NMR (see experimental, E22) shows up at 215 ppm, identical to the CO in the empty compound. Additionally, the solution phase IR spectra shown in Figure 2.14 show the ν_{CO} do not shift upon Na^+ encapsulation.

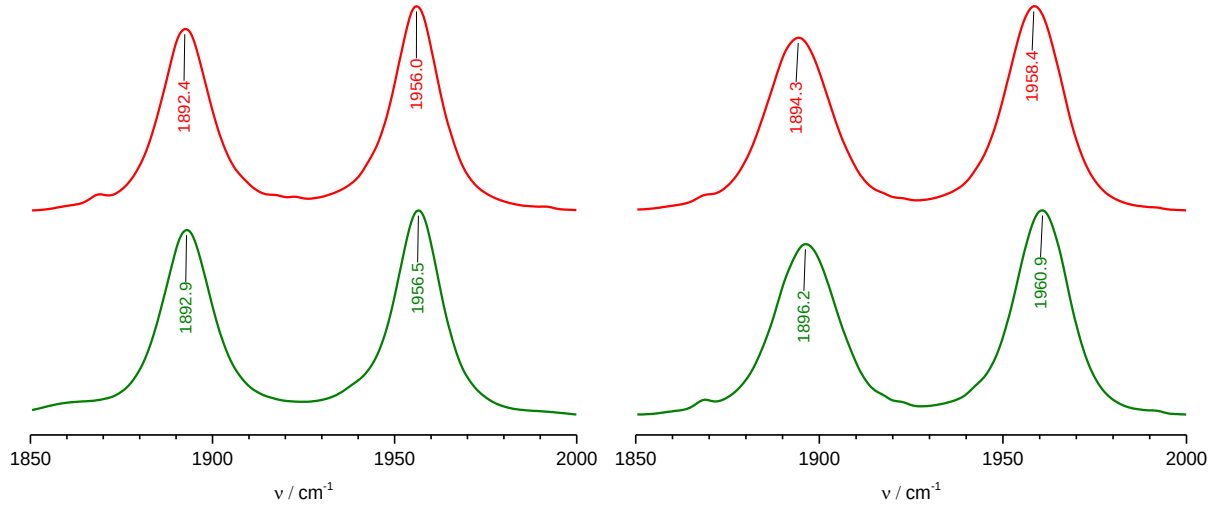

Figure 2.14 Solution FT-IR measurements of 1 mM **$3Fe(CO)_2$** (green) and 1 mM **$[3Fe(CO)_2Na][BPh_4]$** (red) in MeCN (left) and DCM (right) showing ν_{CO} stretches.

Several other alkali metal salts were also encapsulated, including $NaPF_6$, $NaBH_4$, and $NaNO_2$. The ν_{CO} stretches of these complexes can be seen in Table 2.1, where very slight shifts indicate little effect on the ν_{CO} bands of the bound CO.

Table 2.1 Solid and solution phase ν_{CO} IR stretches.

Compound	ν_{CO} / cm^{-1} (solid)	ν_{CO} / cm^{-1} (solution, MeCN)
$3Fe(CO)_2$	1948, 1886	1957, 1893
$[3Fe(CO)_2Na][PF_6]$	1937, 1868	--
$[3Fe(CO)_2Na][BPh_4]$	1929, 1857	1956, 1892
$[3Fe(CO)_2Na][BH_4]$	1954, 1873	--
$[3Fe(CO)_2Na][NO_2]$	1949, 1884	1957, 1893

The Mössbauer spectra of **$[3Fe(CO)_2Na][BPh_4]$** is seen in Figure 2.15. The Mössbauer parameters (δ = - 0.077(5) mm/s, and ΔE_Q = 1.339(9) mm/s) indicate little change to the electronics or geometry around the Fe(II) center after encapsulation.

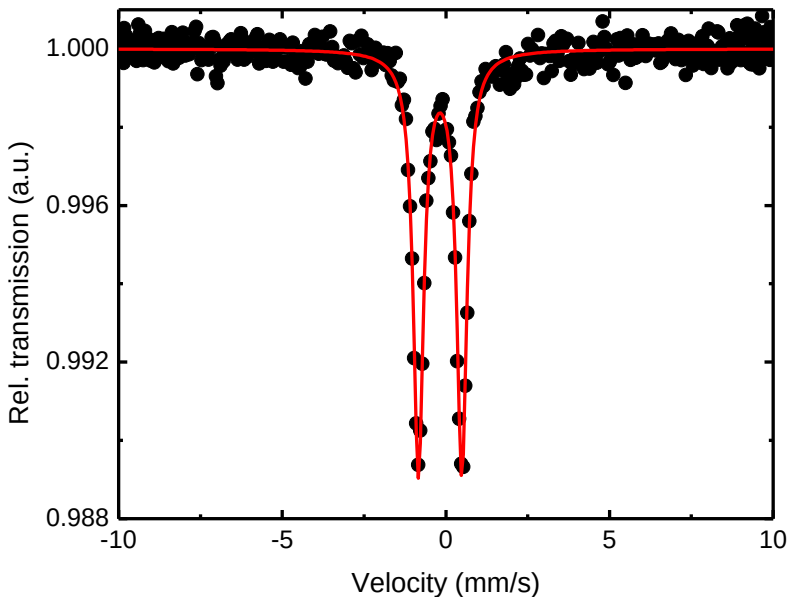

Figure 2.15 Room temperature zero-field Mössbauer spectrum of **[3Fe(CO)$_2$Na][BPh$_4$]**. Isomershift, δ = -0.077(5) mm/s, Quadrupole splitting, ΔE_Q = 1.339(9) mm/s, Line width, Γ = 0.39(1) mm/s.

Figure 2.16 shows the comparative cyclic voltammograms of empty and Na^+ encapsulated complexes, and Table 2.2 shows selected electrochemical data of these encapsulated compounds, where the modest electrochemical shifts ($\Delta E_{1/2} \approx 30$ mV) indicate little effect on the electrochemical behavior of the FePDI backbone. The electrochemical and liquid IR data taken together indicate that the chemical potency of the FePDI is effectively unattenuated upon encapsulation of the alkali metals.

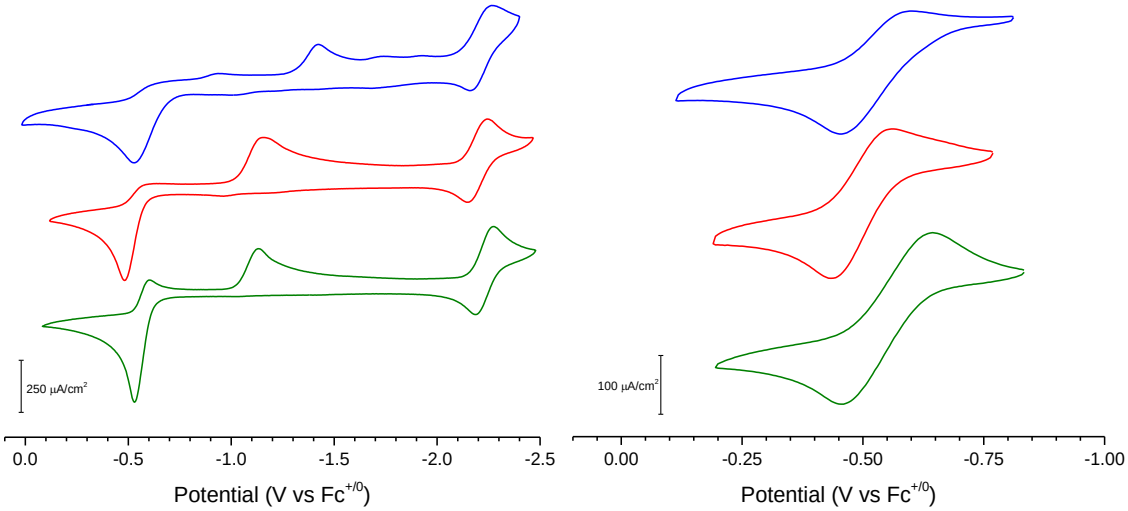

Figure 2.16 Cyclic Voltammograms of 1 mM **$3Fe(CO)_2$** (green), 1 mM **$[3Fe(CO)_2Na][PF_6]$** (red) and 1 mM **$[3Fe(CO)_2Na][BPh_4]$** (blue) in MeCN (left) and DCM (right). WE: glassy carbon, RE: $Ag/AgNO_3$, CE: Pt wire, 100 mM $TBAPF_6$.

Table 2.2 Electrochemical reduction potentials of **$3Fe(CO)_2$** complexes, potentials are referenced vs. $Fc^{+/0}$.

Compound	$E_{1/2}$ / V (MeCN)	$\Delta E_{1/2}$ / mV (MeCN)	$E_{1/2}$ / V (DCM)	$\Delta E_{1/2}$ / mV (DCM)
$3Fe(CO)_2$	-2.200	--	-0.523	--
$[3Fe(CO)_2Na][PF_6]$	-2.238	38	-0.498	25
$[3Fe(CO)_2Na][BPh_4]$	-2.231	31	-0.492	31
$[3Fe(CO)_2Na][NO_2]$	-2.230	30	-0.513	10
$[3Fe(CO)_2K][PF_6]$	-2.221	21	-0.501	22
$[3Fe(CO)_2K][BPh_4]$	-2.200	0	-0.499	24

2.4 NMR Salt Titration Experiments

In the ^{1}H NMR spectrum of **$[3Fe(CO)_2Na][BPh_4]$**, Figure 2.17, the resonances associated with the crown ether are shifted slightly downfield upon encapsulation of the sodium salt. The regions of the crown ether CH resonances are from 7.0 → 6.5 ppm & 4.2 → 3.6 ppm. Some electron density in the oxygens of the crown ether is donated to the Lewis acid to form the [Na^+-crown] adduct, thereby deshielding the nearby ^{1}H resonances.

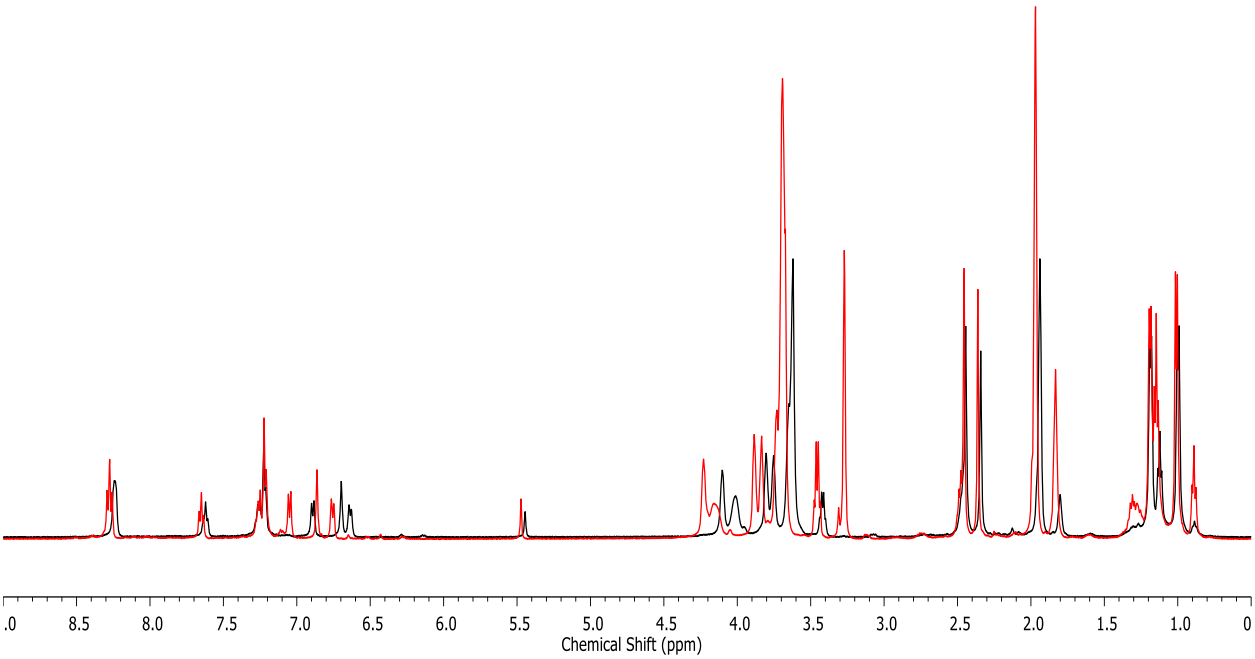

Figure 2.17 Overlaid ^{1}H NMR of **$3Fe(CO)_2$** (black) and **$[3Fe(CO)_2Na][BPh_4]$** (red)**.**

The magnitude of the shift can be used to probe the equilibrium binding between the Na^+ and the crown complex (eq. 5) through ^{1}H NMR salt titration experiments, where varying equivalents of Na^+ were added to the crown complex to obtain a binding isotherm.

$$\text{crown} + Na^+ \longleftrightarrow [\text{Na-crown}]^+ \qquad (5)$$

From these binding isotherms, association constants are extracted using an iterative fitting program.[64] These association constants give insight into the solution behavior of the Na^+-crown adducts, and how strongly the Na^+ is encapsulated into the crown ether. Results from the salt titration of $NaBPh_4$ into **3Fe(CO)$_2$** can be seen in Figure 2.18.

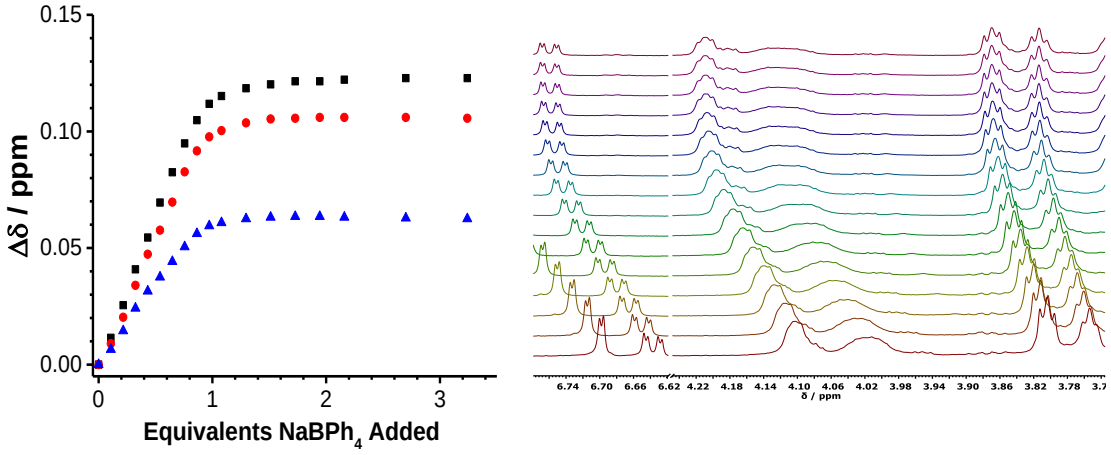

Figure 2.18 ^1H NMR of $NaBPh_4$ and **3Fe(CO)$_2$** in CD_3CN. C-H resonances associated with binding isotherms reference the chemical shift of the empty crown (6.64 ppm = blue; 4.10 ppm = red; 3.78 ppm = black). The spectra plotted correspond to 0 eq. (bottom) and 3.5 eq. $NaBPh_4$ (top).

The results from the $NaBPh_4$ salt titration experiment is representative of typical salt titration experiments, and additional binding isotherms and ^1H NMR spectra can be seen in Section 7.4, however the association constants of these other alkali salts are listed below in Table 2.3. Large values of K_{M+} indicate strong Na^+-crown interactions, and small values indicate a weak Na^+-crown interaction. The strength of the Na^+-crown interaction indicates the strength of the Na^+-A^- interaction in solution, where a strong Na^+-crown interaction necessitates a weak Na^+-A^- interaction. These data can give a hint to which anions would more likely be found nearby to the

encapsulated Na^+ ions. It is worth noting that association constants greater than ≈ 10^5 are commonly accepted to be above the limit of quantification for the NMR method.[65]

Table 2.3 Association constants of various alkali metal salts with **3Fe(CO)$_2$**.

Salt Titrant	Binding Constant / L mol^{-1}
$LiPF_6$	$K_{Li+} > 10^5$
$NaPF_6$	$K_{Na+} = 8.5 \times 10^4$
$NaBPh_4$	$K_{Na+} > 10^5$
$NaBH_4$	$K_{Na+} = 1.6 \times 10^4$
$NaNO_2$	$K_{Na+} = 2.26 \times 10^3$
$KBPh_4$	$K^{1:1}_{K+} = 1.95 \times 10^3$, $K^{2:1}_{K+} = 1.04 \times 10^3$

2.5 Conclusions

With the benzo-15-crown ether successfully installed into the secondary coordination sphere of Fe(PDI) complexes, and an understanding of the effects that binding alkali metal ions into the crown has on the Fe(PDI) compound, the next step is to perform reactivity studies with these compounds to investigate the effect (if any) that secondary sphere alkali metal ions have on the reactivity of Fe(PDI) complexes.

Chapter 3 – Enhancement of NO_x Reduction

3.0 Nitrite Reduction

As mentioned in Chapter 1, the reduction of nitrite is an important nitrogen fixation reaction undertaken by iron and copper containing nitrite reductases in Nature. The reduction of nitrite to form NO species is of biological importance due to the role of nitric oxide as a signaling molecule, where NO is known to be a vasodilator in cardiovascular systems acting to regulate blood flow.[66] Biochemical iron-NO species are found in the body in the form of dinitrosyl iron complexes (DNICs), that serve to transport and store NO *in vivo*.[67] Due to the unknown mechanism of nitrite reduction, recent studies have gained attention by trying to mimic the nitrite reductase active site in synthetic systems to gain mechanistic understanding.[25,68]

Previous work with iron (II) pyridinediimine systems has shown that nitrite reduction by these $Fe(^{L}PDI)(CO)_2$ complexes leads to the formation of dinitrosyl iron complexes (DNICs).[29,69] The Gilbertson group has previously installed a proton-shuttle via introduction of a pendant amine into the secondary coordination sphere of these complexes, showing increased kinetic activity towards nitrite reduction attributed to the increased effective concentration of the proton source close to the reactive center.[70] Further insight into the mechanism of nitrite reduction in these systems was investigated by utilizing the crown ether arm to increase the effective concentration of the reactive oxyanion near the reactive center.

3.1 Nitrite Reduction to Form Fe(^{b15c5}PDI)$(NO)_2^+$ (3Fe$(NO)_2$[X])

With the characterization of various encapsulated benzo-15-crown-5 products completed, the hypothesis of kinetic enhancement was ready to be tested. As nitrite reduction was previously shown to be promoted by the Fe(PDI)$(CO)_2$ complexes, it was chosen as a reaction probe for rate enhancement by encapsulated Lewis acids. Before probing this effect however, it was important to verify the expected Fe(PDI)$(NO)_2^+$ was the same product.

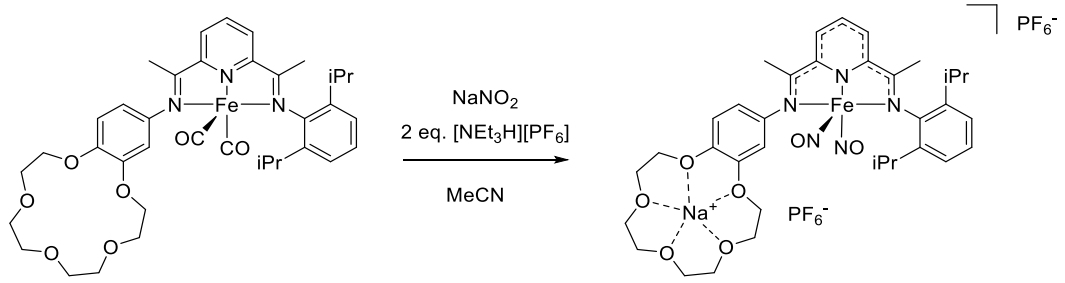

(**6**)

The nitrite reduction experiment was performed by charging a vial with **3Fe$(CO)_2$**, $NaNO_2$ and $[NEt_3H][PF_6]$ in a 2:1 mixture of THF/MeOH as per previous studies,[29] shown in eq. 6. Over a period of 12 hours, the solution changes color from a dark forest green to a brown-red indicating a reaction has taken place. After removal of the solvent under vacuum, the reaction mixture was re-dissolved in DCM and filtered through celite, and a dark orange solution was obtained. A solid state IR spectra of the solid was obtained, showing bands consistent with NO stretching frequencies[71] at 1785 and 1712 cm^{-1} and the presence of a PF_6^- anion at 828 cm^{-1}, Figure 3.1. X-ray quality crystals of **3Fe$(NO)_2$Na][PF_6]$_2$** were obtained by layering toluene on a concentrated THF solution, which was carefully placed in a freezer (-35°C) to slow down diffusion of the layers.

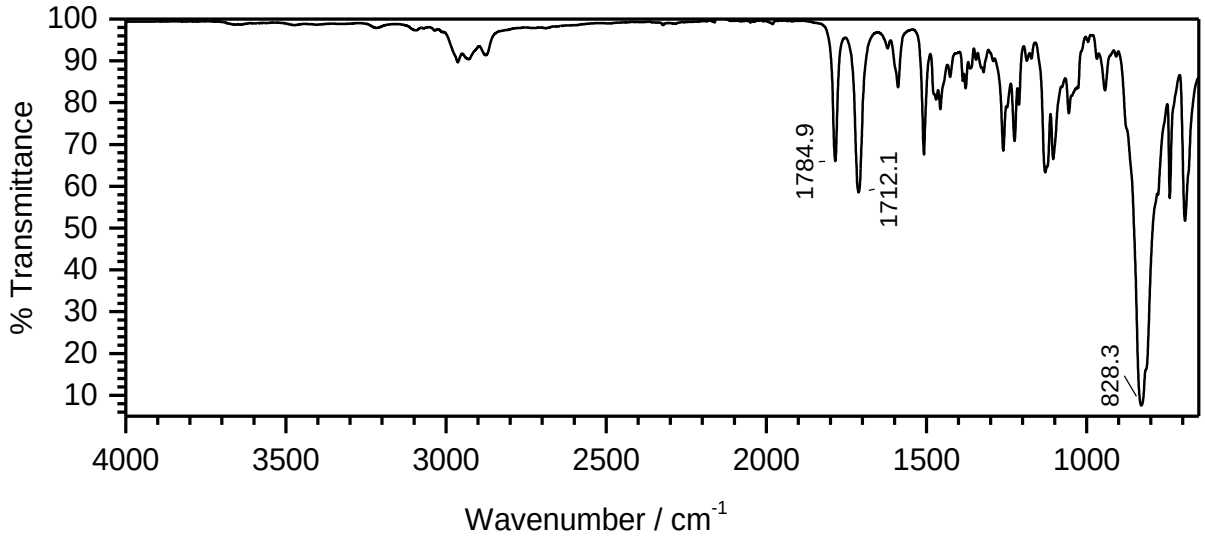

Figure 3.1 Solid FT-IR (ATR) spectrum of **[3Fe(NO)$_2$Na][PF$_6$]$_2$**.

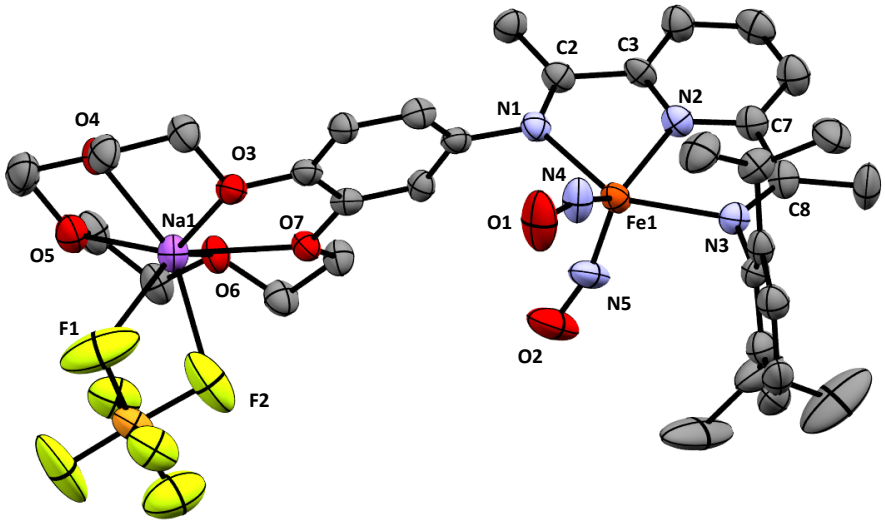

Figure 3.2 Solid state structure at 30% probability of **[3Fe(NO)$_2$Na][PF$_6$]**. The H atoms and one PF_6^- have been omitted for clarity. Selected bond lengths (Å): Fe(1)−N(1), 2.113(8); Fe(1)−N(2), 2.071(7); Fe(1)−N(3), 2.202(8); Fe(1)−N(4), 1.692(9); Fe(1)−N(5), 1.684(9); N(1)−C(2), 1.29(1); N(3)−C(8), 1.29(1); C(2)-C(3), 1.47(1); and C(7)-C(8), 1.49(1). Selected bond angles (°): N(4)Fe(1)N(5), 109.3(4); N(2)Fe(1)N(4), 135.6(4); N(1)Fe(1)N(3), 147.6(3); Fe(1)N(4)O(1), 157.9(9); and Fe(1)N(5)O(2), 161.3(8).

An ORTEP view of **[3Fe(NO)$_2$Na][PF$_6$]$_2$** can be seen in Figure 3.2, clearly showing an encapsulated $NaPF_6$ in the crown with an additional PF_6^- counter ion. The geometry around the Fe^{2+} center is a distorted square pyramid (τ_5 = 0.2). The bond angles between Fe-N-O for both nitrosyls are 157.9° and 161.3°. Typically, the bond angles of nitrosyl units can be used to determine the oxidation state of the NO unit. Since NO can exist in three different oxidation states as seen in Figure 3.3, NO can exhibit different binding modes, giving a wide range of M-N-O bond angles (Figure 3.3).[72]

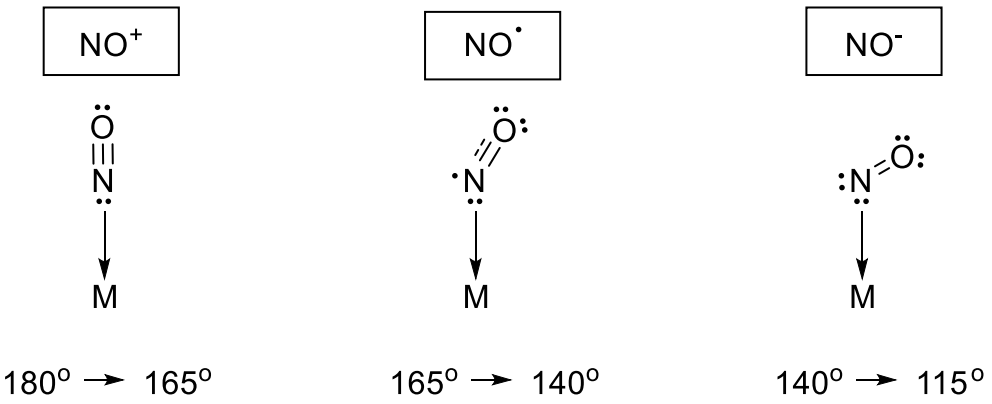

Figure 3.3 Oxidation state dependent M-NO binding modes.

When the M-N-O bond angle is linear, between 180° → 165°, this indicates NO^+. Slightly bent M-N-O bonds between 165° → 140° indicate $NO^\bullet$. Fully bent M-N-O bonds between 140° → 115° indicate NO^-. As the bond angles found in **3Fe(NO)$_2^+$** lie close to the ranges that define $NO^\bullet$ and NO^-, a definitive assignment of the NO oxidation states cannot be made in this case.

Determination of the oxidation states of dinitrosyl iron complexes can be difficult if they do not fall into these ranges due to the similar energies of the frontier orbitals in both the Fe and NO, leading to difficulty in assigning the orbitals that contain the electrons.[73] For this reason, the

Enemark-Feltham notation is used, which assigns the d-electrons to the $\{Fe(NO)_2\}$ unit avoiding ambiguity altogether.[74]

The oxidation state assignment of **$[3Fe(NO)_2Na][PF_6]_2$** using the Enemark-Feltham notation is $\{Fe(NO)_2\}^9$. In this method, the metal center is treated as neutral, with all its d-electrons, in this case Fe^0 which is a d^8 metal. Each NO is treated as a 1 e^- donor, and after accounting for the positive charge of the overall complex, as evidenced by the second PF_6^-, the total number of electrons is found to be 9.

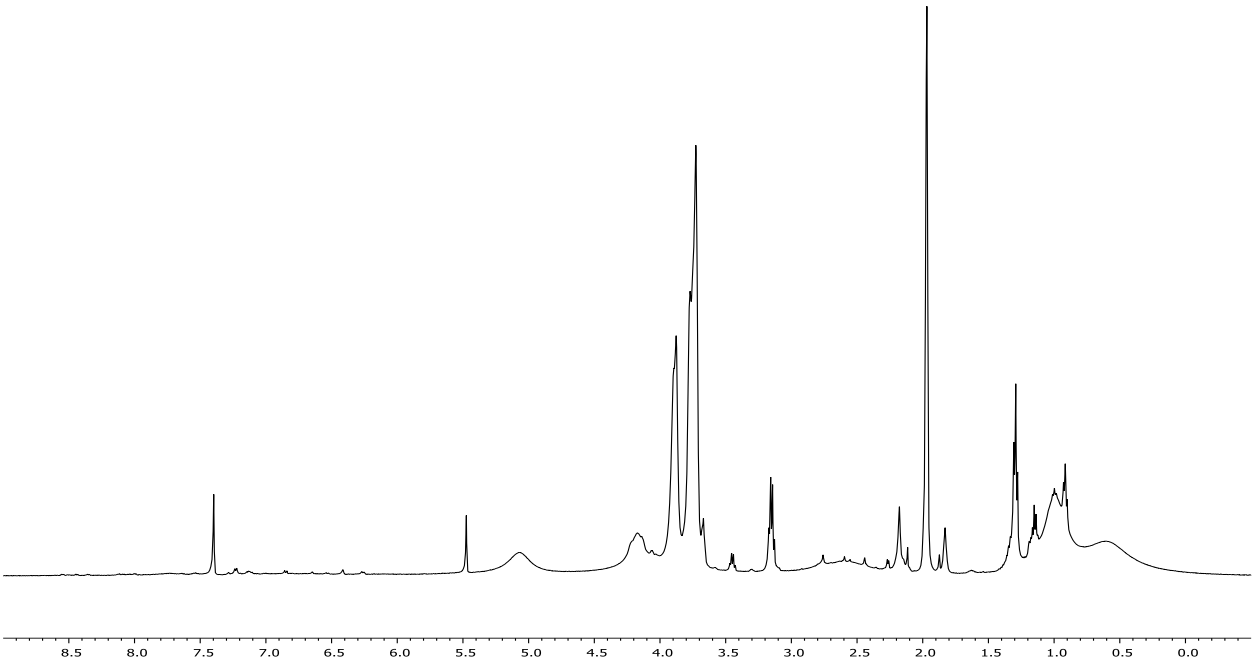

Figure 3.4 ^1H NMR Spectrum of **$[3Fe(NO)_2][PF_6]_2$** in CD_3CN (500 MHz)

The ^1H NMR spectra of **$[3Fe(NO)_2Na][PF_6]_2$** can be seen in Figure 3.4. The loss of the assigned peaks of the dicarbonyl compound, as well as peak broadening indicate the compound is likely weakly paramagnetic. The solution phase magnetic susceptibility measurements (μ_{eff} = 2.07 μ_B), confirm the compound is weakly paramagnetic with a spin system of S = 1/2, consistent

with previously reported PDI DNICs of one unpaired electron delocalized over the $\{Fe(NO)_2\}^9$ unit.[72]

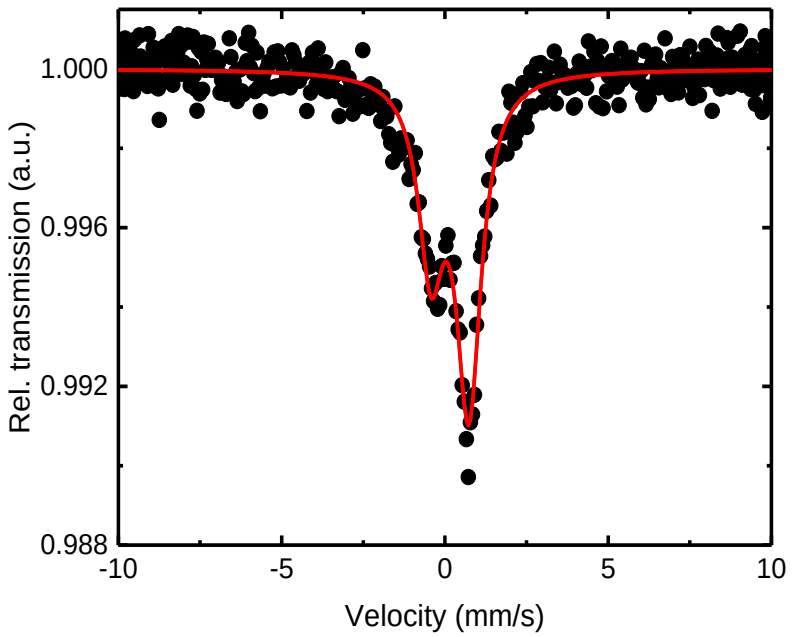

Figure 3.5 Room Temperature Zero-field Mössbauer spectrum of **$[3Fe(NO)_2Na][PF_6]_2$**. Isomershift, δ = 0.25(1) mm/s, Quadrupole splitting, ΔE_Q = 1.16(2) mm/s, Line width, Γ = 0.92(3) mm/s.

Additionally, the room temperature Mossbauer spectrum of **$[3Fe(NO)_2Na][PF_6]_2$** can be seen in Figure 3.5, where the Mossbauer parameters (δ = 0.25(1) mm/s, and ΔE_Q = 1.16(2) mm/s) are consistent with previously reported $\{Fe(NO)_2\}^9$.[29,67,69,72]

3.2 Reaction Stoichiometry and Yield Determination

During encapsulation of $NaNO_2$ into **$3Fe(CO)_2$** to form **$[3Fe(CO)_2Na][NO_2]$**, the compound was left in the THF/MeOH solution for long periods of time (7+ days) resulting in the formation of **$3Fe(NO)_2^+$**. This indicates that the MeOH can act as the proton source for the nitrite reduction, as seen in eq. 7. To control the concentration of the proton source, the solvent was changed from MeOH to MeCN, where the only possibility for a proton source was through the added acid.

$$\mathbf{3Fe(CO)_2} + NaNO_2 + 2\ MeOH \longrightarrow \frac{1}{2}\ \mathbf{3Fe(NO)_2^+} + H_2O + Na^+ + 2\ OMe^- + 2\ CO \qquad (\mathbf{7})$$

In various syntheses of **$3Fe(NO)_2^+$** in MeCN, when the reaction was not worked up within 24 hours, the brown-orange solution would decompose and change to a deep greenish-blue solution. To elucidate the cause, a determination of the reaction stoichiometry through solution based liquid cell IR measurements was performed. The relative concentrations of $NaNO_2$ and $[NEt_3H][PF_6]$ were varied and these reaction mixtures were analyzed using a liquid IR cell and the yields were obtained through use of a calibration curve of the final product.

$$\mathbf{3Fe(CO)_2} + NO_2^- + 2\ H^+ \longrightarrow \frac{1}{2}\ \mathbf{3Fe(NO)_2^+} + H_2O + CO + \frac{1}{2}\ \mathbf{3Fe(CO)_2} \qquad (\mathbf{8})$$

According to eq. 8, in a 1**:**1**:**2 mixture of **$3Fe(CO)_2$** / NO_2^- / H^+, there is only be enough NO_2^- for a 50% yield in the final DNIC product. As seen in Figure 3.6, the formation of the DNIC was not observed after the 18 or 72-hour time intervals as evidenced by the lack of ν_{NO} peaks at 1793 and 1722 cm^{-1}. In a 1:2:2 mixture, the reaction goes to completion, however the yield drops to

60% if left to sit for 3+ days, determined by the calibration curve in Figure 3.7. In a 1:2:4 reaction mixture, the yield in the DNIC was 100% and with no product decomposition after 72 hours.

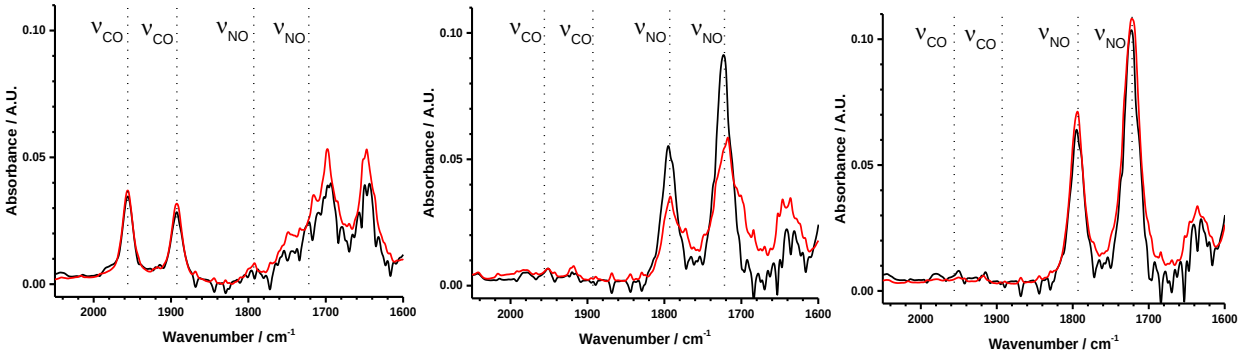

Figure 3.6 Liquid FT-IR Cell Yield Measurements. Ratios of **$3Fe(CO)_2$** to $NaNO_2$ to $[NEt_3H][PF_6]$ were a) 1:1:2, b) 1:2:2 and c) 1:2:4. Color coding represents 18 hrs (black) and 72 hrs (red).

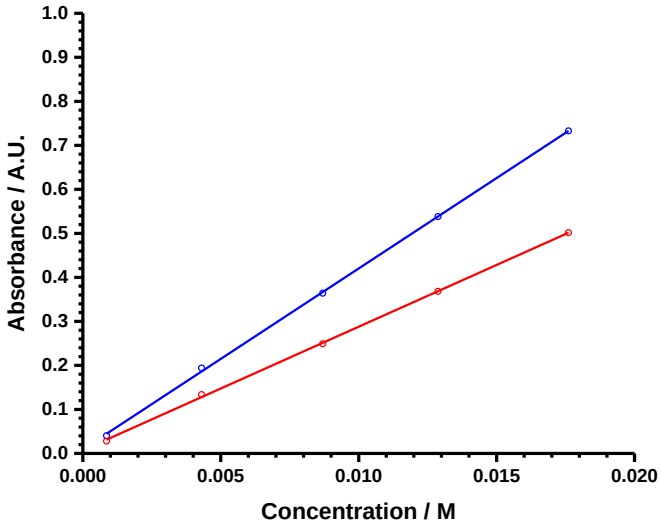

Figure 3.7 Liquid FT-IR cell calibration curve of ν_{NO} peaks at 1793 cm^{-1} (y = 28.073x + 0.007, R^2 = 0.998, red) and 1722 cm^{-1} (y = 41.090x + 0.009, R^2 = 0.998, blue).

These results indicate that both the electrons stored in the backbone of the PDI can participate in nitrite reduction, and with 2 eq. of nitrite and 4 eq. of acid (enough to get all the way to water) the formation of the DNIC product goes to completion. The rapid formation of

DNIC is still observed if there are not enough protons, however the likely initial formation of hydroxide slowly decomposes the DNIC, leading to loss of the DNIC product. The reaction stoichiometry of nitrite reduction was adjusted according to eq. 9 for future experiments.

$$\mathbf{3Fe(CO)_2} + 2\ NO_2^- + 4\ H^+ \longrightarrow \mathbf{3Fe(NO)_2^+} + 2\ H_2O + 2\ CO \qquad (\mathbf{9})$$

3.3 Kinetics Enhancement of Nitrite Reduction Through Lewis Acids

With the nitrite reduction product confirmed to be a dinitrosyl iron complex, and the stoichiometry determined to be a 1:2:4 molar ratio of **3Fe(CO)$_2$** / NO_2^- / H^+, the next step was to explore the potential kinetic enhancement effect of shuttling in the reactive anion. As seen in Figure 3.8, the comparison of the pre and post reaction UV-Vis spectra indicate a loss of the charge transfer bands (λ_{max} = 429, 361 nm) and d←d (λ_{max} = 758 nm) of Fe(^{b15c5}PDI)(CO)$_2$ and the growth of a new charge transfer band (λ_{max} = 290 nm) of Fe(^{b15c5}PDI)$(NO)_2^+$.

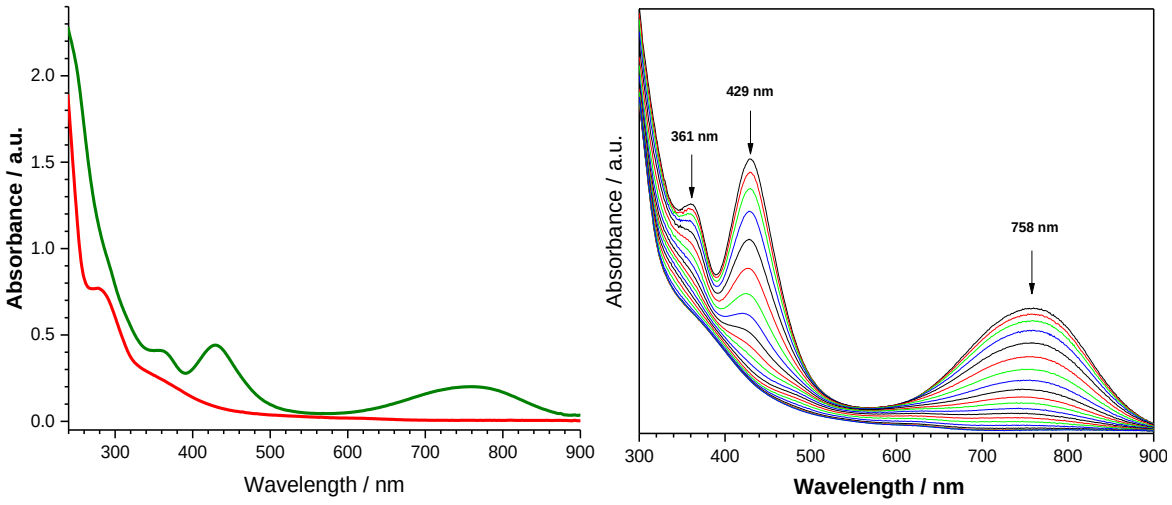

Figure 3.8 UV-Vis spectra of **3Fe(CO)$_2$** (left, red) and $[3Fe(NO)_2Na][BPh_4]_2$ (left, green). Full window kinetic traces of nitrite reduction by **3Fe(CO)$_2$**, forming **3Fe(NO)$_2^+$** (right).

These data were used to determine that the kinetics would be measured through the decay of the d←d band (λ_{max} = 758 nm) through the method of initial rates in order to avoid complications introduced with the unknown mechanism as described in Section 3.1, which potentially includes gas-liquid interface kinetics as it is not understood whether the reduction of the nitrite anion in these systems is inner sphere or outer sphere in nature, which could lead to NO gas in the headspace of the reaction vessel before binding.

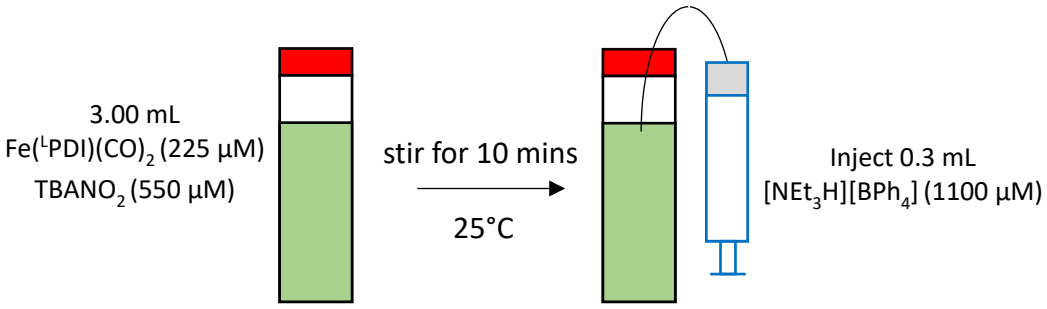

Figure 3.9 General method for nitrite reduction kinetics monitored by UV-Vis. Reaction solution (green), pierceable septa (red), and syringe with needle.

To perform the kinetic experiments, stock solutions of the FePDI compounds, tetra(n-butyl)ammonium nitrite ($TBANO_2$), and triethylammonium tetraphenylborate ($[NEt_3H][BPh_4]$) were prepared in acetonitrile. The nitrite salt was chosen to be fully soluble in organic solvents to remove solubility effects from affecting the reaction. The FePDI and NO_2^- were prepared together in a 10 mL volumetric to obtain solutions with concentrations seen in Figure 3.9. 3.0 mL of this solution was then added to a quartz cuvette equipped with a stir bar and pierceable septa, then placed in the spectrometer at 25°C for 10 mins while monitoring the λ_{max} of the d←d transition, ca. 758 nm. This step was to ensure enough time to equilibrate the temperature of the solution, as well as to make sure were no leaks in the septa that would lead to degradation

of the signal, by reaction with O_2 in the air. As the kinetics were to be monitored by the decay of the FePDI signal, it was important to ensure that measured loss of signal was solely due to reduction of nitrite. After this induction period, 4 eq. (0.3 mL) of the acid was injected into the solution and the kinetics experiment was started. In the cases of added alkali salts or exogenous benzo-15-crown-5 ether, the corresponding reagents were added to the initial 10 mL volumetric at the same concentration as the FePDI.

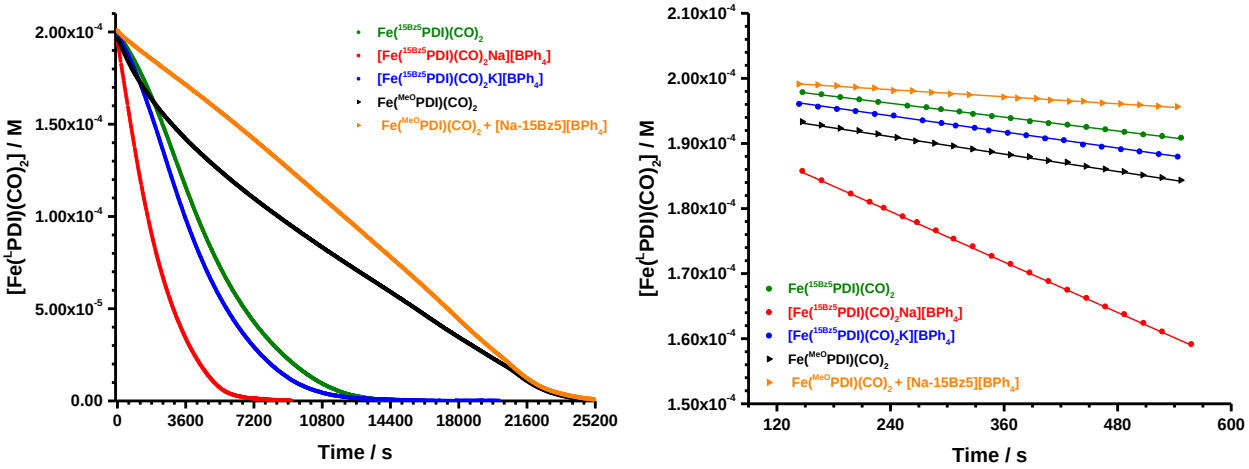

Figure 3.10 Kinetic traces of nitrite reduction. Global kinetics of Fe(^{L}PDI)(CO)$_2$ + 2 eq. TBANO$_2$ + 4 eq. [NEt$_3$H][BPh$_4$] (left). Initial rate data from kinetics runs (right).

Each of these kinetic experiments seen above (Fig. 3.10, left) were run in triplicate, with one representative kinetic trace of each. The initial rates were extracted from the first five minutes of the reactions (Fig. 3.10, right) and these initial rates can be seen below in Table 3.1.

Table 3.1 Initial rate data of Lewis acid assisted nitrite reduction.

Compound	Rate / Ms^{-1}	Std. Dev. / Ms^{-1}	Rel. Rate vs $3Fe(CO)_2$
$3Fe(CO)_2$	1.79×10^{-8}	0.63×10^{-9}	1.00
$[3Fe(CO)_2Na][BPh_4]$	6.16×10^{-8}	2.5×10^{-9}	3.43
$[3Fe(CO)_2K][BPh_4]$	2.03×10^{-8}	1.2×10^{-9}	1.13
$2Fe(CO)_2$	2.11×10^{-8}	2.1×10^{-9}	1.18
$2Fe(CO)_2$ + b15c5 + $NaBPh_4$	0.866×10^{-8}	0.52×10^{-9}	0.48

To probe the effect of encapsulating alkali ions into the secondary coordination sphere, the empty crown complex **$3Fe(CO)_2$** was compared to a Na^+ encapsulated crown, **$[3Fe(CO)_2Na][BPh_4]$**. The Na+ encapsulated compound showed kinetic enhancement relative to the empty, with the initial rate increasing from 1.79×10^{-8} to 6.16×10^{-8} Ms^{-1}, by a factor of 3.5. This is likely due to an electrostatic interaction between the Na^+ and the NO_2^- in solution, where the NO_2^- would preferentially exist near the Na^+, compared to the BPh_4^-. This is evidenced by the difference in Na^+-crown association constants between the BPh_4^- and NO_2^- salts ($K_{Na+} > 10^5$ and $K_{Na+} \approx 10^3$ respectively), where a weaker binding constant between the Na^+-crown in the NO_2^- case indicates a stronger Na^+-NO_2^- interaction.

To investigate if the NO_2^- was simply being activated by interaction with the encapsulated Na^+, control experiments using **$2Fe(CO)_2$** with and without exogenous Na^+ encapsulated benzo-15-crown-5 ether. The initial rate of **$2Fe(CO)_2$** is virtually identical to **$3Fe(CO)_2$**, being 1.79×10^{-8} and 2.11×10^{-8} Ms^{-1} respectively, however the initial rate of nitrite reduction by **$2Fe(CO)_2$** in the presence of $NaBPh_4$ encapsulated in benzo-15-crown-5 ether exhibits slowed reaction kinetics, with the initial rate decreasing from 2.11×10^{-8} to 0.866×10^{-8} Ms^{-1}, slowing by a factor of 2. This

effect can be attributed to the slowed rate of NO_2^- reaching the active site due to the increased steric bulk of association with the free Na^+-crown.

In an additional control experiment, a K^+ salt was encapsulated into the crown ether to determine if the increased initial rate of nitrite reduction was caused by intramolecular interactions. As previously discussed in chapter 2, **[3Fe(CO)$_2$Na][BPh$_4$]** forms a centrosymmetric dimer in the solid state. While further characterization showed that the dimer likely does not exist in solution, it was necessary to determine if this kind of dimer, if formed in small quantities not easily observed spectroscopically, could be responsible for the increase in the initial rate.

Potassium salts are known to form 1:2 K^+-crown interactions in solution, and evidence for these dimers formed with the **3Fe(CO)$_2$** can be seen in the ^{1}H NMR salt titration experiments performed with $KBPh_4$ (see experimental figure E39), where the initial upfield shifts upon addition of K^+ is caused by the shielding effect of two molecules of **3Fe(CO)$_2$** closely associated in solution. This effect is greatest at 0.5 eq of K^+, indicating a 1:2 binding affinity, where additional K^+ results in disruption of the association equilibrium of the formed dimer. By ensuring that this dimer was formed in solution during the kinetic experiment, an initial rate enhancement in the nitrite reduction should also be observed if an intramolecular interaction was responsible. This is not observed however, as the initial rate of **[3Fe(CO)$_2$K][BPh$_4$]** shows a nearly identical initial rate to that of **3Fe(CO)$_2$**, being 1.79×10^{-8} and 2.03×10^{-8} Ms^{-1} respectively. This serves to rule out the likelihood of an intramolecular interaction in solution causing the enhanced rates.

These data taken together clearly show that an encapsulated sodium tethered to the secondary coordination sphere facilitates enhanced reaction kinetics through intermolecular interactions with the nitrite, having an initial rate almost seven times faster than the control without the Na^+-crown interaction appended into the secondary coordination sphere.

3.4 Proposed Mechanism of Kinetic Enhancement

Based on the findings from the kinetics data from nitrite reduction above, and spectroscopic characterization of $Fe(PDI)(CO)_2$ complexes,[27,56,61] a mechanism for the kinetic enhancement of nitrite reduction can be proposed.

Scheme 3.1 Proposed mechanism of encapsulated Lewis acid assisted nitrite reduction. 15-crown-5 ether depicted as ring on aryl arm.

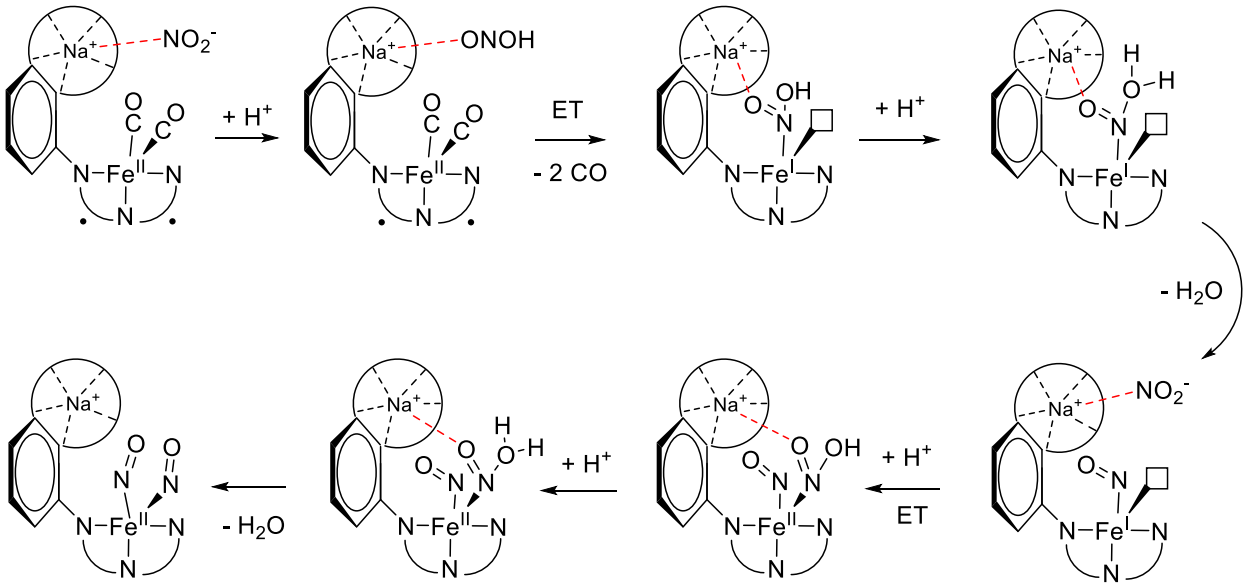

First, the nitrite anion is positioned close to the redox-active site by electrostatic interaction with the encapsulated Lewis acid. After a proton transfer step to form nitrous acid (HONO), a ligand-based electron transfer occurs, reducing the nitrous acid by one electron. This initial

proton transfer step is likely to occur first as the reduction potential of nitrous acid is more positive than nitrite, meaning the electron transfer to HONO would be easier than NO_2^-. The electronics of the ligand backbone are no longer stable, releasing the CO ligands, with the remaining electron now residing in the Fe center, forming Fe(I), as shown in literature.[27] This leaves open coordination sites for the reduced nitrogen species to bind. After an additional proton transfer step forming N-OH_2, water is cleaved forming the first bound nitrosyl. A second nitrite molecule is enticed into binding to the open coordination site on the metal where it is reduced by one electron, leaving an Fe(II) species. After two proton transfer steps and subsequent loss of water, the final dinitrosyl iron complex is formed. This mechanism is consistent with Mechanism A discussed in Section 1.4. Most of this mechanism would likely be similar for the control compound **$2Fe(CO)_2$**, which does not feature a pendant Lewis acid interaction, lacking the pre-association in the first step which is likely the cause of the ~ 4-fold kinetic enhancement seen in the initial rate analysis.

Further investigations could probe the validity of this mechanism by repeating these kinetic experiments using pendant amines, which could act to shuttle protons to the nitrogen species, facilitating rate enhancement of the proton transfer steps. Compounds featuring pendant amines would likely show even greater rate enhancement relative the pendant crown ether compounds.

Chapter 4 – Redox Non-Innocent Tripodal Ligand Design.

4.0 Tripodal Ligand Scaffolds

As seen in some notable examples in Section 1.2, tripodal ligand scaffolds are common in coordination chemistry.[14,21,24,68] Often, when coordinated to five-coordinate metal centers, they enforce C_3 symmetry, leaving a single open coordination site. These ligand frameworks have been shown to stabilize reactive intermediates with the careful design of H-bond donor and acceptors in the secondary coordination sphere.[14]

One major drawback of these ligand designs is their redox innocence. Unlike with the pyridinediimine ligand scaffold, where several ligand-based redox states can be accessed, the redox behavior of many metal-ligand complexes featuring tripodal ligand scaffolds is restricted to the oxidation states available to the metal, which can limit the chemistry available to mononuclear sites. One solution is to design a ligand scaffold capable of binding two metal centers, leading to cooperative chemistry between multiple metal sites.[75–77] The solution we set out to investigate was to use the redox active nature of the PDI to design redox non-innocence into the tripodal ligand scaffold. If successful, we could expand the synthetic toolbox and could translate the secondary sphere interactions previously installed on the PDI ligands into the tripodal ligand frameworks. Two of the ligand designs can be seen in Figure 4.1, with ethyl and phenyl linkers between the imines and the central tertiary nitrogen. Initial studies were performed by first synthesizing the Zn-ligand complexes, as zinc is redox-inactive and any redox activity would be attributed to the ligand framework.

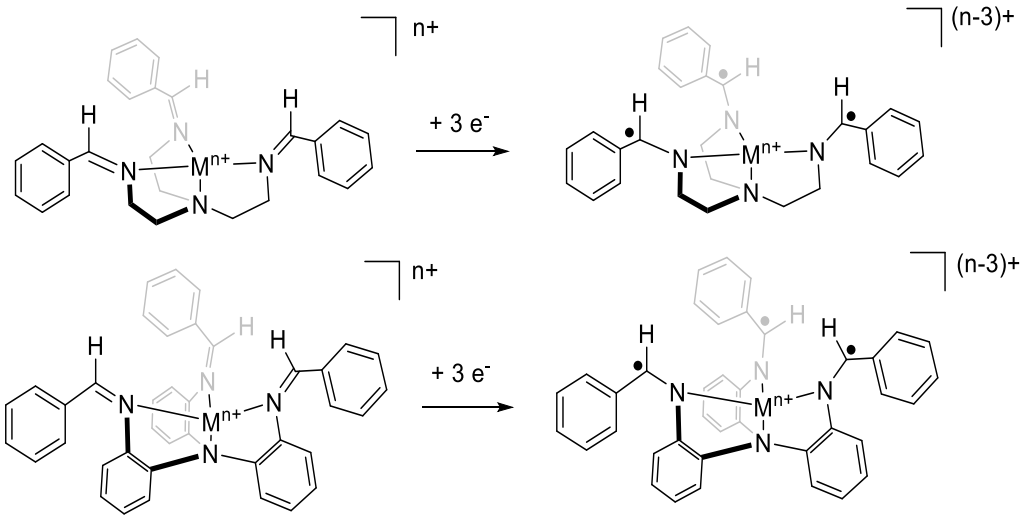

Figure 4.1 Proposed tripodal ligand designs featuring redox-noninnocence.

4.1 Synthesis and Characterization of N(EtN=CHPh)$_3$ (4) Complexes

Synthesis of N(EtN=CHPh)$_3$ (**4**) was performed according to a literature preparation.[78] Tris(2-aminoethyl)amine, and freshly distilled benzaldehyde were dissolved in acetonitrile and refluxed for 6 hours. The solvent was removed under vacuum leaving the desired product as a white solid, (**4**). Inside an N_2-filled glovebox, a vial was charged with compound **4**, 1 eq. of zinc trifluoromethanesulfonate, 20 mL of acetonitrile and a stirbar. This was stirred until all the solid had disappeared, likely indicating coordination of Zn^{2+} to **4** forming **4Zn(OTf)$_2$** (Scheme 4.1).

Scheme 4.1 Synthesis of **4Zn(OTf)$_2$**.

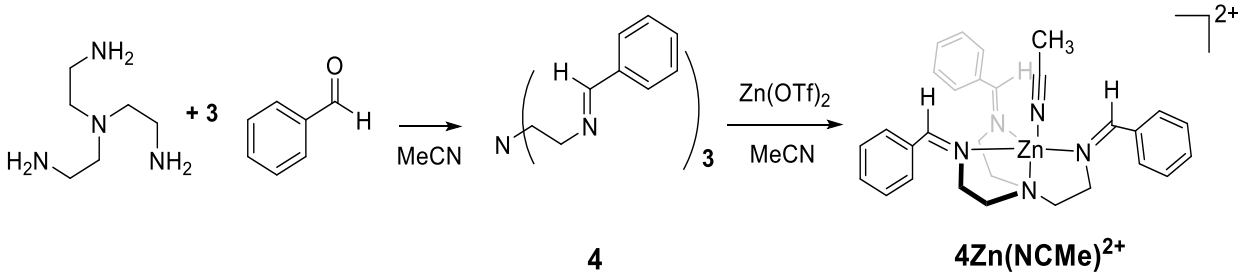

4 **4Zn(NCMe)$^{2+}$**

The solution was filtered and carefully layered with ether to crystallize, yielding large clear X-ray quality crystals, confirmed to be **4Zn(NCMe)(OTf)$_2$** where an acetonitrile ligand occupies the open coordination site, as seen in Figure 4.2. In the solid state, two of the benzaldehyde phenyl rings are pointed toward the inner-sphere, while one is pointed away. This is likely due to the disfavored steric interactions of all three phenyl rings adopting a similar arrangement about the Zn (II) center. As the formed imine bonds cannot rotate, this effect of one dissimilar imino arm is also present in the solution phase, as seen in the ^{1}H NMR of **4Zn(NCMe)[OTf]$_2$** seen in Figure 4.3, where the three N=CH protons integrate in a 1:2 ratio, due to the two different chemical environments the aldimine protons exist in.

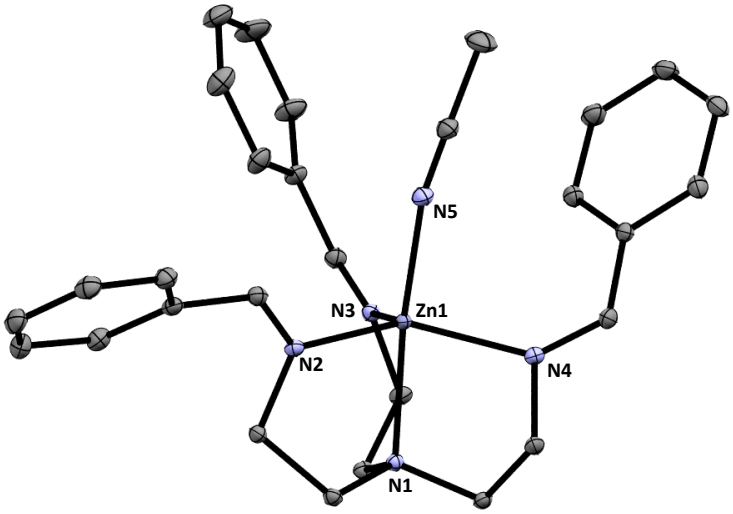

Figure 4.2 Solid state structure at 30% probability of **4Zn(NCMe)[OTf]$_2$**. The H atoms and both triflates have been omitted for clarity. Selected bond lengths (Å): Zn(1)-N(1), 2.2058; Zn(1)-N(2), 2.0667; Zn(1)-N(3), 2.0710; Zn(1)-N(4), 2.0996; and Zn(1)-N(5), 2.0810. Selected bond angles (˚): N(1)Zn(1)N(5), 168.80; and N(2)Zn(1)N(4), 131.97.

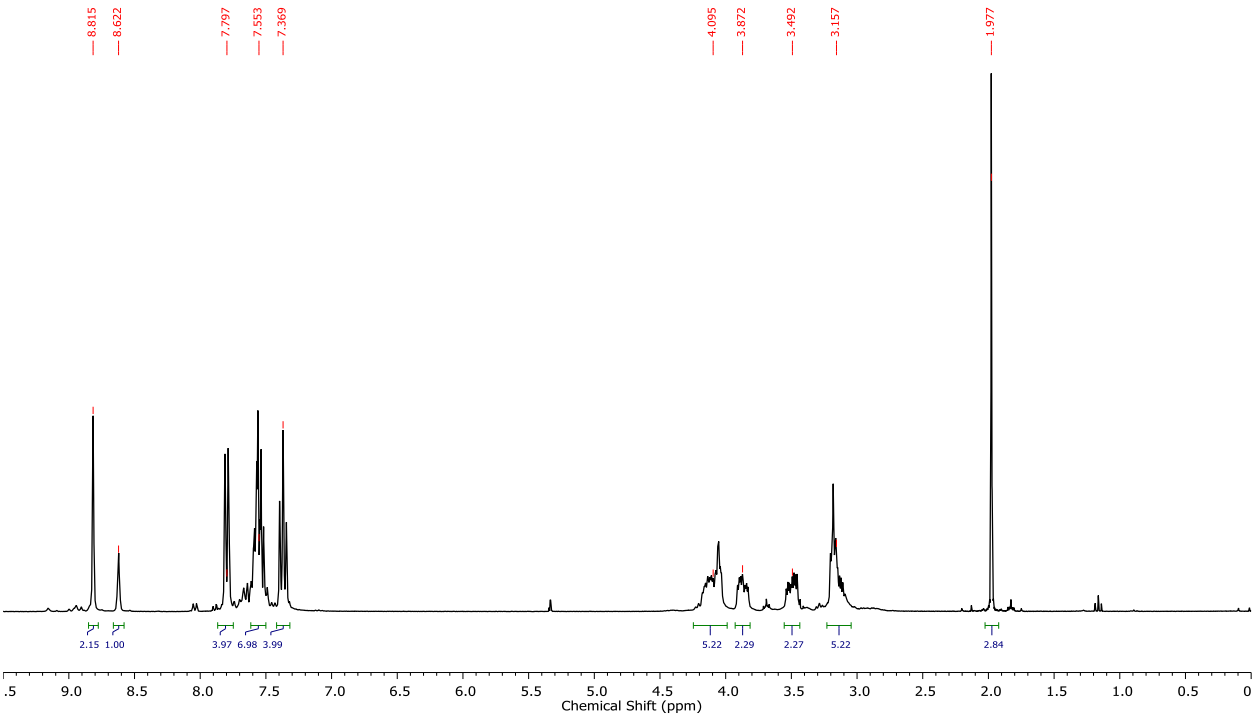

Figure 4.3 ^{1}H NMR of **4Zn(OTf)$_2$** in CD_2Cl_2 (500 MHz).

4.2 Synthesis and Characterization of N(*o*-PhN=CCH$_3$Ph)$_3$ (5) Complexes

Synthesis of N(*o*-PhN=CCH$_3$Ph)$_3$ (**5**) started with the formation of tris(2-nitrophenyl)amine through nucleophilic aromatic substitution (SN_{Ar}), adapted from literature preparation[79] as seen in Scheme 4.2. 2-nitroaniline, two mol equivalents of 1-fluoro-2-nitrobenzene, potassium carbonate as a base were added to a 100 mL round bottom flask along with 60 mL of DMSO and a stir bar. The reaction mixture was heated while stirring to 150˚C under an N_2 atmosphere and allowed to react for 84 hours. The solution was allowed to cool to room temperature before the contents of the flask were poured into 1 L of deionized water with strong stirring to precipitate the reaction products. The mixture was filtered, and the solid was re-dissolved in hot methanol. After a second filtration, the solid was washed with cold acetone, the resulting yellow solid is the desired tris(2-nitrophenyl)amine. The deep red acetone soluble product is the singly substituted product, bis(2-nitrophenyl)amine, and was dried in vacuo and set aside.

Scheme 4.2 Synthesis of **5Zn(OTf)$_2$**.

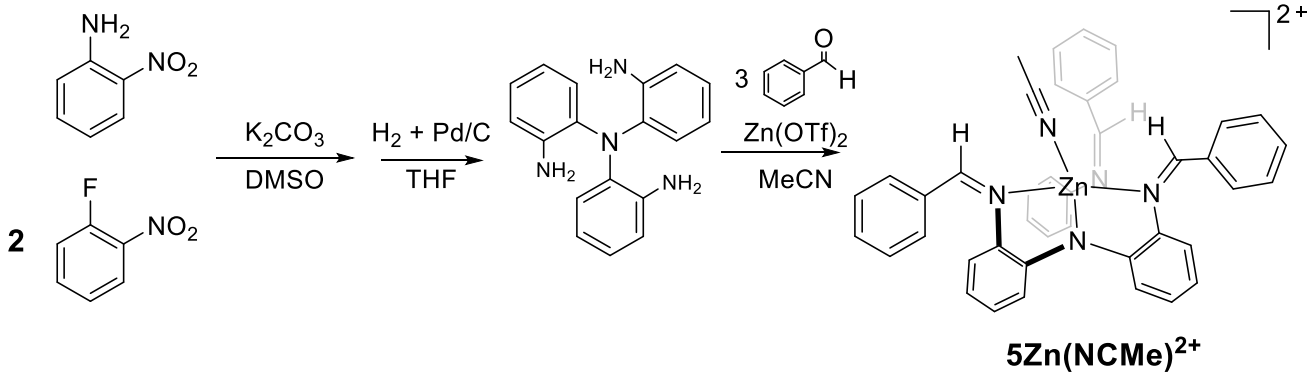

The ^{1}H NMR of tris(2-nitrophenyl)amine can be seen in Figure 4.4, showing a purified product ready for the next step of the synthesis, hydrogenation of the nitro groups to the corresponding amines.

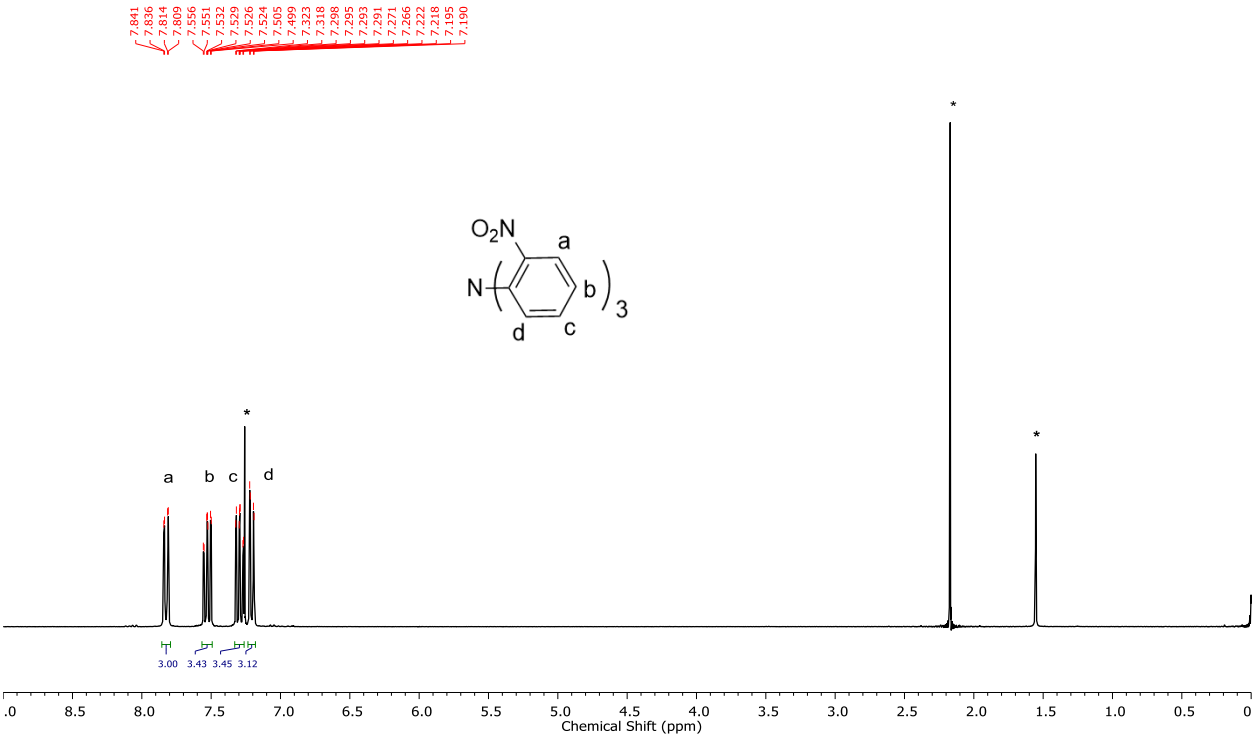

Figure 4.4 ^{1}H NMR spectra of tris(2-nitrophenyl)amine $CDCl_3$ (500 MHz).

The hydrogenation to the corresponding amines was facilitated using Pd on carbon. 2 g of tris(2-nitrophenyl)amine, 0.5 g of 10% Pd/C, a stirbar and 25 mL of tetrahydrofuran were added to a Fisher-Porter bottle inside of an N_2-glovebox and sealed with a pressure gauge. Outside of the box, the vessel was charged with 40 psi of H_2 and the slurry was stirred vigorously. A decrease in the pressure reading over time indicates consumption of H_2 and the vessel was periodically recharged with more H_2 until the pressure was maintained, marking that the reduction was complete. After filtering off the Pd/C, the solution was pulled dry under vacuum to yield a yellow solid confirmed to be the desired precursor of tris(2-aminophenyl)amine by FT-IR analysis as seen in Figure 4.5, where the new stretches at 3454 and 3358 cm^{-1} indicate presence of a secondary amine, NH_2.

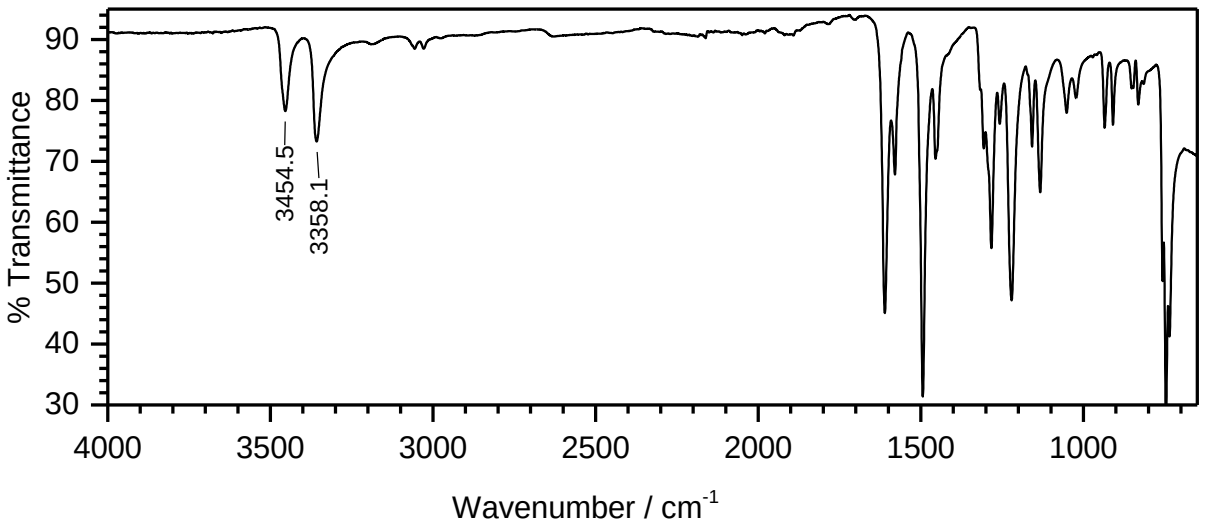

Figure 4.5 Solid FT-IR (ATR) Spectrum of tris(2-aminophenyl)amine.

Isolation of the free ligand, compound **5**, featuring the imine arms formed through Schiff-base with benzaldehyde proved difficult, so compound **5** was instead formed at the same time as the metalation via metal templated Schiff-base condensation method employed in Chapter 2.

Tris(aminophenyl)amine, benzaldehyde and zinc triflate were added to a Schlenk neck flask with 40 mL of EtOH. The reaction mixture was heated under N_2 at 78˚C for 12 hours, followed by filtration through celite. After removal of the solvent under vacuum, X-ray quality crystals were obtained by carefully layering diethyl ether on a saturated MeCN solution, yielding large clear crystals identified as **5Zn(NCMe)[OTf]$_2$**. An ORTEP view of the solid-state crystal structure of **5Zn(NCMe)[OTf]$_2$** can be seen in Figure 4.6.

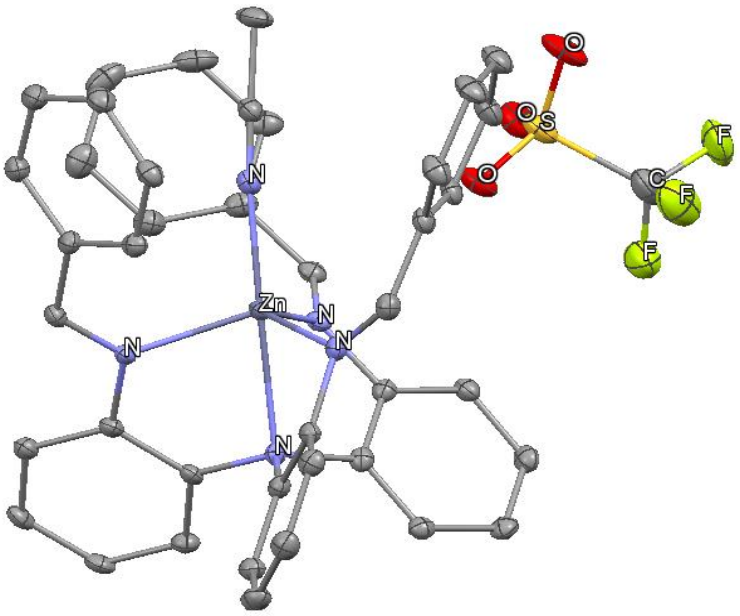

Figure 4.6 Solid state structure at 30% probability of **5Zn(NCMe)[OTf]$_2$**. The H atoms and second triflate have been omitted for clarity.

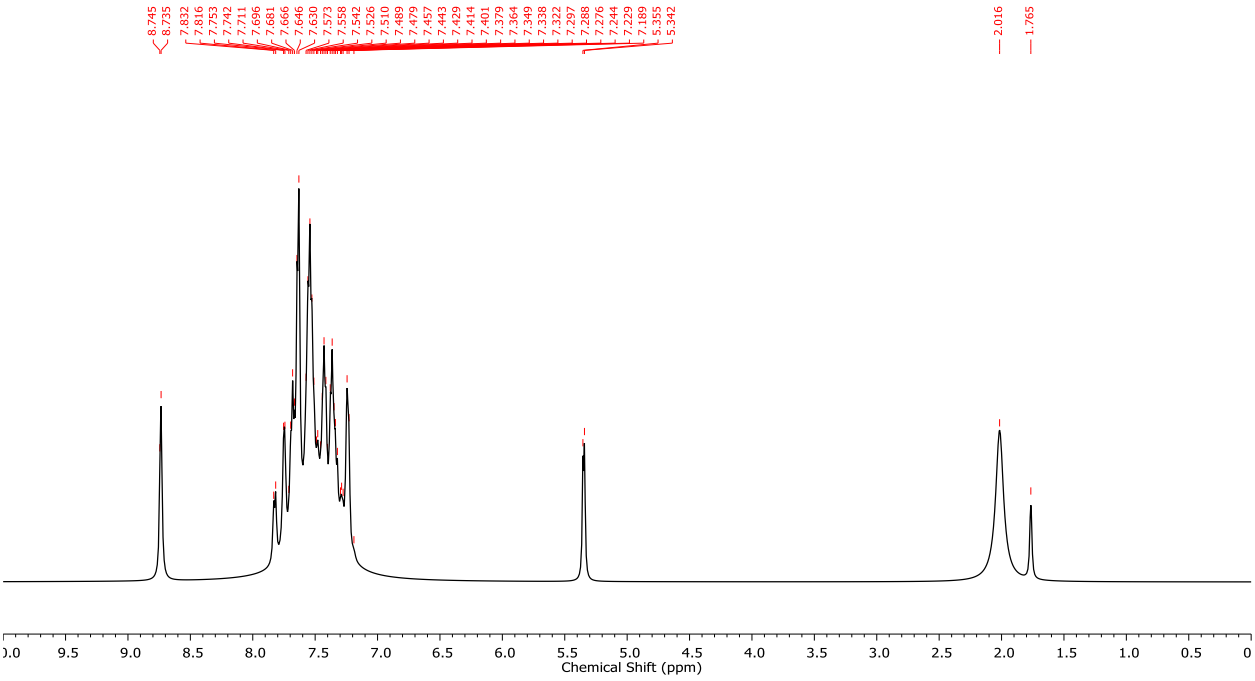

Figure 4.7 ^{1}H NMR of **5Zn(OTf)$_2$** in CD_2Cl_2 (500 MHz). α-aldimine proton, 8.74 ppm, bound CH_3CN, 2.02 ppm.

4.3 Electrochemical Studies of Tripodal Ligands

To explore the potential redox-activity of the tripodal ligands, electrochemical studies were first performed on the metallated complexes featuring zinc. The preliminary findings can be seen in Figure 4.8, where both complexes show redox-activity. As zinc is a redox-inactive metal, these non-faradaic currents must be attributed to the tripodal ligand.

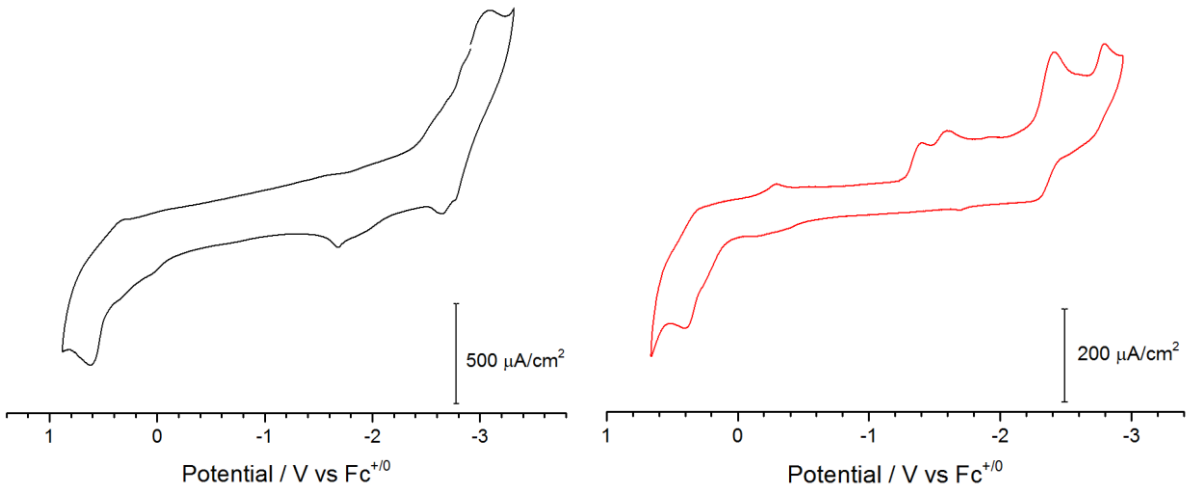

Figure 4.8 Cyclic Voltammograms of 1 mM **4Zn(NCMe)[OTf]$_2$** (left) and 1 mM **5Zn(NCMe)[OTf]$_2$** (right) in MeCN. WE: GC, RE: Ag/Ag$^+$, CE: Pt wire.

4.4 Future Work

Preliminary findings show that the concept of building redox activity into tripodal ligand scaffolds has promise, however these complexes are extremely air and/or water sensitive, as they quickly decompose when brought outside of a glovebox. This is likely due to the relative instability of a Lewis acid (Zn^{2+}) activated aldimine. Further studies will likely need to include ligand designs featuring ketimines, formed from the corresponding ketones such as acetophenone. It might also be necessary to metallate with redox active metals like Fe^{2+} to fully explore the redox-activity.

Chapter 5 – Furthering CO_2 Reduction by Fe(PDI) Complexes

5.0 Ligand Based CO_2 Reduction

As mentioned in Ch.1, previous work has shown iron (II) PDI complexes facilitate ligand-based reduction of CO_2 to CO.[30] Scheme 5.1 depicts this reaction cycle, where the starting compound **$2FeCl_2$** is reduced by 2 equivalents of a strong reductant ($NaHBEt_3$), reducing the ligand backbone by two electrons and allowing N_2 to bind terminally to iron. Three equivalents of this Fe(PDI)N_2 then participates in the 2 e^- reduction of CO_2 as seen in eq. 10. Two Fe(PDI)N_2 molecules act as the reductant for the third Fe(PDI)N_2 molecule, and given an O-atom acceptor such as trimethylsilylchloride instead of protons, the third Fe(PDI)N_2 forms Fe(PDI)$(CO)_2$.

$$CO_2 + 2\,e^- + 2H^+ \longrightarrow CO + H_2O \qquad (\mathbf{10})$$

There are three notable issues with this system however; 1) this synthesis is a limited number of cycles (being only one in the current system) as Fe(PDI)$(CO)_2$ cannot participate in further reactions, 2) the reaction must be run under low temperature (-35°C) for the necessary use of a sufficiently strong reductant to reduce the Fe(PDI), as when run at room temperature the reductant degrades the starting material, and 3) the reductant is a non-regenerable hydride source, meaning it is spent once used. For these reasons, further investigations into these complexes must address some or all these issues. Ideally, use of a catalytic, regenerable reductant that could operate at elevated temperatures without degrading the compounds in a system where CO is easily released (or further reduced) to regenerate the starting material for use in further reduction chemistry.

Scheme 5.1 Ligand-based reduction of CO_2 release of CO on iron (II) PDI.

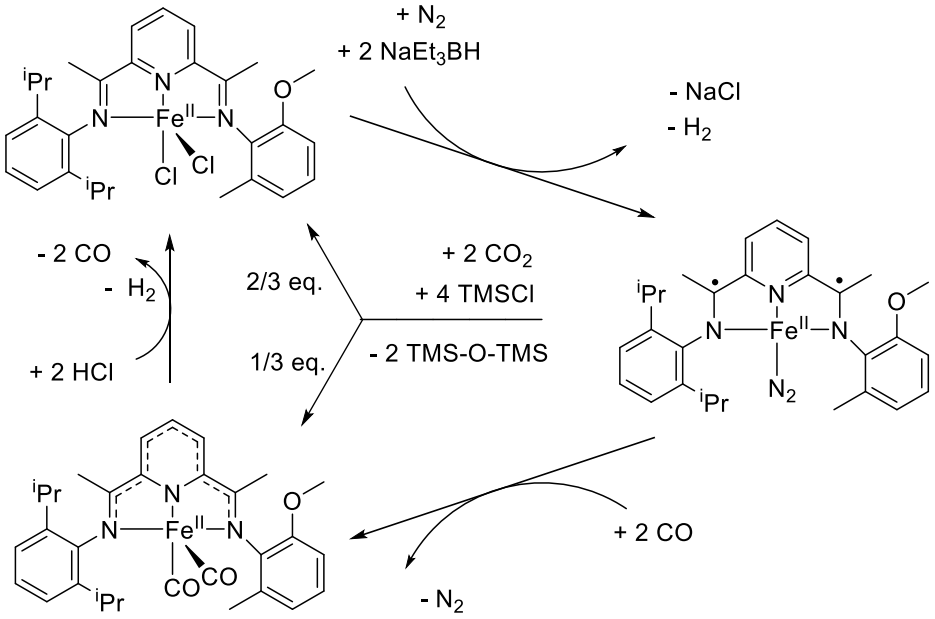

The first problem highlighted above is technically possible to overcome, as it is possible to oxidize the $Fe(PDI)(CO)_2$ back to $Fe(PDI)Cl_2$ by addition of hydrochloric acid. This results in proton reduction by the reduced ligand, and subsequently releases of CO, being replaced by Cl^-. However, this requires additional workup and cannot be performed during the reaction cycle. A method of regenerating the starting material *in situ* would be desirable, as this would be catalytic.

As mentioned previously, the $NaEt_3BH$ used in the reduction of the initial compound necessitates lower temperatures (-35˚C) to favor the kinetic product (reduction of the ligand backbone), rather than the thermodynamic product (deprotonation of the CH_3 acetyl protons), the latter leading to product decomposition. As this reductant is expensive,[80] especially when considering its one-time use, a regenerable hydride transfer agent would be advantageous. If

successful in finding a hydride transfer catalyst that was amenable to our CO_2 reduction system, a tandem catalytic system[81] was envisioned for the purposes of reducing CO_2 to CO.

5.1 Hydride Transfer Catalysis

There is substantial precedent for hydride transfer catalysts in the literature to develop alternatives to using traditional borohydride reagents, which are often expensive to produce and regenerate.[82–84] There are numerous transition metal complexes that can generate metal-hydrides by heterolytic cleavage of gaseous H_2, each with varying hydride donor abilties. The hydride transfer catalyst chosen for the tandem catalyst described above must have sufficient hydride donor capability toward reduction of CO_2, however be mild enough that the Fe(PDI) can tolerate the reductant without decomposition. The hydride donor ability (also known as hydricity; $\Delta G°_{H^-}$) of various metal and organic hydrides can be seen in Table 5.1, where a lower hydricity values indicate stronger hydride donors.

Table 5.1 Hydricity values of selected metal and organic hydride donors in acetonitrile.[85]

Hydride Donor	$\Delta G°_{H^-}$ (kcal/mol)	Hydride Donor	$\Delta G°_{H^-}$ (kcal/mol)
H_2	76	$[HPd(depe)_2]^+$	43.0
HCO_2^-	44	$[HPt(dmpe)_2]^+$	41.4
BEt_3H^-	26	$[HCo(dppe)_2]^+$	49.9
BH_4^-	50	$[HNi(dppe)_2]^+$	62.8
HCO^-	-10	$[HNi(dmpe)_2]^+$	49.9

Ligand abbreviations; dmpe = 1,2-bis(dimethylphosphinoethane), depe = 1,2-bis(diethylphosphinoethane), and dppe = 1,2-bis(diphenylphosphinoethane).

The hydride transfer catalyst(s) chosen for the tandem system will need to strong enough donors to reduce the Fe(PDI), however must be poorer hydride donors than that of $[HBEt_3]^-$ as

these will decompose the complex. A range of compounds fit that criteria, including $[HPd(depe)_2]^+$, $HCo(dppe)_2$ and $[HNi(dmpe)_2]^+$, and the weakest hydride donor, $[HNi(dmpe)_2]^+$ was chosen as a starting point.

Synthesis of $[HNi(dmpe)_2]^+$ was performed according to literature preparations.[86] Inside an N_2-filled glovebox. 1,3-dimethylphosphinoethane (1.0 g, 6.66 mmol) was dissolved in 60 mL of THF and placed into a LN_2 submerged cold-well to freeze the solution. The solution was allowed to thaw slightly and with strong stirring, bis(cyclooctadiene)nickel(0) (1.832, 6.66 mmol) was added to the solution, which was allowed to slowly warm to room temperature and react overnight. Ammonium hexafluorophosphate (1.182 g, 13.32 mmol) was added to the solution and stirred for an additional 30 mins. The solution was concentrated down to 10 mL, which precipitated out a bright yellow solid, the desired $[HNi(dmpe)_2][PF_6]$ which was isolated, washed with diethyl ether and stored in the glovebox freezer.

Scheme 5.2 Mechanism of hydride transfer to FePDI compounds.

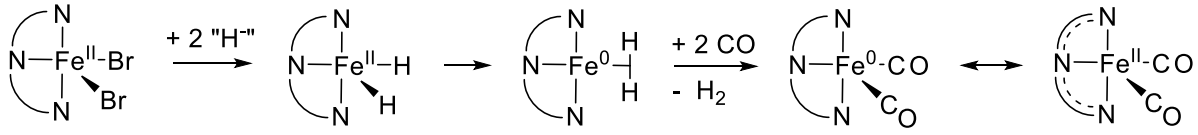

To test whether $[HNi(dmpe)_2][PF_6]$ was a strong enough hydride donor to reduce the iron (II) PDI complexes, **$2FeBr_2$** was set up with $[HNi(dmpe)_2][PF_6]$ under a CO atmosphere. CO does not bind to the neutral Fe(PDI) compounds,[30] so formation of **$2Fe(CO)_2$** would necessitate reduction by the hydride donor, as shown in Scheme 5.2.

To perform these reactions, **2FeBr$_2$**, [HNi(dmpe)$_2$][PF$_6$] and 10 mL of DCM were added to a Fisher-Porter tube along with a stir bar inside the glovebox and sealed with a pressure gauge. The vessel was charged with 25 psi CO and stirred overnight where the solution went from blue to the familiar dark forest green of the reduced iron(II) dicarbonyls. The CO was pulled off and the solution dried under vacuum and worked up inside the glovebox by dissolving in diethyl ether and filtering through celite. The ν_{CO} bands at 1946 and 1883 cm^{-1} (Figure 5.1) are seen in the IR spectra, indicating formation of the doubly reduced **2Fe(CO)$_2$**, thus validating use of [HNi(dmpe)$_2$][PF$_6$] as an adequate reductant for the Iron (II) PDI complexes. This also implies that the hydride donor ability is similar to [HNi(dmpe)$_2$]$^{+,}$ with a hydricity at least 49.9 kcal/mol.

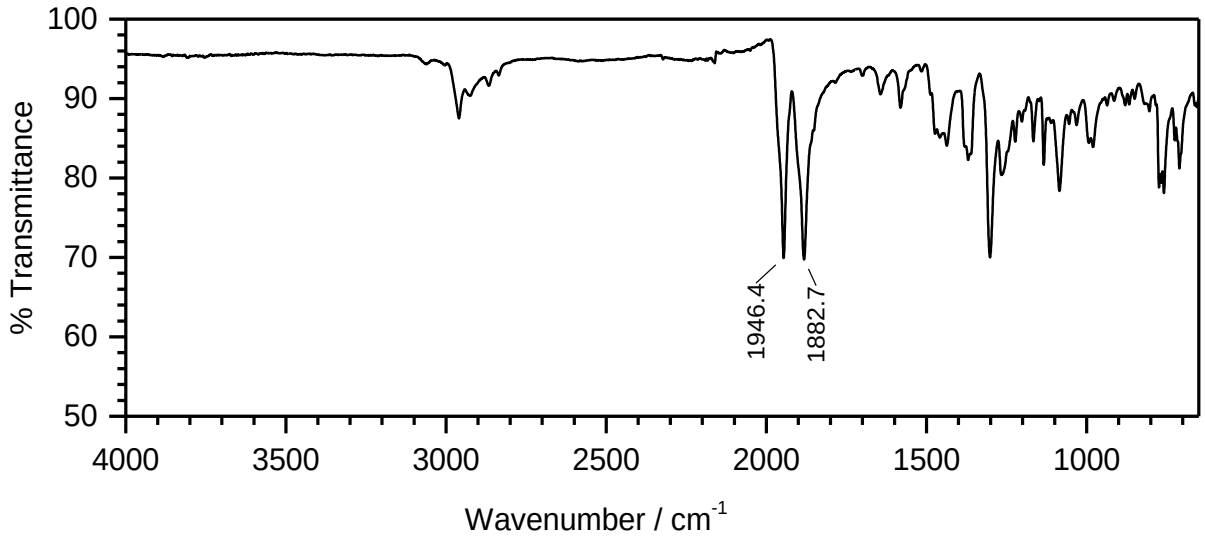

Figure 5.1 Solid FT-IR spectra of product from [HNi(dmpe)$_2$][PF$_6$] reduction under CO.

With the NiH(dmpe)$_2$ proven to transfer hydride to the iron (II) complex, the next step was to combine **2FeBr$_2$** and Ni(dmpe)$_2$[PF$_6$]$_2$ under a mixture of CO and H$_2$ to determine if the hydride catalyst could be generated *in situ* to form **2Fe(CO)$_2$**. Similar to the previous experiment, if the

hydride catalyst was generated, it was shown to transfer hydride to $2FeBr_2$, thus formation of **$2Fe(CO)_2$** would confirm generation of the hydride transfer catalyst.

Inside the glovebox, a vial was charged with **$2FeBr_2$** (0.200 g, 0.304 mmol), $Ni(dmpe)_2[PF_6]_2$ (0.1975 g, 0.304 mmol), triethylamine (0.3076 g, 3.04 mmol), 15 mL of acetonitrile and a stir bar. The vial was placed in a Parr reactor, sealed and brought outside the glovebox where it was charged with H_2 and CO. High pressures of H_2 have been shown to be necessary for the formation of some of these hydride catalysts.[83] The experiment described above was performed under various conditions, varying the pressure of H_2 (0.5 – 5 atm), temperature (25°C – 50°C) and time allowed to react (12 hours to 7 days). Only under the extreme conditions of each was there any observed reaction. After 7+ days at 50°C under 5 atm pressure of H_2, the formation of a purple solution was observed. FT-IR analysis of the resulting solution showed extremely small ν_{CO} bands at 1961 and 1899 cm^{-1}, indicating minority product formation of **$2Fe(CO)_2$**, however it was entirely too slow to be useful, as the ν_{CO} peaks in the reaction solution were not present when not run for at least 7 days.

From these initial experiments, it is clear the tandem catalysis approach to CO_2 reduction would fail in its current state as the dicarbonyl product is not formed in appreciable quantities even when CO is present. As $[HNi(dmpe)_2][PF_6]$ has already successfully been shown to transfer hydrides to the iron(II) PDI complex, the likely explanation for the failed system is the base. Triethylamine, with a pK_a of 18.8 in acetonitrile, is likely not a strong enough base to deprotonate the dihydride species to form the Ni(IV)-hydride seen in Scheme 5.3. The use of stronger bases, such as DBU (pK_a = 24.3) and Verkade's superbase (pK_a = 32.9) have been shown to substantially

increase turnover number in these hydride transfer catalysts.[87] However, these bases will decompose the complex by deprotonating the alpha proton of the imine ($pK_a \approx 22$).[88] Since the use of a stronger base is necessary, but incompatible with the current ligand, design of a pyridinediimine ligand backbone that can withstand stronger bases is necessary.

Scheme 5.3 Tandem Catalysis. Catalytic $[HNi(dmpe)_2]^+$ formation with H_2 to form hydride transfer catalyst for ligand-based CO_2 reduction on FePDI to form CO.

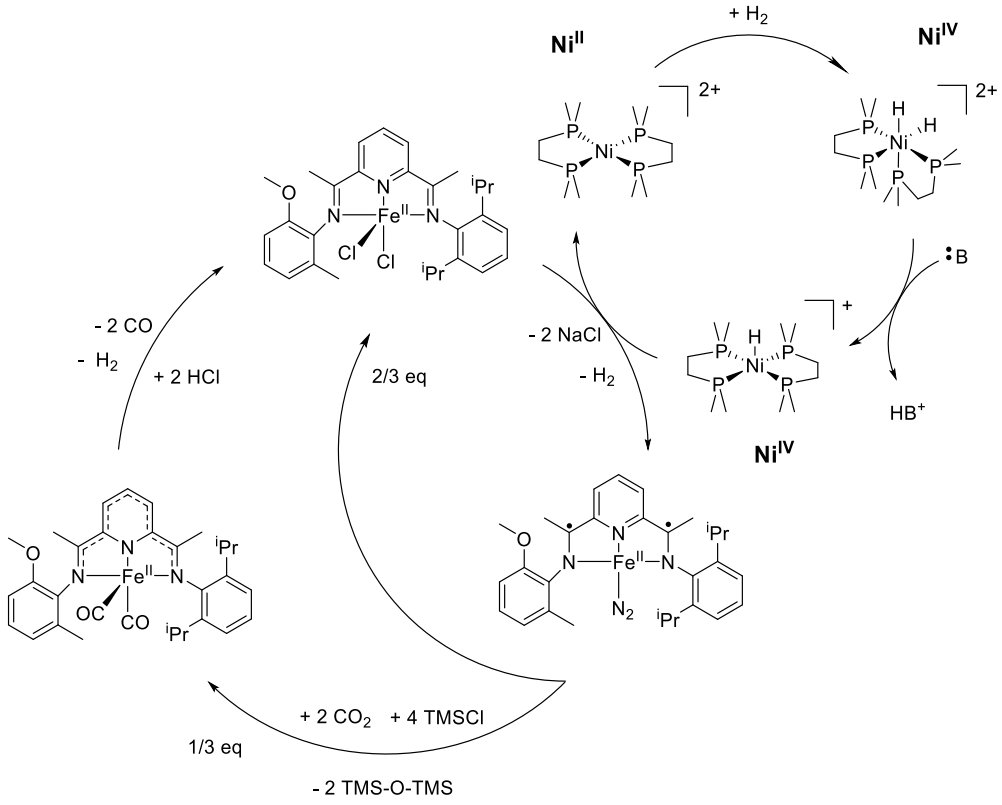

5.2 Design of Base-Safe Ligands

As mentioned above, the base used must be sufficiently basic enough to deprotonate the $[(H)_2Ni^{IV}(dmpe)_2]^{2+}$ species to form the $[HNi^{II}(dmpe)_2]^{+}$, however not too basic or it would lead to decomposition of the complex. Triethylamine (pK_a = 18.8) is insufficient in facilitating the turnover, and stronger bases like DBU (pK_a = 24.3) lead to decomposition of the complex. There are not many organic bases in this pK_a window, so instead we decided to design the ligand scaffold to be more resistant to strong bases, leading to a family of dibenzoyl PDI complexes.

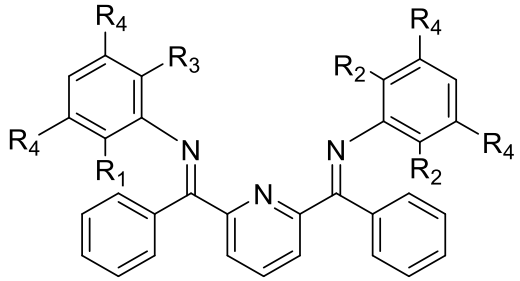

	(7)	(8)	(9)	(10)	(11)
R_1	^{i}Pr	H	H	Me	Me
R_2	^{i}Pr	H	H	Me	^{i}Pr
R_3	^{i}Pr	H	Bpin	Me	OMe
R_4	H	^{t}Bu	H	H	H

Figure 5.2 Base-safe ligand designs.

Figure 5.2 shows a few of the ligand scaffolds synthesized to be resistant to strong base. The exchange of the methyl groups for phenyl leads to much less protic C-H bonds. Ligand **7** is a direct analogue to the classic symmetric PDI backbone investigated by Chirik.[27] Ligand **8** was designed with bulky tert-butyl groups to increase the solubility in non-polar solvents such as diethyl ether. Ligand **9** was designed as an attempt to position a Lewis Acid in the secondary coordination sphere, like the Na-crown system.

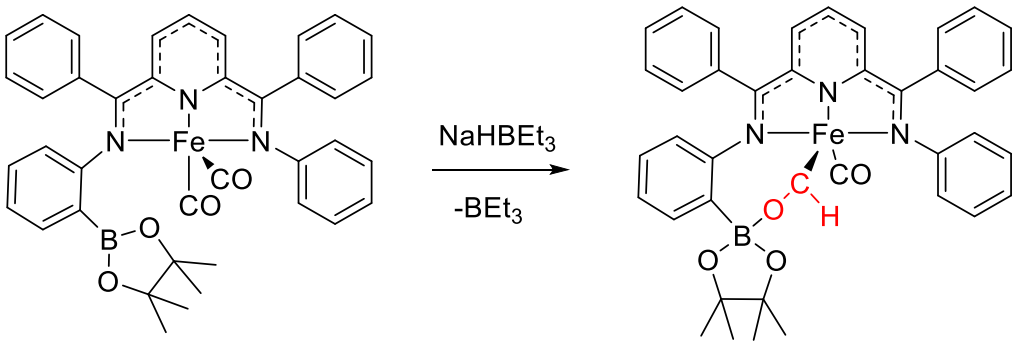

(**11**)

Here, the Lewis acid could act to stabilize reactive intermediates such as formyl (eq. 11), which is formed by hydride transfer to bound CO molecules, similar to the Miller system seen below in Scheme 5.4.[89] This facilitation of hydride transfer could be used to further reduce the CO formed during the reduction of CO_2 in the previous system, and if incorporated into the tandem catalysis system would allow for multiple catalytic turnovers.

Scheme 5.4 Pendant Lewis acid stabilized reductive coupling of carbon monoxide.

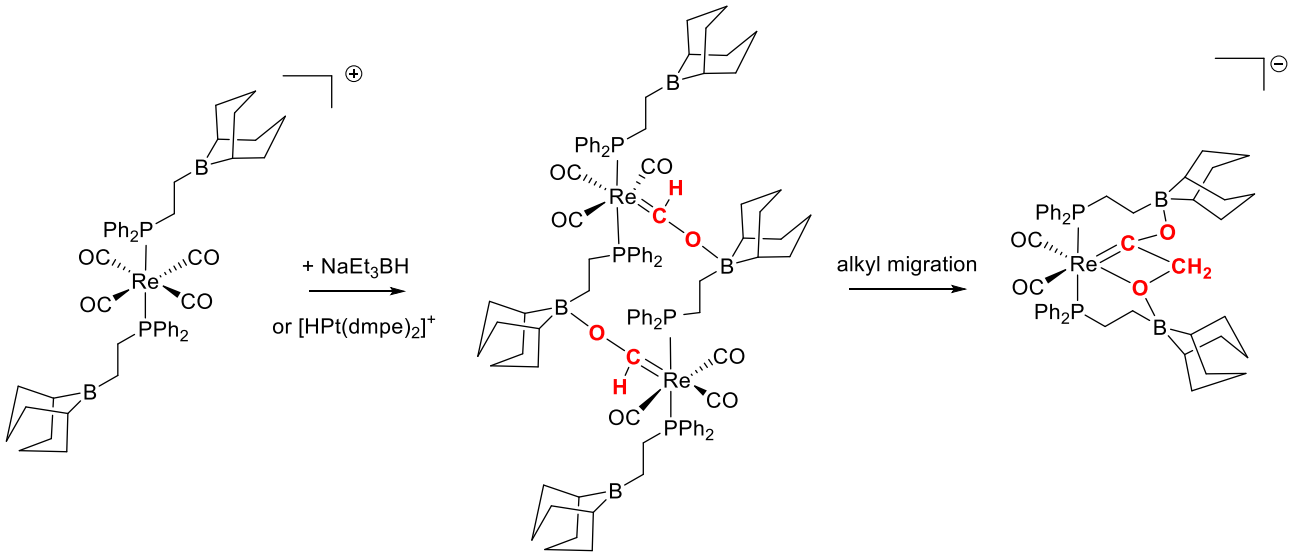

Ligand **10** was designed to be less sterically bulky than the diisopropyl derivative. This compound was successfully utilized to stabilize rare square-planar Cu^{I}-PDI complexes.[90] Finally,

ligand **11** is an analogue to the ligand employed in the previous CO_2 reduction studies, **3Fe(CO)$_2$**. Each of these ligands was designed to be more stable to strong bases, though the secondary sphere alterations vary in purpose.

5.3 Synthesis and Characterization of Base-Safe Metal Ligand Complexes

The common starting material 2,6-dibenzoylpyridine (**6**) was formed according to a slightly modified literature preparation, seen in eq. 12.[91] Inside an N_2-filled glovebox, 2,6-pyridinedicarbonyl dichloride (5.00 g, 24.5 mmol), aluminum chloride (12.5 g, 61.25 mmol), 60 mL benzene and a stir bar were added to a 250 mL round bottom flask. The flask was equipped with a condenser and brought outside the box where the water lines were attached, and the flask was placed in an oil bath to reflux for 12 hours.

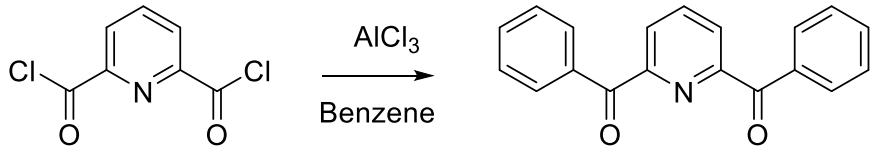

6 (**12**)

The red solution was cooled to room temperature while 150 mL deionized water was chilled to 0° C. With strong stirring, the water was slowly added to the flask to quench the aluminum chloride. Additional water was added until the solid dissolved. The organic layer was separated, and the aqueous layer was extracted with cold diethyl ether (10 mL x 5). The organic phases were combined and placed in the freezer to precipitate the desired product.

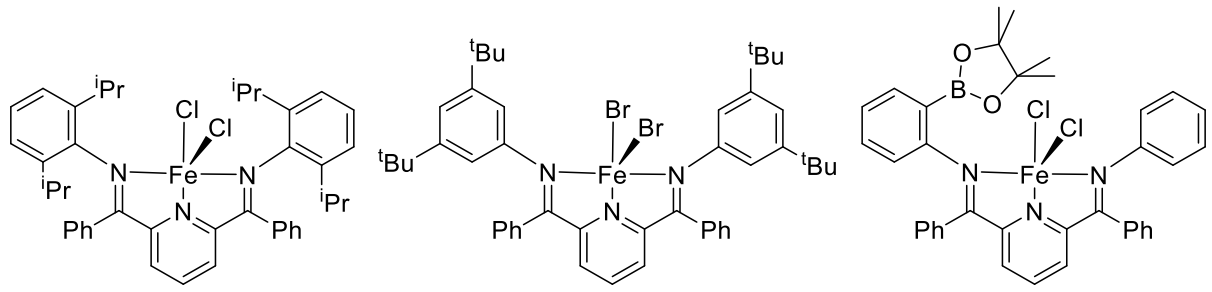

$7FeCl_2$ **$8FeBr_2$** **$9FeCl_2$**

Figure 5.3 FePDI complexes formed from dibenzoyl backbone.

$7FeCl_2$, **$8FeBr_2$** and **$9FeCl_2$** (Figure 5.3) were all synthesized using the metal templated Schiff-base condensation method utilized in section 2.2, though two equivalents of the corresponding aniline were added (**7**: 2,6-diisopropylaniline; **8**: 3,5-di-tert-butylaniline; and **9**: 2-aminophenylboronic acid pinacol ester). Interestingly, ligand **9** was not the desired target, and was initially intended to be symmetric, with each aryl arm featuring the Lewis acidic boronic ester group, Bpin. The symmetric product was never successfully synthesized, consistently forming the asymmetric product as described. Likely, the boronic ester of the second arm is cleaved through protodeboronation with the H_2O formed in the Schiff-base of the first addition, leaving an unsubstituted phenyl ring as the second arm.

ORTEP views of the solid-state crystal structures of **$7FeCl_2$**, **$8FeBr_2$**, **$8Fe(CO)_2$**, **$9FeCl_2$** and **$9Fe(CO)_2$** can be seen in the experimental, E57-E61. **$8Fe(CO)_2$** and **$9Fe(CO)_2$** were prepared identically to the reduction method described in chapter 2.

5.4 Future Work

Preliminary work has successfully synthesized a few of the FePDI complexes featuring the dibenzoyl backbone that should stand up to stronger bases such as DBU, however additional work will need to be done to answer a few keys questions before these compounds can be used in the tandem catalysis approach. 1) Will these complexes hold up to DBU and Verkades' superbase? They will need to be subjected to these bases to determine their chemical stability. 2) Will these compounds participate in the ligand-based reduction of CO_2 to CO? The activity toward CO_2 reduction to form the corresponding Fe(PDI)$(CO)_2$ using the methods previously developed using **2Fe(CO)$_2$** must be determined. 3) Is the hydride donor ability of $[HNi(dmpe)_2]^+$ sufficient to reduce these FePDI complexes? The same tests described in section 5.1 must be performed. If the chemistry works as envisioned, at this point, one of these complexes should be able to participate in the tandem catalysis system facilitated by DBU or Verkades' superbase.

Chapter 6 – Conclusions

Kinetic enhancement of small molecule reductions has been shown through installation of pendant Lewis acidic and Lewis basic sites. Encapsulation of redox inactive alkali metal ions into pendant crown ethers result in modest shifts in reduction potential, as the Lewis acidic metal ions are effectively uncoupled from the ligand-based redox sites on the iron (II) PDI complexes. The strength of the interaction can be probed through salt titration experiments, where Na^+-crown interactions can entice reactive anion species into the secondary coordination sphere. This feature has been successfully utilized to enhance reaction kinetics of nitrite reduction to nitrous oxide by a factor of 3.5, forming a dinitrosyl iron complex (DNIC). Future investigations of kinetic enhancement on PDIs will be aimed at determination of the mechanism.

The development of redox active tripodal ligands is still in early stages. Mild redox-activity has been observed in the tripodal framework featuring imines, however these complexes are unstable. Future investigations will expand on this idea by synthesizing the ketimine forms rather than the aldimines, installing redox-active metals and varying the secondary sphere functional groups to fully explore the potential of these ligand frameworks. Successful development of a redox active tripodal framework could expand the synthetic toolbox available to inorganic chemists.

Base-safe ligand designs based on the dibenzoylpyridine backbone have been synthesized, though have not been fully characterized. Like the tripodal ligand project, this work is still in its infancy. Future work will include fully characterizing these complexes, followed by reactivity

studies by employing the tandem catalyst methods we have proposed by first testing the Fe(PDI) complexes against stronger bases to determine if they will ultimately be stable. If stable to stronger bases such as DBU, which is sufficiently basic enough to deprotonate the dihydride nickel complex to form the active hydride transfer agent, these complexes can be set up with $[Ni(dmpe)_2]^{2+}$ under CO and H_2 with DBU to form $Fe(PDI)(CO)_2$. DBU is sufficiently basic enough to deprotonate the dihydride nickel complex to form the active hydride transfer agent, so this should form the corresponding $Fe(PDI)(CO)_2$ complexes. If this reactivity is shown, then these complexes should be able to work in tandem with the hydride transfer catalyst to ultimately reduce CO_2 to CO. If the reactivity is not shown however, and the formation of the hydride transfer catalyst from H_2 being the limiting step, the next strongest metal-hydride donor could be chosen to repeat these experiments, until a functional tandem catalysis system was discovered and optimized.

Chapter 7 – Supporting Information

7.0 General Considerations

All reagents were purchased from commercial sources and used as received. Solvents were dried and deoxygenated with a PureSolv solvent purification. ((2,6-^{i}Pr-C_6H_3)N=C(CH_3))C_5H_3N((CH3)-C=O)[92] **(1)**, ^{MeO}PDI **(2)**, Fe(^{MeO}PDI)Br_2 **($2FeBr_2$)**, Fe(^{MeO}PDI)$(CO)_2$ **($2Fe(CO)_2$)** were synthesized according to literature procedures.[30] Air sensitive materials were handled and stored on a Schlenk line or in a glovebox under N_2 atmosphere. Elemental analyses were performed by ALS Enviornmental in Tuscon, AZ.

FT-IR. Solid infrared spectra were recorded on a Thermo Scientific Nicolet iS10 FT-IR spectrometer equipped with an ATR accessory. Solution FT-IR were obtained using a Transmission accessory and a liquid IR cell equipped with CaF_2 salt plates.

FT-NMR. All NMR spectra were recorded on a Bruker 500 MHz FT-NMR spectrometer. Data are reported in ppm from the solvent resonance as the internal standard unless otherwise noted. ^{11}B spectra were recorded in a quartz J-Young tube and referenced to BF_3. ^{15}N spectra were referenced to neat nitromethane. ^{19}F spectra were referenced to 1,1,1-trifluorotoluene. ^{31}P spectra were referenced to D_3PO_4 in D_2O.

Mössbauer Spectroscopy. Mössbauer spectra were recorded at room temperature with a constant acceleration spectrometer (Wissel GMBH, Germany) in a horizontal transmission mode using a 50 mCi ^{57}Co source. Approximately 0.200 g of sample was crushed in a Mössbauer sample holder and a drop of Paratone-N was used to cover the sample to prevent oxidation. Data acquisition varied from 2 to 7 days to get a statistically reasonable spectrum for each sample to analyze. The velocity scale was normalized with respect to metallic iron at room temperature; hence all isomer shifts were recorded relative to metallic iron. The Mössbauer spectra were fitted by assuming Lorentzian line shapes using the NORMOS (Wissel GMBH) least-square fitting program. The isomershift and quadrupole splitting parameters were determined from the fitted spectra.

Electrochemistry. Cyclic voltammetry was carried out using a Pine WaveNow potentiostat employing a standard three-electrode electrochemical cell consisting of a glassy carbon working electrode, platinum auxiliary electrode and a freshly prepared Ag/$AgNO_3$ reference electrode with a Vycor tip filled with

acetonitrile. All potentials were internally referenced to the ferrocene redox couple. Unless otherwise noted, experiments were carried out under a dinitrogen atmosphere at room temperature using either acetonitrile or methylene chloride. Solutions of the analyte at 0.001 M and with 0.100 M tetra(n-butyl)ammonium hexafluorophosphate ($TBAPF_6$) as the supporting electrolyte were prepared.

UV-Vis. UV-Vis spectra and kinetics data were obtained using a Jasco V-670 Spectrometer equipped with a Peltier controlled 6-cell linear autosampler. Cuvettes were 21-Q-10 Spectrosil® quartz from Starna Cells. All data were obtained at 298K.

^{1}H NMR Titrations. In a typical experiment, a sample of **3Fe(CO)$_2$** (20 mmol) in CD_3CN (500 µL) was added to a J-young NMR tube. The Na^+ salt in CD_3CN (except in the case of $NaNO_2$ where CD_3OD was utilized) was added in 0.15 equivalent aliquots (20 µL). The resulting mixture was vigorously shaken for 15 seconds and inserted into the NMR probe and allowed equilibrate at 298 K for 10 mins before a spectrum was obtained. The tube was brought into the glovebox to add the next aliquot and the process was repeated until the titration was complete.

7.1 Synthesis and Characterization

Fe(^{MeO}PDI)(NO)$_2$[BPh$_4$] (2Fe(NO)$_2$[BPh$_4$]). A 20 mL scintillation vial was charged with **2Fe(CO)$_2$** (0.250 g, 0.452 mmol), $NaNO_2$ (0.0624 g, 0.904 mmol), $[NEt_3H][BPh_4]$ (0.798 g, 1.808 mmol), a stir bar, and 10 mL of acetonitrile. The solution was stirred for 18 h. The resulting dark orange solution was filtered through celite and dried under vacuum. Crystals were obtained by re-dissolving the solid in tetrahydrofuran, carefully layering with hexanes and setting aside for crystallization. The resulting red crystals were identified as **2Fe(NO)$_2$[PF$_6$]**. FT-IR (ATR): 1797, 1729 cm^{-1} (N=O), 830 cm^{-1} (PF_6^-).

Fe(^{Bz15c5}PDI)X$_2$ (3Fe[X]$_2$) (X = Cl$^-$, Br$^-$). Compound **1** (0.500 g, 1.551 mmol) and $FeCl_2$ (0.1965 g, 1.551 mmol) were dissolved in approximately 40 mL of ethanol into a 100 mL round bottom Schlenk flask with a stir bar. The solution was heated to 50˚C for 20 mins under N_2 gas and stirred. A solution of 4'-aminobenzo-15-crown-5 ether (0.4394 g, 1.551 mmol) in 5 mL of acetonitrile as slowly syringed into the flask and the solution was left to heat at 78˚C for 12 hours under N_2 gas. The solvent was removed in vacuo and a dark green solid was obtained. In the glovebox, the resulting solid was re-dissolved in 30 mL of CH_2Cl_2 and filtered through celite. The filtrate was layered with ether and set aside for crystallization. Green crystals identified as **3FeCl$_2$** were isolated in 69% yield. ^{1}H NMR (500 MHz, CD_2Cl_2), ^{13}C NMR (125 MHz, CD_2Cl_2) δ

78.16, 77.54, 73.12, 52.97, 45.01, 16.52, 13.11, 4.65, 3.14, 3.10, 2.91, 2.81, 1.78, 1.17, 0.99, -0.82, -2.22, -5.63, -8.11, -23.33, -24.38, -27.74, -39.81. Anal. Calc'd for $C_{35}H_{45}Br_2FeN_3O_5$: C, 52.32; H, 5.65; N, 5.23. Found: C, 56.67; H, 7.13; N, 6.48.

Fe(^{Bz15c5}PDI)(CO)$_2$ (3Fe(CO)$_2$). In a nitrogen filled glovebox, compound **3FeX$_2$** (0.300 g, 0.420 mmol), sodium mercury amalgam (0.4054 g, 5% Na), approximately 10 mL of CH_2Cl_2, and a stir bar were added to a Fisher Porter tube. The tube was closed with a pressure valve, taken out of the box, charged with 35 psi of CO, and the solution was stirred vigorously overnight. The solvent was removed by vacuum and brought into the glovebox. The green solid was re-dissolved in 40 mL of diethyl ether and filtered through a celite plug. Slow evaporation of diethyl ether yielded dark green crystals identified as **3Fe(CO)$_2$** in 71% yield (0.130 g, 0.196 mmol). FT-IR (ATR): 1948, 1886 cm^{-1} (C=O). ^{1}H NMR (500 MHz, CD_2Cl_2) δ 8.16 (dd, 2H), 7.58 (t, 1H), 7.23 (m, 3H), 6.86(d, 1H), 6.68 (d, 1H), 6.64 (dd, 1H), 4.14 - 3.70 (m, 16H), 2.51 (sept, 2H), 2.46 (s, 3H), 2.38 (s, 3H), 1.21 (d, 6H), 1.01 (d, 6H). ^{13}C NMR (125 MHz, CD_2Cl_2) δ 15.52, 16.45, 24.39, 27.25, 68.46, 69.00, 69.38, 70.17, 70.78, 109.21, 112.70, 114.71, 117.44, 120.85, 121.21, 123.45, 126.13, 140.15, 144.50, 146.72, 148.41, 149.58, 155.19, 156.32, 198.33, 214.03. Anal. Calc'd for $C_{37}H_{45}FeN_3O_7$: C, 63.52; H, 6.48; N, 6.01. Found: C, 61.05; H, 7.28; N, 6.57.

[Fe(^{Bz15c5}PDI)(CO)$_2$Na][PF$_6$] (3Fe(CO)$_2$Na[X]) (X = PF$_6^-$, BPh$_4^-$, BH$_4^-$, NO$_2^-$). A 20 mL scintillation vial was charged with **3Fe(CO)$_2$** (0.250 g, 0.357 mmol), the appropriate Na^+ salt (0.357 mmol), a stir bar and approximately 5 mL of CH_3CN (2 mL of MeOH was also added in the case of NO_2^- to help with solubility). The solution was stirred overnight. The solvent was removed via vacuum and re-dissolved in 5 mL of CH_2Cl_2. The dark green solution was filtered through celite, carefully layered with pentane and set aside for crystallization. X-ray quality crystals were obtained of the PF_6^-, BPh_4^-, and BH_4^-. FT-IR (ATR): 1929, 1857 cm^{-1} (C=O); 734, 707 cm^{-1} (BPh_4^-). ^{1}H NMR (500 MHz, CD_2Cl_2) δ 8.22 (t, 2H), 7.64 (s, 1H), 7.34 - 6.83 (br, 26H), 4.15 - 3.68 (br, 16H), 2.51 - 2.44 (br, 8H), 1.24 (s, 3H), 1.05 (s, 3H). ^{13}C NMR (125 MHz, CD_2Cl_2) δ 214.28, 164.55, 164.16, 163.77, 163.38, 157.28, 154.99, 149.48, 145.79, 145.40, 144.23, 140.18, 135.93, 126.29, 125.61, 123.55, 121.16, 116.45, 112.45, 109.15, 68.90, 68.52, 68.10, 67.99, 67.30, 67.05, 27.30, 24.41, 16.58, 15.69. Anal. Calc'd for $C_{61}H_{65}BFeN_3O_7$: C, 70.32; H, 6.29; N, 4.03. Found: C, 61.05; H, 7.28; N, 6.57.

[Fe(^{Bz15c5}PDI)(NO)$_2$Na][X]$_2$ (3Fe(NO)$_2$[X]$_2$) (X = Cl$^-$, PF$_6^-$, BPh$_4^-$). A 20 mL scintillation vial was charged with **3Fe(CO)$_2$** (0.250 g, 0.357 mmol), $NaNO_2$ (0.050 g, 0.714 mmol), [NEt_3H][X] (1.428 mmol), a stir bar and approximately 10 mL of CH_3CN. The solution was stirred for 18 h. The resulting dark orange solution was

filtered through celite and dried under vacuum. Crystals were only obtained using the PF_6^- acid where the solid was re-dissolved in 5 mL of tetrahydrofuran and then carefully layered with 10 mL of toluene and set aside for crystallization. The resulting orange crystals were identified as **$3Fe(NO)_2[PF_6]_2$**. FT-IR (ATR): 1784, 1712 cm^{-1} (N=O), 828 cm^{-1} (PF_6^-). ^1H NMR (500 MHz, CD_2Cl_2) Anal. Calc'd for $C_{35}H_{45}F_{12}FeN_5O_7P_2$: C, 41.35; H, 4.46; N, 6.89. Found: C, 61.05; H, 7.28; N, 6.57.

$N(EtN=C(CH)(C_6H_5))_3$ (4). Tris(2-aminoethyl)amine (4.85 g, 33.1 mmol) and benzaldehyde (10.55 g, 99.3 mmol) were added to a 250 mL round bottom flask along with 100 mL of acetonitrile and refluxed for 6 hours. The solvent was pulled off under vacuum to leave the desired product, a white solid.

$4Zn(OTf)_2$. In a nitrogen filled glovebox, a vial was charged with a stir bar, compound **7**, 1 eq. of zinc trifluoromethanesulfonate and 15 mL of acetonitrile. The solution was filtered through celite and carefully layered with ether to obtain clear, colorless x-ray quality crystals.

$N(o\text{-}(C_6H_4)NH_2)_3$. 2-nitroaniline (2.5 g, 18.1 mmol), 1-fluoro-2-nitrobenzene (10.17 g, 72.1 mmol), potassium carbonate (15.0 g, 108.5 mmol) and 50 mL of DMSO were added to a round bottom flask and heated at 150˚C under an N_2 atmosphere for 84 hours. The solution was allowed to cool and all contents were poured into 1 L of water with strong stirring. The solid was filtered and re-dissolved in hot methanol. After a second filtration, the solid was washed with cold acetone, the resulting yellow solid was tris(2-nitrophenyl)amine. The deep red filtrate contains the singly substituted product and was dried under vacuo and set aside. The compound was hydrogenated to the corresponding amines using Pd on carbon. Tris(2-nitrophenyl)amine (2.00 g), 10% Pd/C (0.50 g), a stir bar and 25 mL of tetrahydrofuran were added to a pressure vessel inside of a glovebox and sealed with a pressure gauge. The vessel was initially charged with 40 psi of H_2 and the slurry was stirred vigorously. The vessel was periodically recharged with more H_2 until the pressure was maintained. The Pd/C was filtered through a fritted funnel and the solution was pulled dry under vacuum to yield a yellow solid confirmed to be the desired precursor of tris(2-aminophenyl)amine.

$5Zn(OTf)_2$. A 100 mL Schlenk flask was charged with Tris(aminophenyl)amine (0.25 g, 0.861 mmol), benzaldehyde (0.274 g, 2.583 mmol), zinc triflate (0.313 g, 0.861 mmol), and 40 mL of EtOH. This was heated under an N_2 atmosphere at 78˚C for 12 hours, brought into the box and filtered through celite. The compound was dried in vacuo yielding, and clear/colorless x-ray quality crystals were obtained by carefully layering diethyl ether on a saturated THF solution of the metallated compound.

2,6-dibenzoylpyridine (6). Inside an N_2-filled glovebox, 2,6-pyridinedicarbonyl dichloride (5.00 g, 24.5 mmol), aluminum chloride (12.5 g, 61.25 mmol), 60 mL benzene and a stir bar were added to a 250 mL round bottom flask. The flask was equipped with a condenser and brought outside the box where the water lines were attached, and the flask was placed in an oil bath to reflux for 12 hours. The red solution was cooled to room temperature while 150 mL deionized water was chilled to 0°C. With strong stirring, the water was slowly added to the flask to quench the aluminum chloride. Additional water was added until the solid dissolved. The organic layer was separated, and the aqueous layer was extracted with cold diethyl ether (10 mL x 5). The organic phases were combined and placed in the freezer to precipitate the desired product.

[(2,6-^{i}Pr-C_6H_3)N=C(C_6H_5)C_5H_3N(C_6H_5)C=N(2,6-^{i}Pr-C_6H_3)] (7$FeCl_2$). In a nitrogen filled glovebox, compound **6** (0.500 g, 1.74 mmol) and $FeCl_2$ (0.2205 g, 1.74 mmol) were added to a 100 mL Schlenk flask equipped with a stir bar and dissolved in 50 mL of ethanol. The solution was heated to 50˚C for 20 mins under N_2 gas and stirred. A solution of 2,6-diisopropylaniline (0.617 g, 3.48 mmol) in 10 mL of ethanol as slowly syringed into the flask and the solution was left to heat at 78˚C for 12 hours under N_2 gas. The solvent was removed in vacuo and a dark green solid was obtained. In the glovebox, the resulting solid was re-dissolved in 50 mL of CH_2Cl_2 and filtered through celite. The filtrate layer was layered with ether and set aside for crystallization. Green x-ray quality crystals were identified as **7$FeCl_2$**

[(3,5-^{t}Bu-C_6H_3)N=C(C_6H_5)C_5H_3N(C_6H_5)C=N(3,5-^{t}Bu-C_6H_3)] (8$FeBr_2$). In a nitrogen filled glovebox, compound **6** (0.500 g, 1.74 mmol) and $FeBr_2$ (0.3573 g, 1.74 mmol) were added to a 100 mL Schlenk flask equipped with a stir bar and dissolved in 50 mL of ethanol. The solution was heated to 50˚C for 20 mins under N_2 gas and stirred. A solution of 3,5-di-tert-butylaniline (0.7146 g, 3.48 mmol) in 10 mL of ethanol as slowly syringed into the flask and the solution was left to heat at 78˚C for 12 hours under N_2 gas. The solvent was removed in vacuo and a dark green solid was obtained. In the glovebox, the resulting solid was re-dissolved in 50 mL of CH_2Cl_2 and filtered through celite. The filtrate layer was layered with ether and set aside for crystallization. Green x-ray quality crystals were identified as **8$FeBr_2$**

8$Fe(CO)_2$. In a nitrogen filled glovebox, compound **8$FeBr_2$** (0.369 g, 0.420 mmol), sodium mercury amalgam (0.4054 g, 5% Na), approximately 10 mL of CH_2Cl_2, and a stir bar were added to a Fisher Porter tube. The tube was closed with a pressure valve, taken out of the box, charged with 35 psi of CO, and the solution was stirred vigorously overnight. The solvent was removed by vacuum and brought into the

glovebox. The green solid was re-dissolved in 40 mL of diethyl ether and filtered through a celite plug. Slow evaporation of diethyl ether yielded dark green crystals identified as **8Fe(CO)$_2$.**

[(C$_6$H$_5$)N=C(C$_6$H$_5$))C$_2$H$_3$N((C$_6$H$_5$)C=N(2-Bpin)] (9FeCl$_2$). In a nitrogen filled glovebox, compound **6** (0.500 g, 1.74 mmol) and $FeCl_2$ (0.2205 g, 1.74 mmol) were added to a 100 mL Schlenk flask equipped with a stir bar and dissolved in 50 mL of ethanol. The solution was heated to 50˚C for 20 mins under N_2 gas and stirred. A solution of 2-aminophenylboronic acid pinacol ester (0.7625 g, 3.48 mmol) in 10 mL of ethanol as slowly syringed into the flask and the solution was left to heat at 78˚C for 12 hours under N_2 gas. The solvent was removed in vacuo and a dark blue solid was obtained. In the glovebox, the resulting solid was re-dissolved in 50 mL of CH_2Cl_2 and filtered through celite. The filtrate layer was layered with ether and set aside for crystallization. Blue x-ray quality crystals were identified as **9FeCl$_2$**.

9Fe(CO)$_2$. In a nitrogen filled glovebox, compound **9FeCl$_2$** (0.289 g, 0.420 mmol), sodium mercury amalgam (0.4054 g, 5% Na), approximately 10 mL of CH_2Cl_2, and a stir bar were added to a Fisher Porter tube. The tube was closed with a pressure valve, taken out of the box, charged with 35 psi of CO, and the solution was stirred vigorously overnight. The solvent was removed by vacuum and brought into the glovebox. The green solid was re-dissolved in 40 mL of diethyl ether and filtered through a celite plug. Slow evaporation of diethyl ether yielded dark green crystals identified as **9Fe(CO)$_2$**.

7.2 FT-IR Spectra

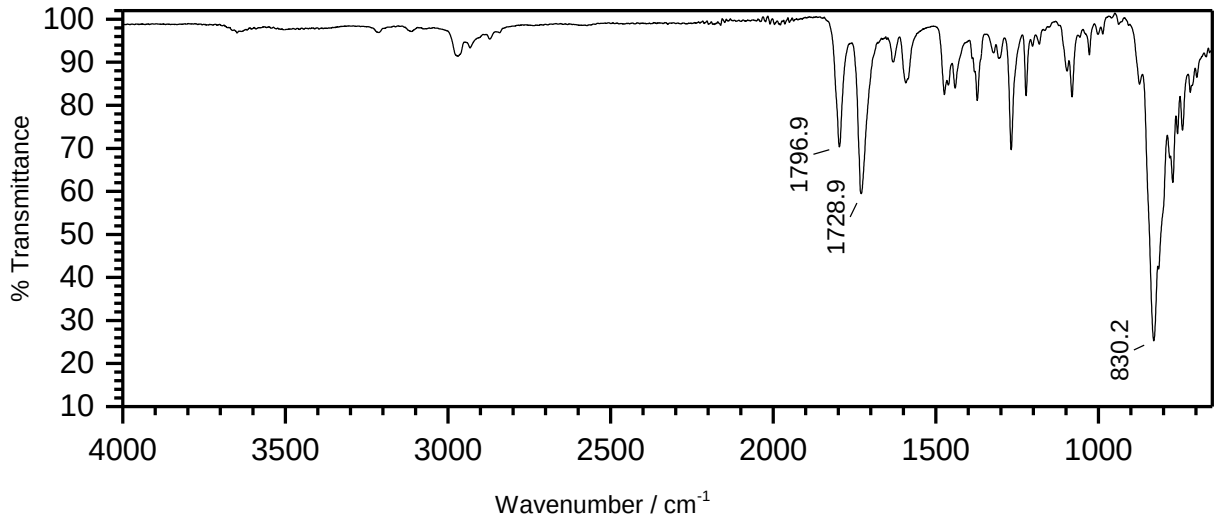

E1 Solid FT-IR spectra of **$[2Fe(NO)_2][PF_6]$**

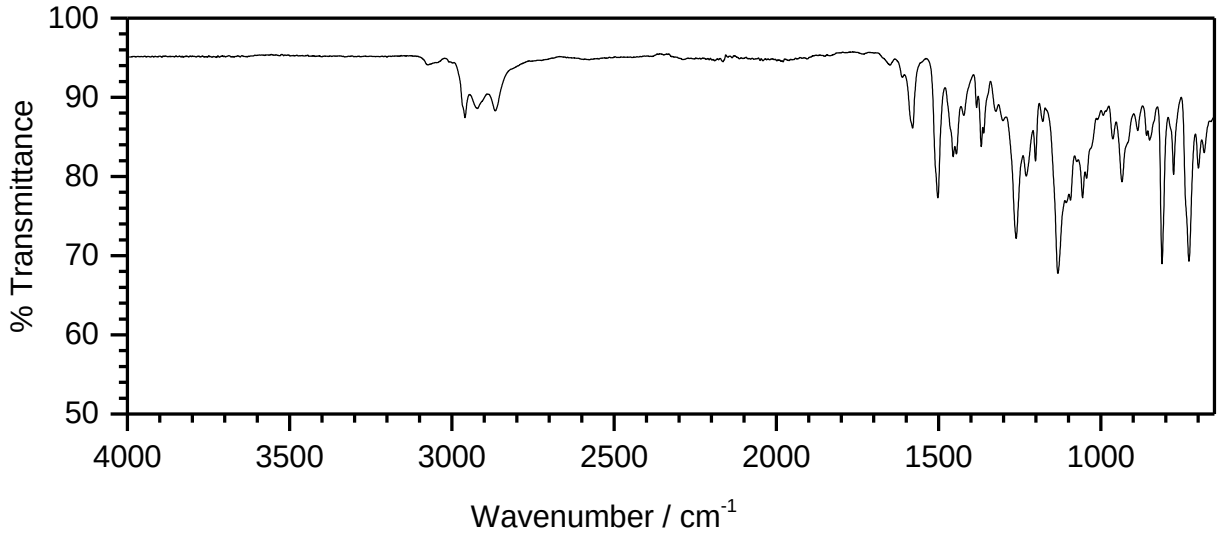

E2 Solid FT-IR spectra of **$3FeBr_2$**

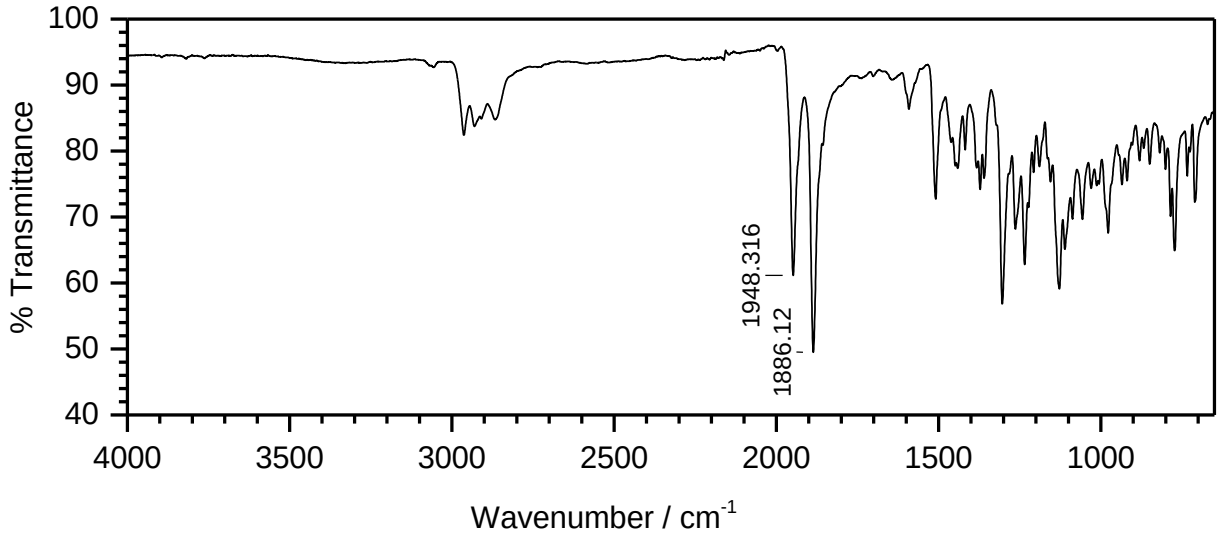

E3 Solid FT-IR spectra of **$3Fe(CO)_2$**

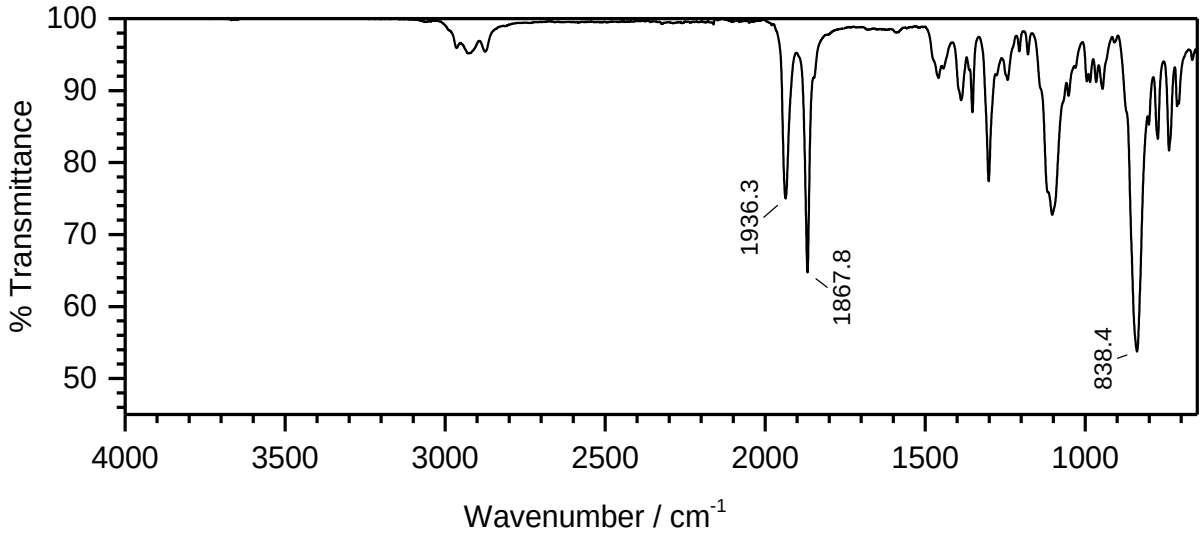

E4 Solid FT-IR spectra of **$[3Fe(CO)_2Na][PF_6]$**

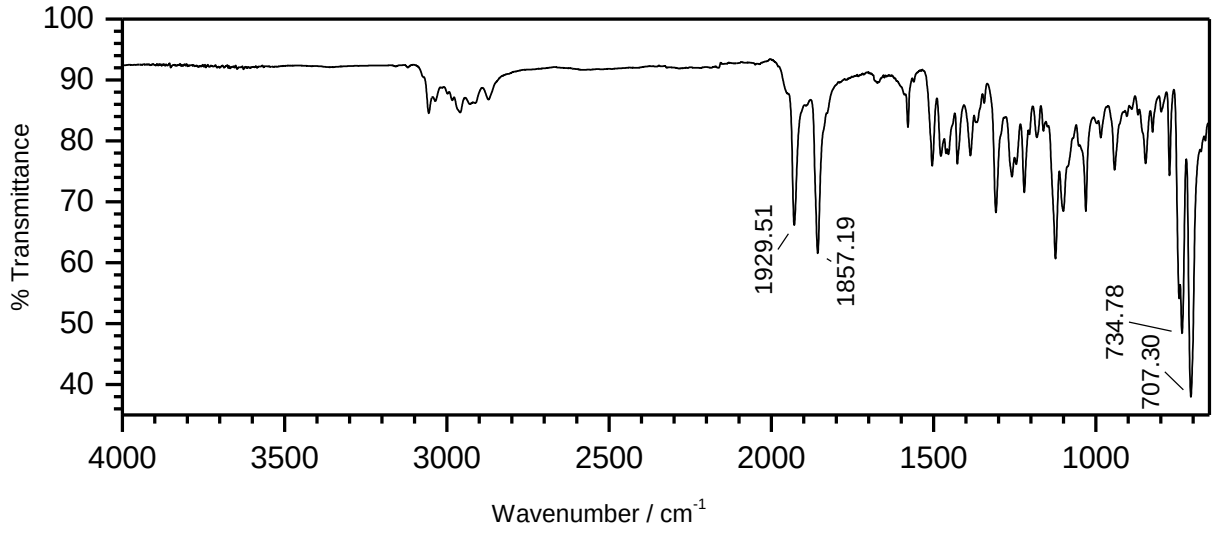

E5 Solid FT-IR spectra of **[3Fe(CO)$_2$Na][BPh$_4$]**

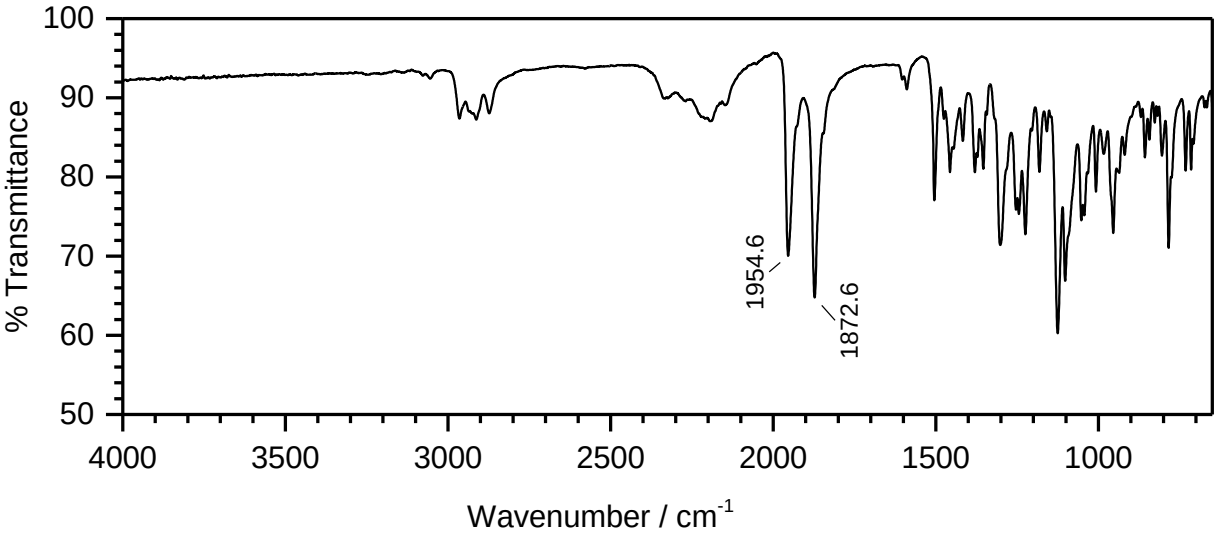

E6 Solid FT-IR spectra of **[3Fe(CO)$_2$Na][BH$_4$]**

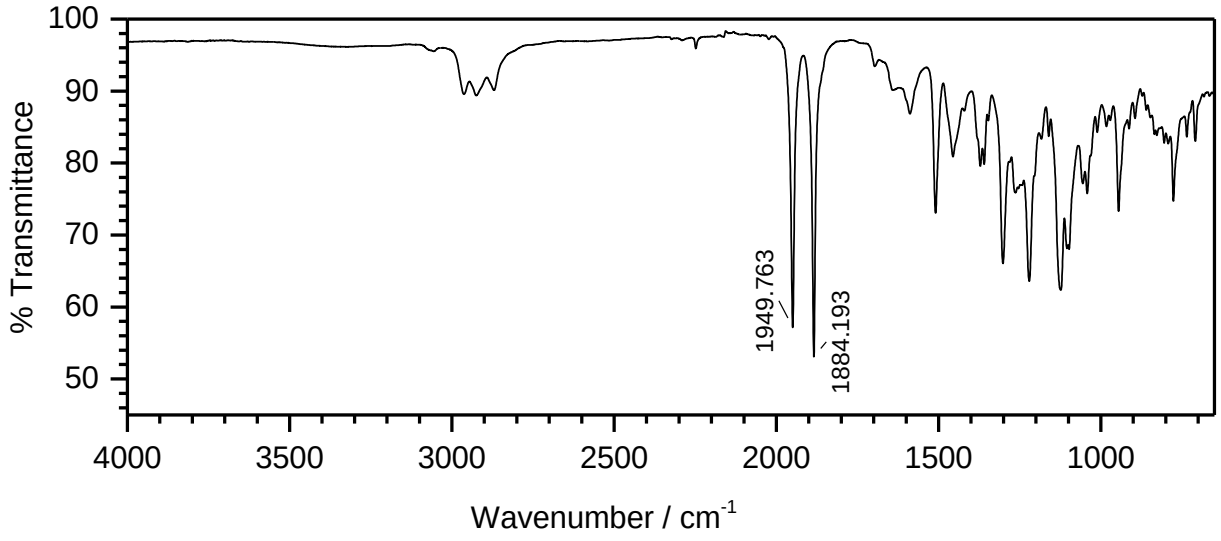

E7 Solid FT-IR spectra of **[3Fe(CO)$_2$Na][NO$_2$]**

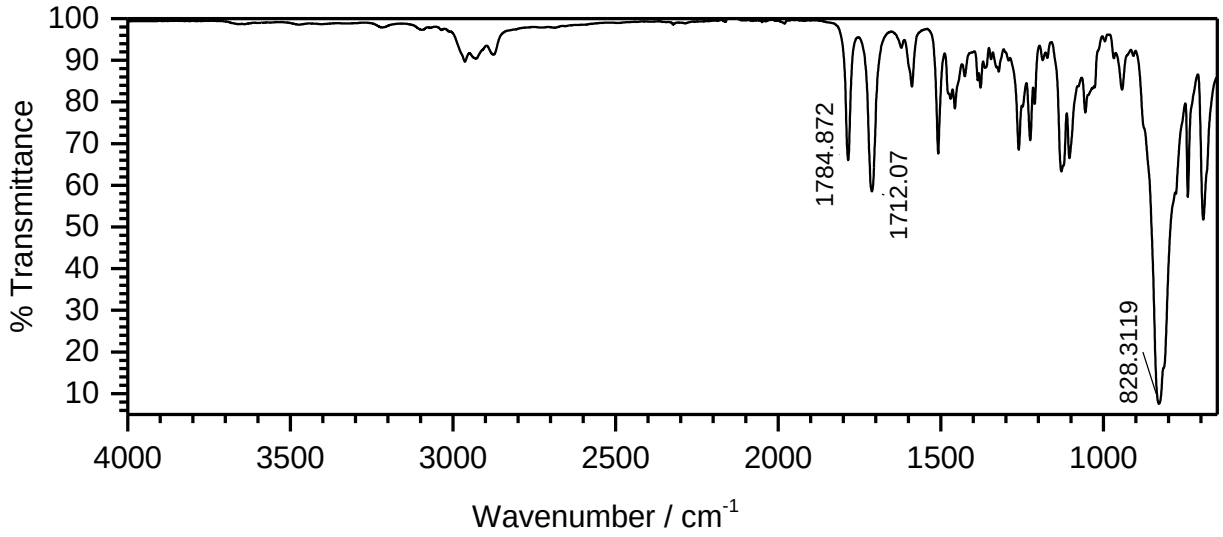

E8 Solid FT-IR spectra of **[3Fe(NO)$_2$Na][PF$_6$]$_2$**

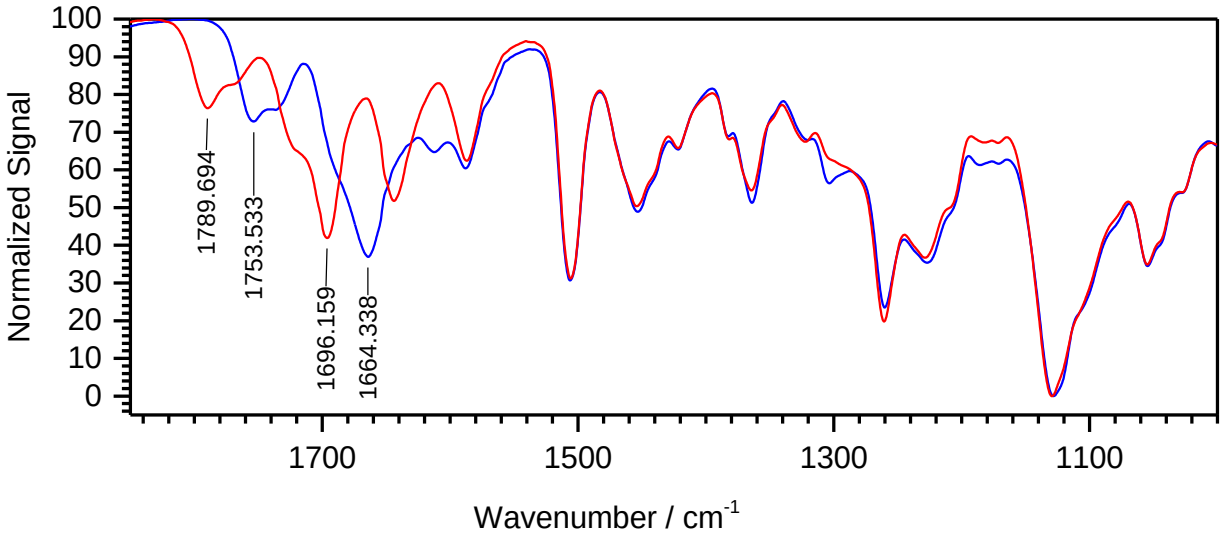

E9 Solid FT-IR spectra of **[3Fe(^{14}NO)$_2$Na][PF$_6$]$_2$** (red) vs **[4Fe(^{15}NO)$_2$Na][PF$_6$]$_2$** (blue)

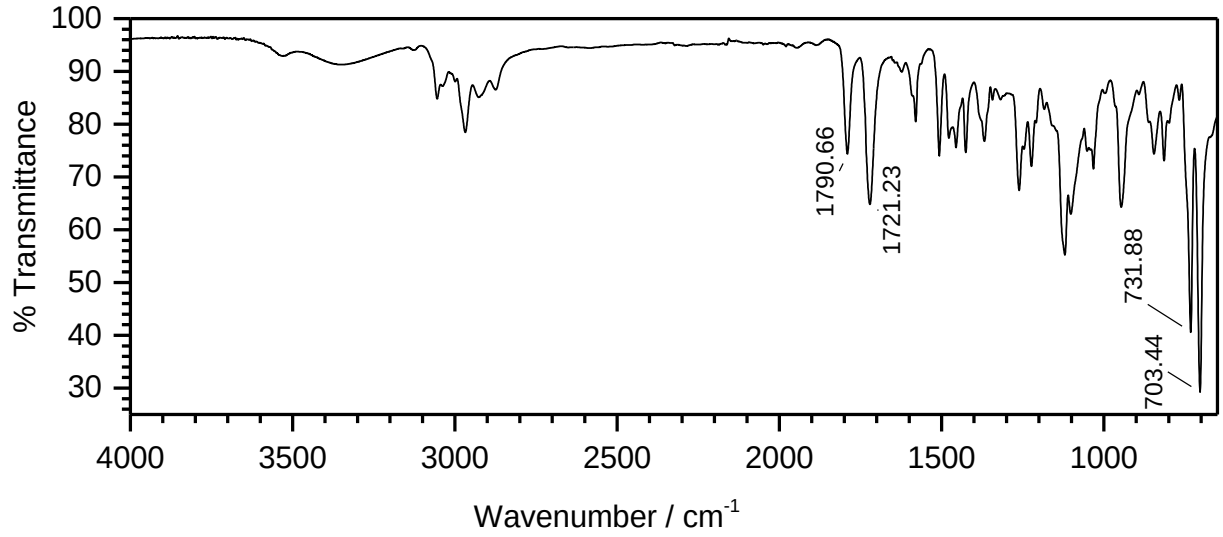

E10 Solid FT-IR spectra of **[3Fe(NO)$_2$Na][BPh$_4$]$_2$**

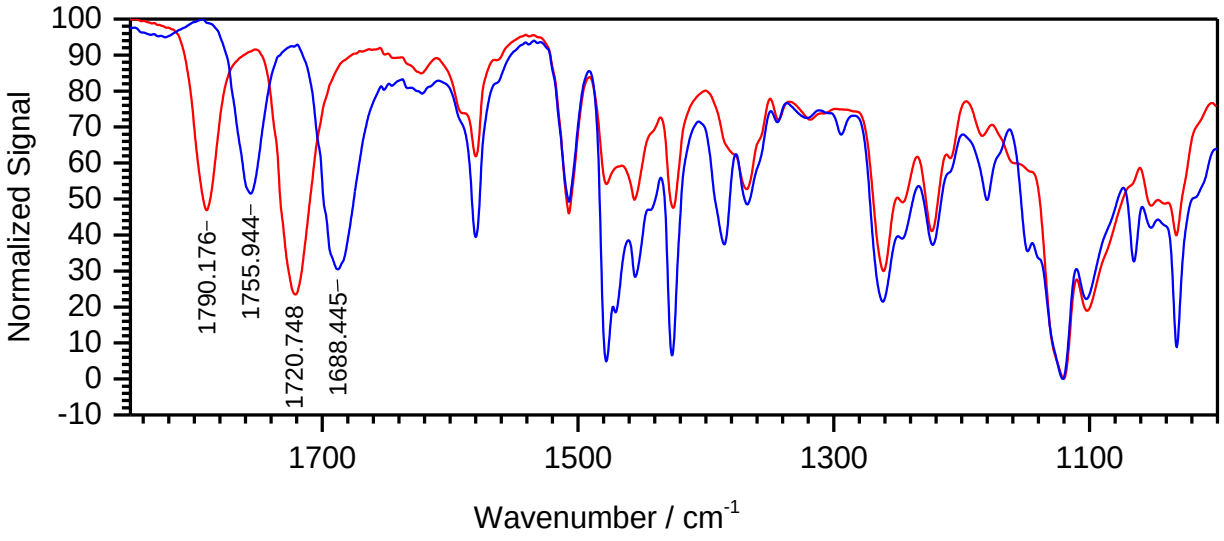

E11 Solid FT-IR spectra of **[3Fe(^{14}NO)$_2$Na][BPh$_4$]$_2$** (red) vs **[3Fe(^{15}NO)$_2$Na][BPh$_4$]$_2$** (blue)

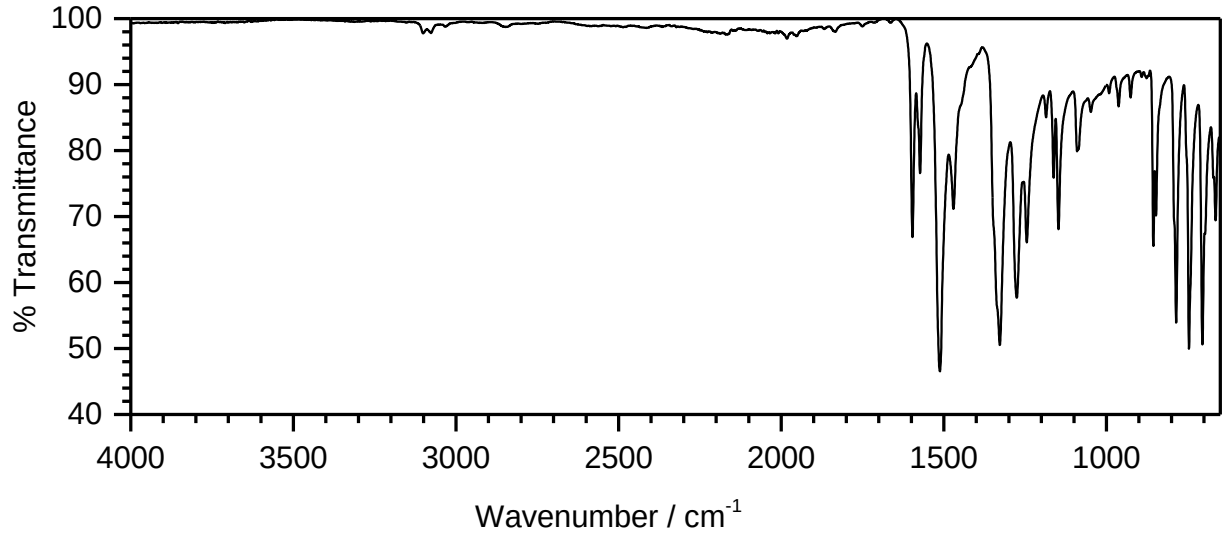

E12 Solid FT-IR spectra of Tris(2-nitrophenyl)amine

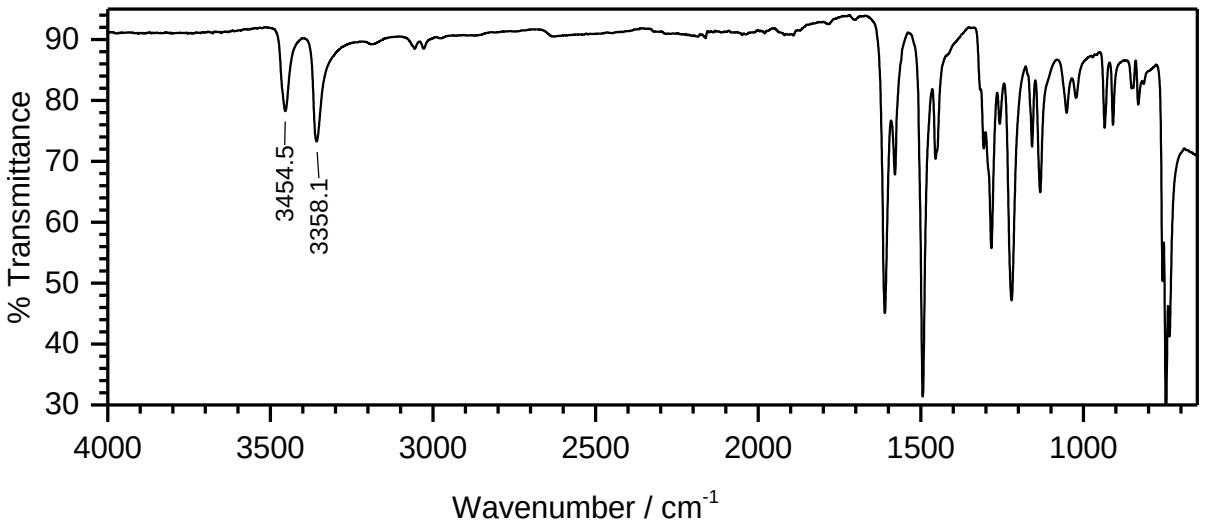

E13 Solid FT-IR spectra of Tris(2-aminophenyl)amine

7.3 NMR Spectra

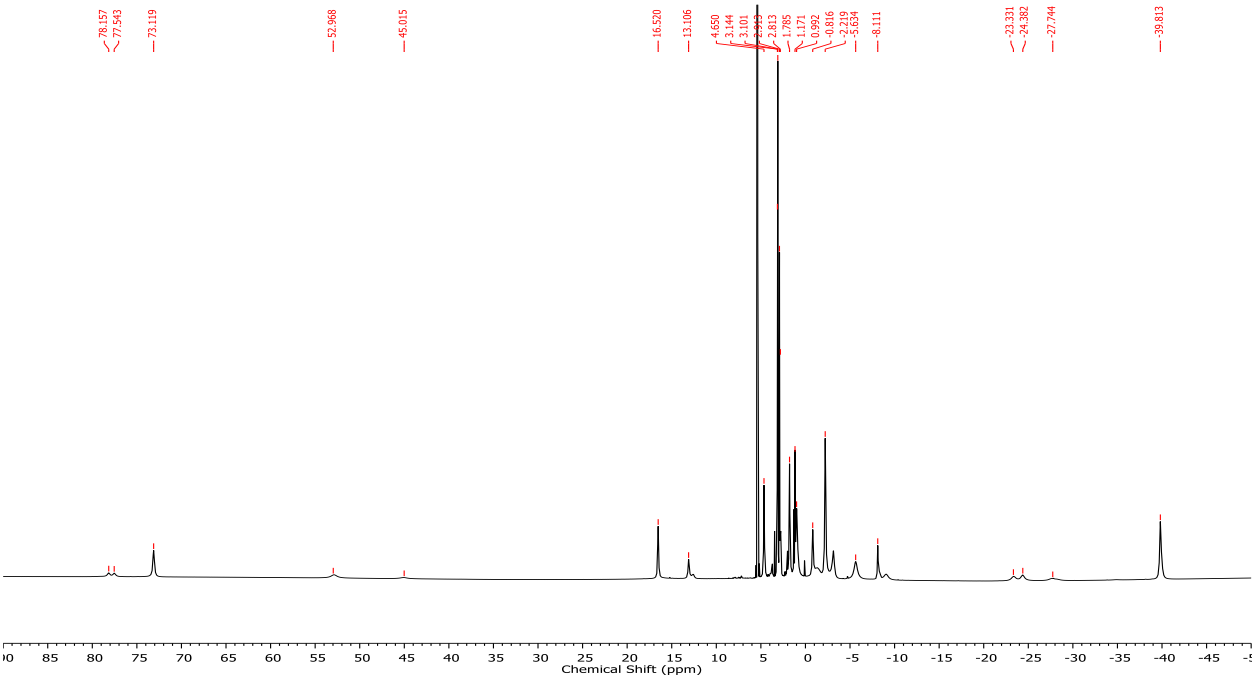

E14 ^{1}H NMR spectra of **3FeCl$_2$** in CD_2Cl_2 (500 MHz).

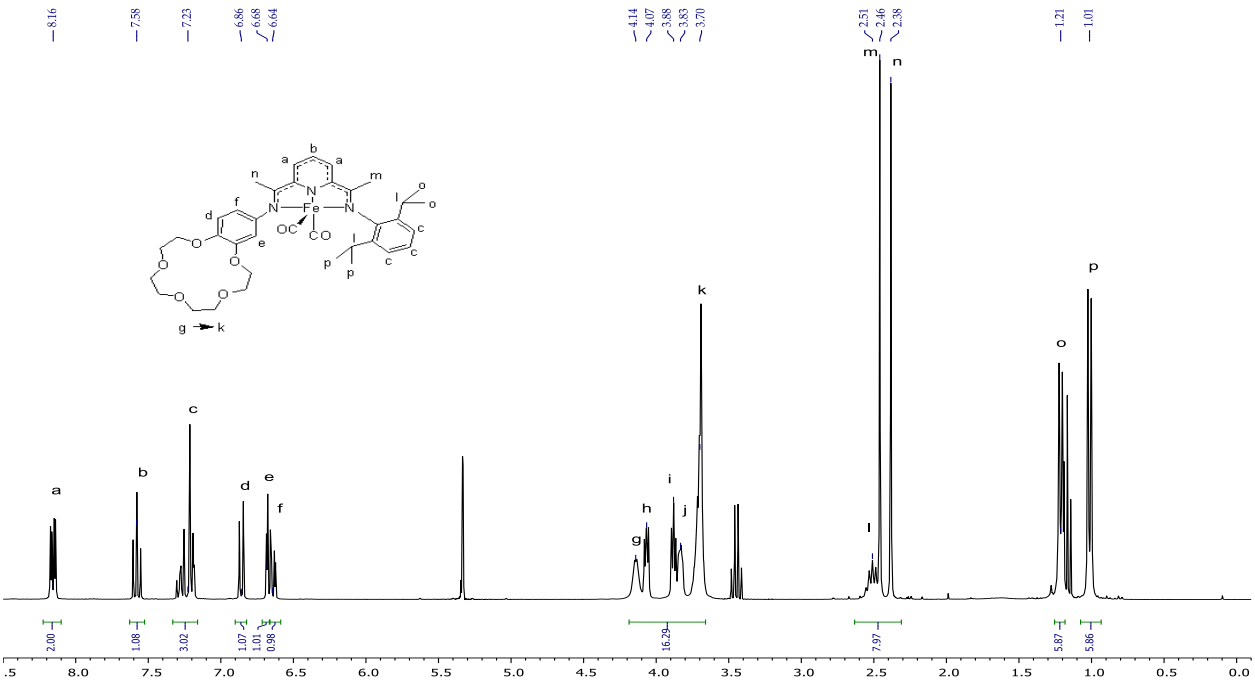

E15 ^{1}H NMR spectra of **3Fe(CO)$_2$** in CD_2Cl_2 (500 MHz).

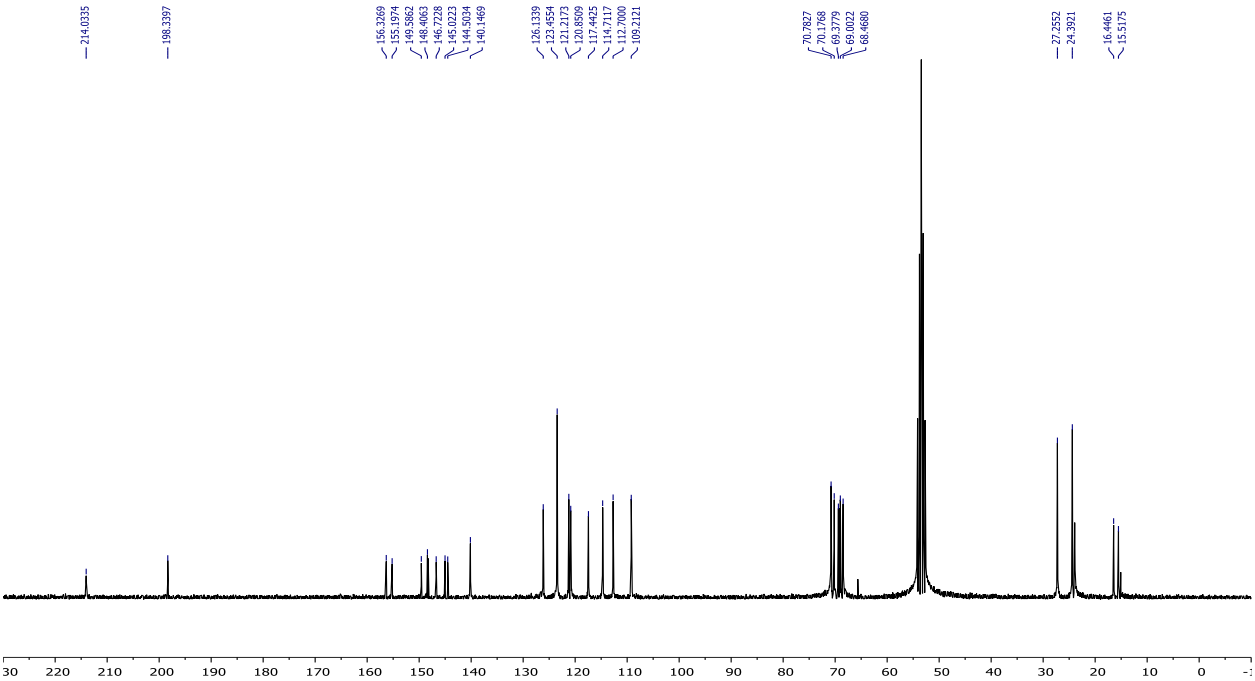

E16 ^{13}C NMR spectra of **$3Fe(CO)_2$** in CD_2Cl_2 (125 MHz).

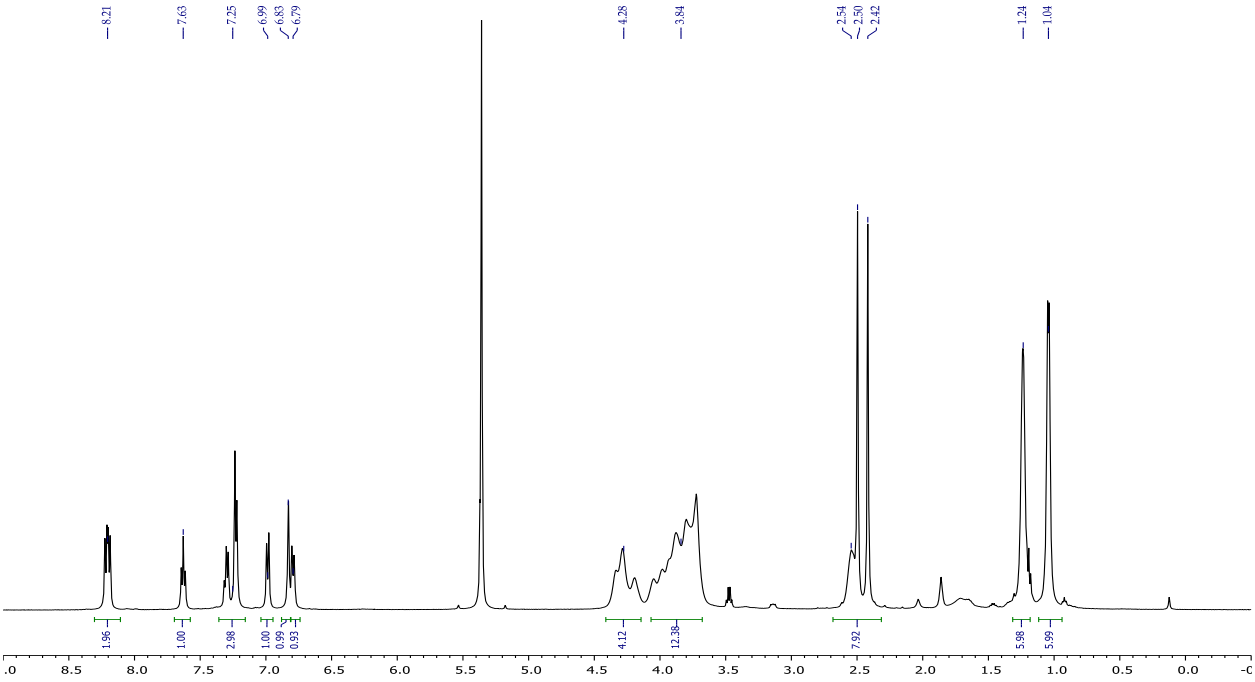

E17 ^{1}H NMR spectra of **$[3Fe(CO)_2Na][PF_6]$** in CD_2Cl_2 (500 MHz).

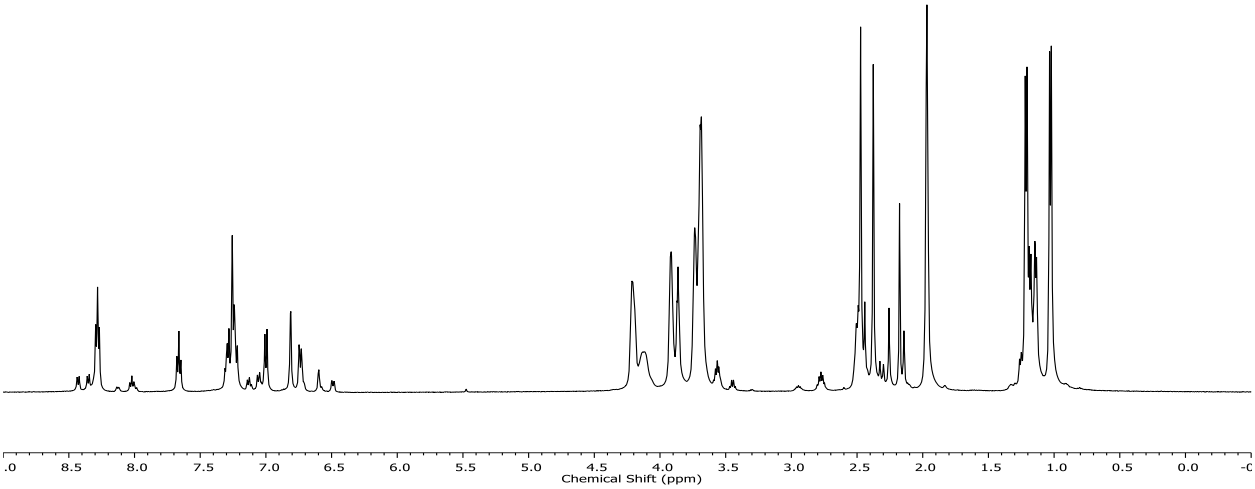

E18 ^{1}H NMR spectra of **[3Fe(CO)$_2$Na][NO$_2$]** in CD_2Cl_2 (500 MHz).

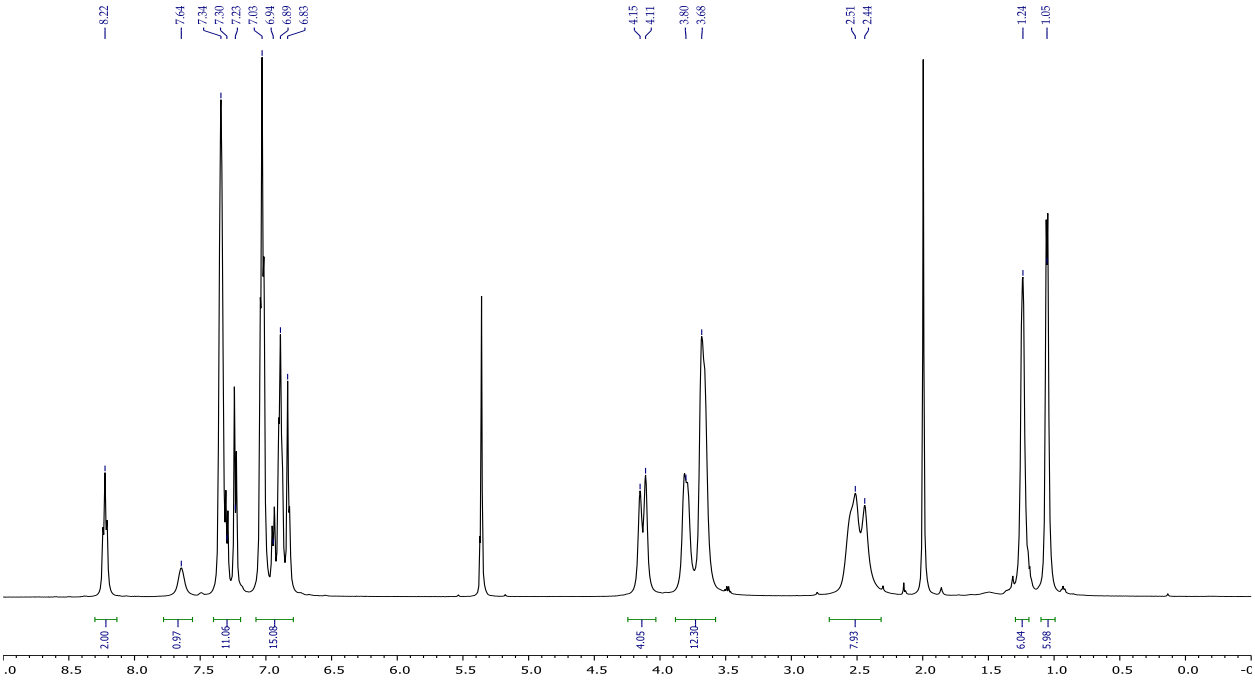

E19 ^{1}H NMR spectra of **[3Fe(CO)$_2$Na][BPh$_4$]** in CD_2Cl_2 (500 MHz).

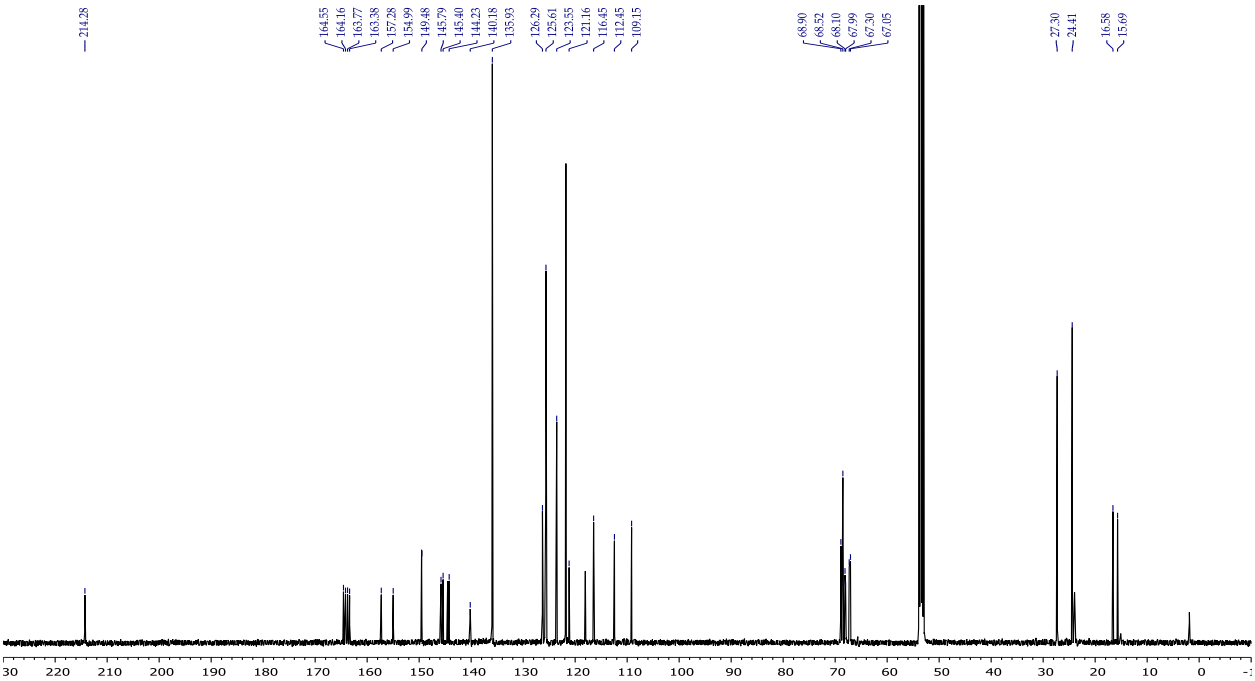

E20 ^{13}C NMR spectra of **[3Fe(CO)$_2$Na][BPh$_4$]** in CD_2Cl_2 (125 MHz).

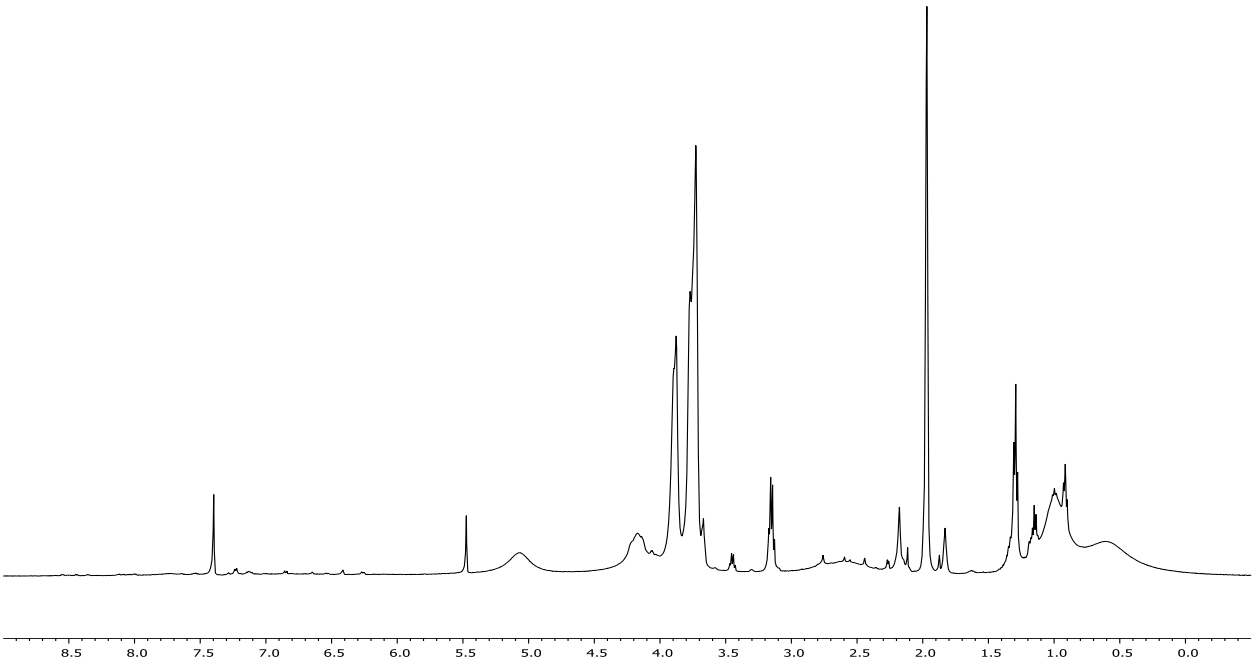

E21 ^{1}H NMR spectra of **[3Fe(NO)$_2$Na][PF$_6$]$_2$** in CD_2Cl_2 (500 MHz).

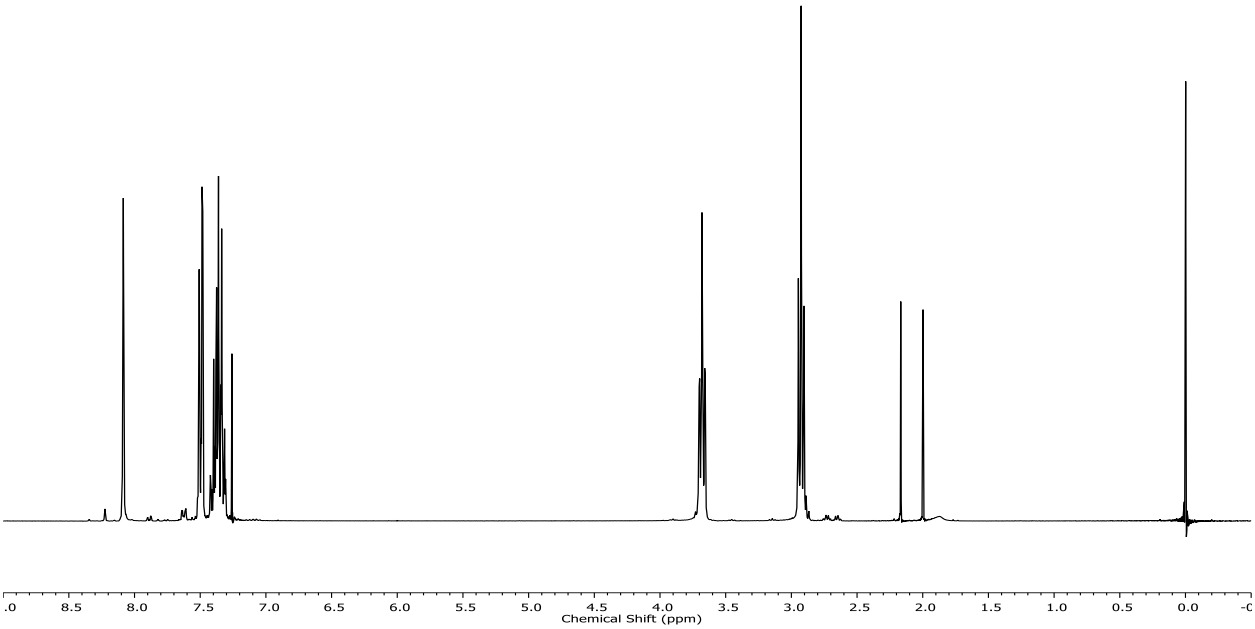

E22 ^{1}H NMR spectra of **4** in $CDCl_3$ (500 MHz).

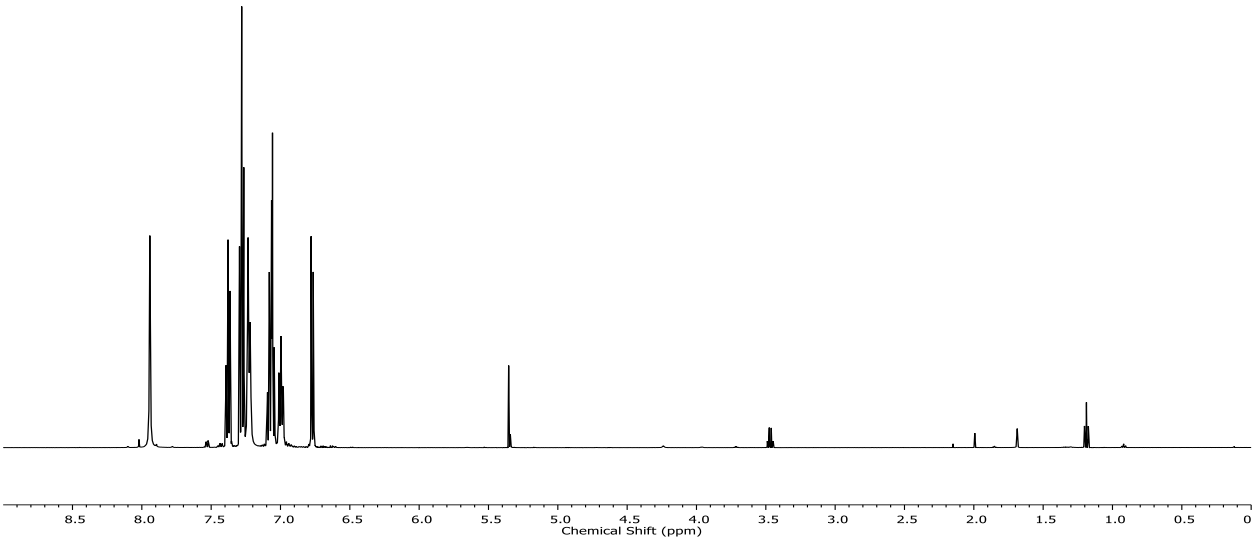

E23 ^{1}H NMR spectra of **5** in CD_2Cl_2 (500 MHz).

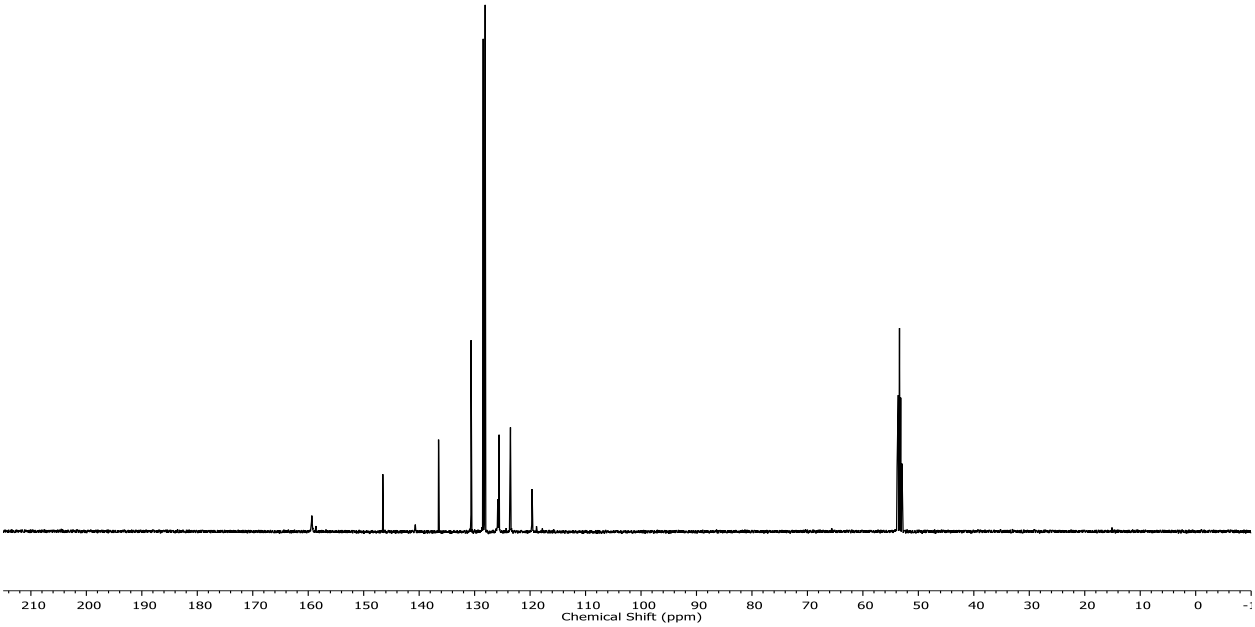

E24 ^{13}C NMR spectra of **5** in $CDCl_3$ (125 MHz).

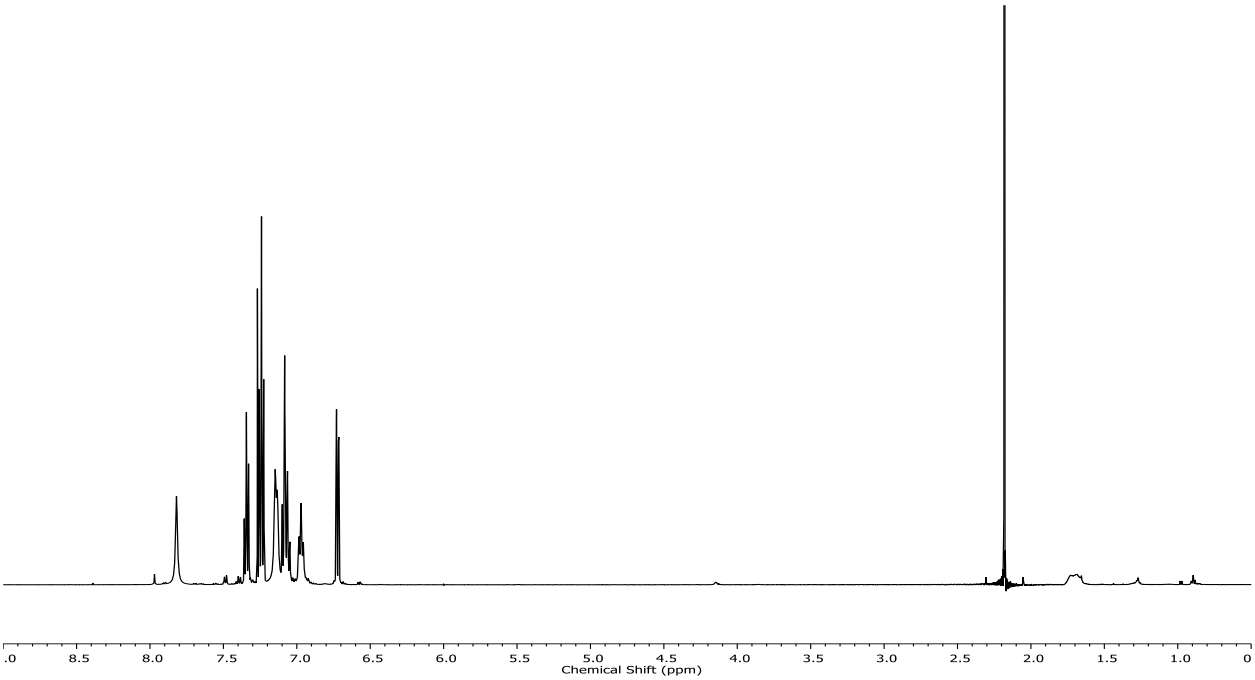

E25 ^{1}H NMR spectra of **5Zn(OTf)$_2$** in $CDCl_3$ (500 MHz).

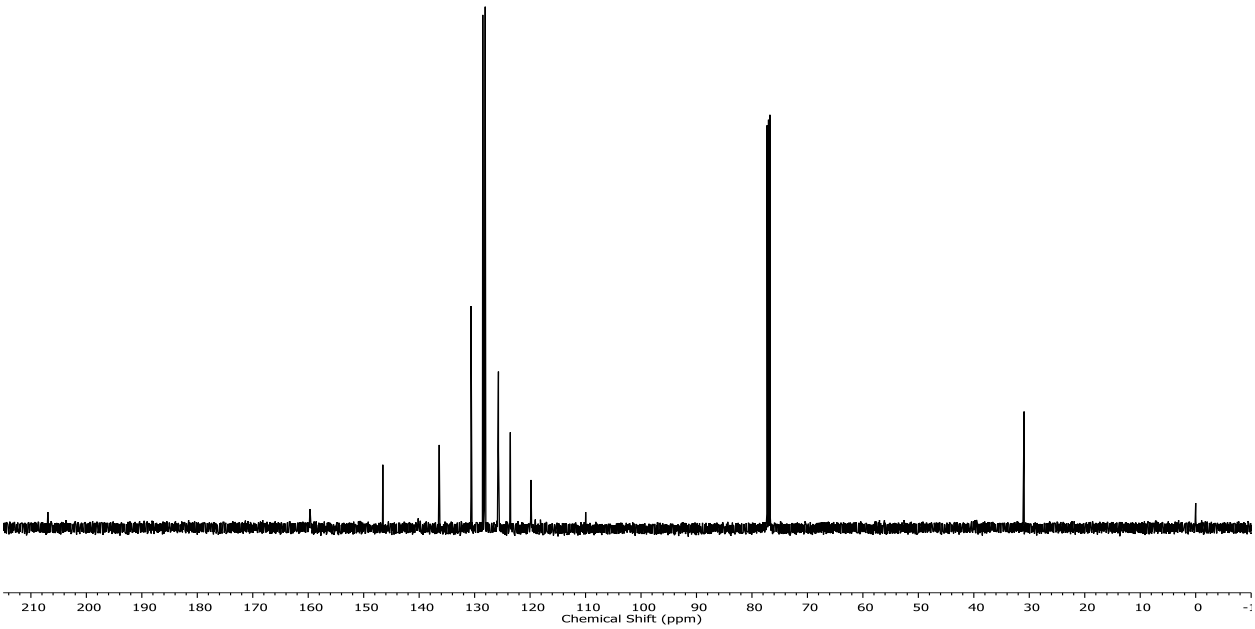

E26 ^{13}C NMR spectra of **5Zn(OTf)$_2$** in $CDCl_3$ (125 MHz).

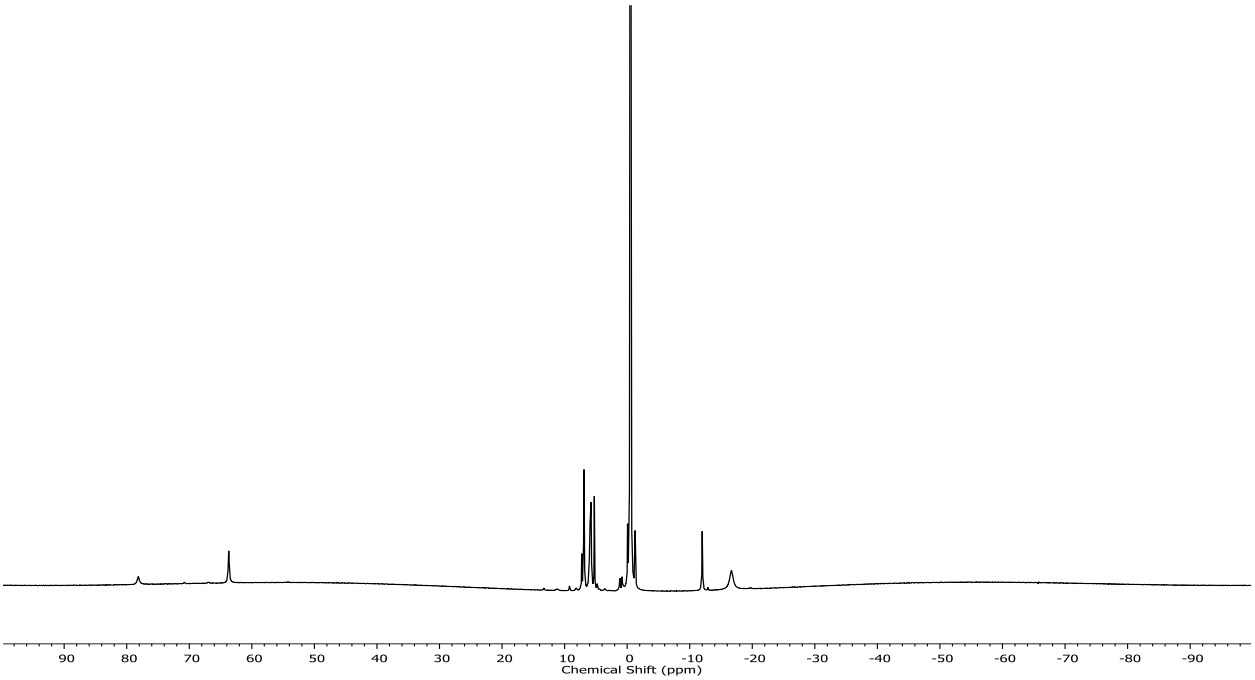

E27 ^{1}H NMR spectra of **8FeBr$_2$** in $CDCl_3$ (500 MHz).

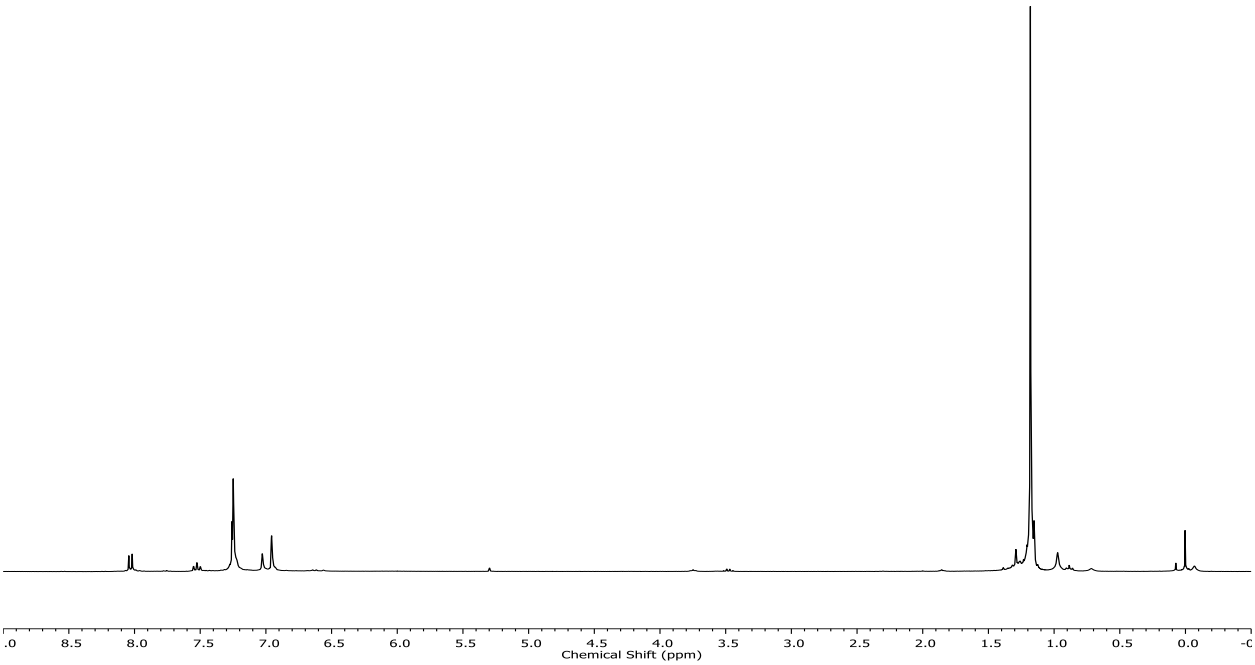

E28 ^{1}H NMR spectra of **8Fe(CO)$_2$** in $CDCl_3$ (500 MHz).

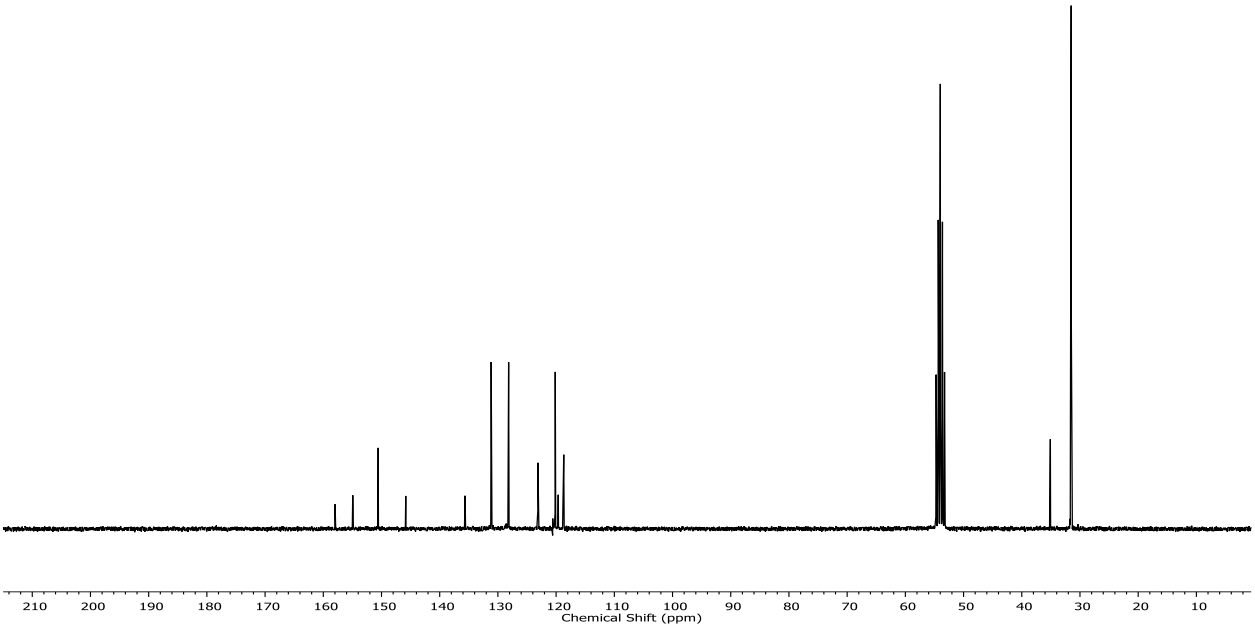

E29 ^{13}C NMR spectra of **8Fe(CO)$_2$** in CD_2Cl_2 (125 MHz).

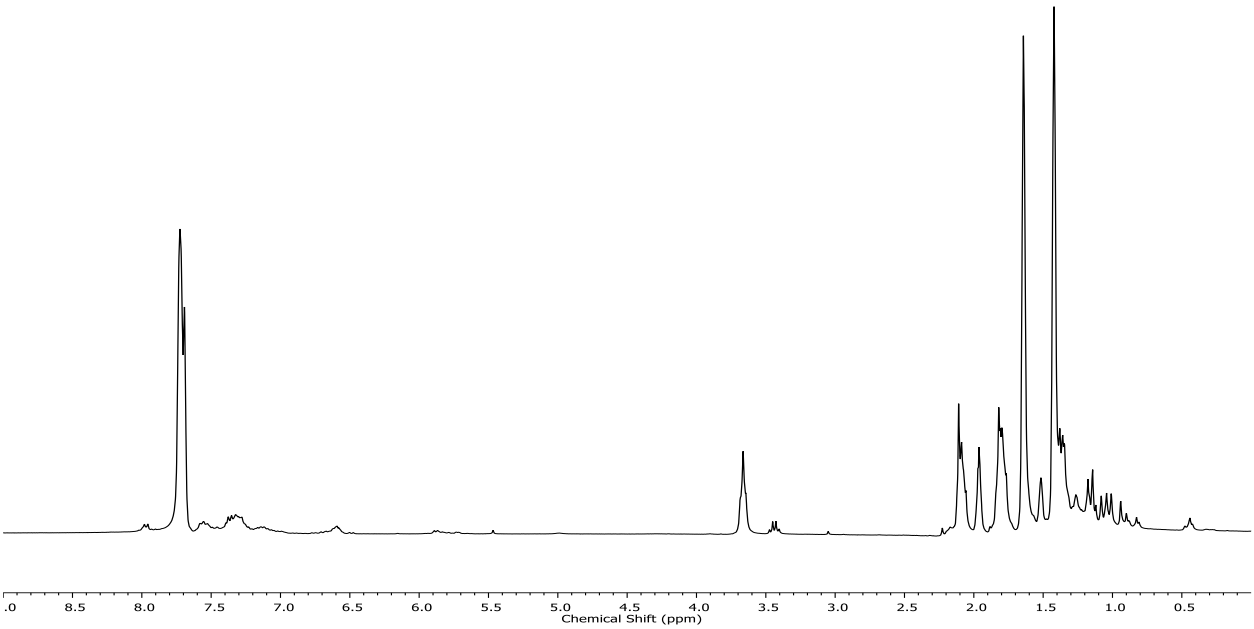

E30 ^{1}H NMR spectra of **9Fe(CO)$_2$** in CD_3CN (500 MHz).

7.4 ^{1}H NMR Salt Titration Binding Studies

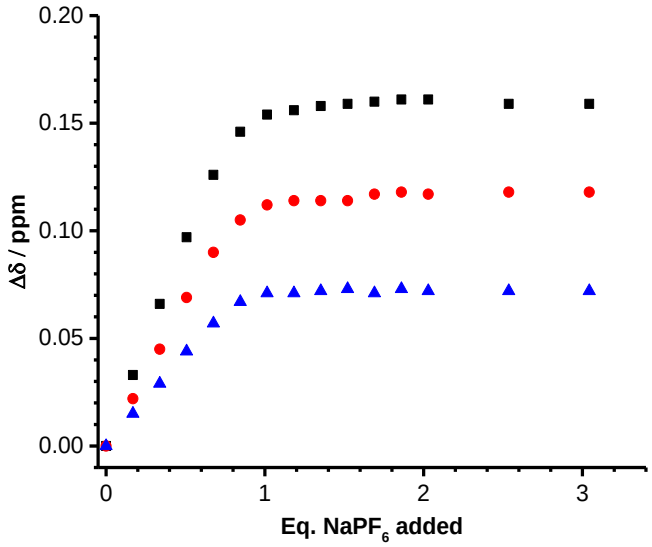

E31 ^{1}H NMR Titration of **3Fe(CO)$_2$** with $NaPF_6$. Binding isotherms.

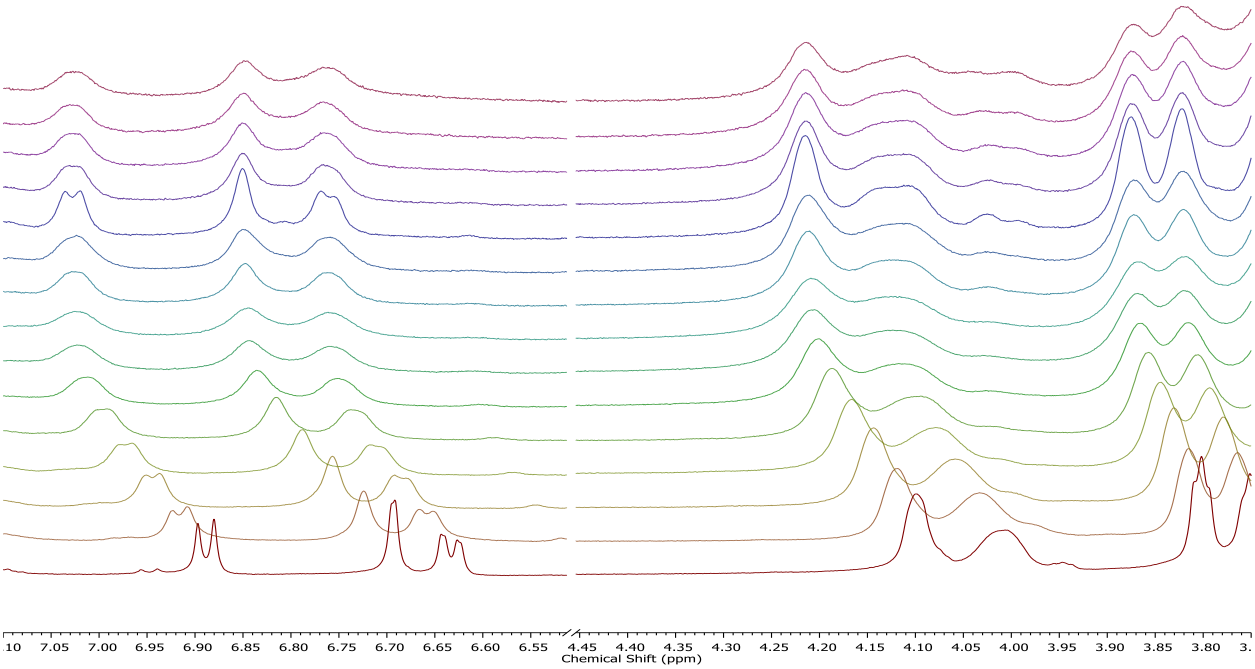

E32 ^{1}H NMR Titration of **3Fe(CO)$_2$** with $NaPF_6$. Waterfall plot of spectra. CD_3CN (500 MHz)

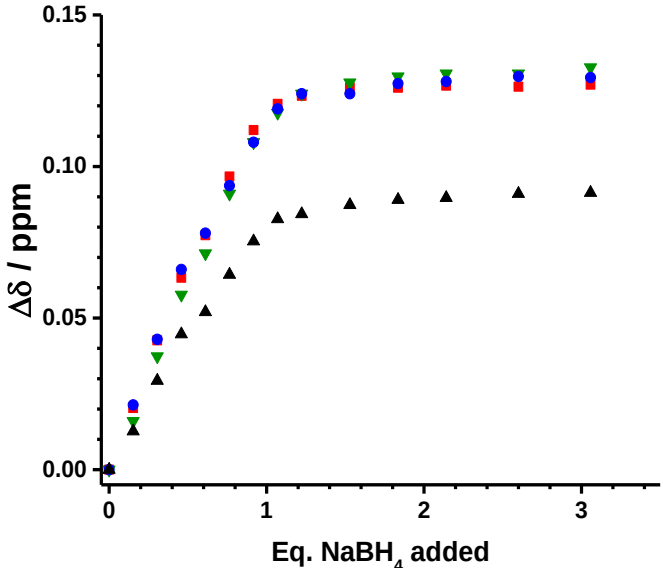

E33 ^{1}H NMR Titration of **3Fe(CO)$_2$** with $NaBH_4$. Binding isotherms.

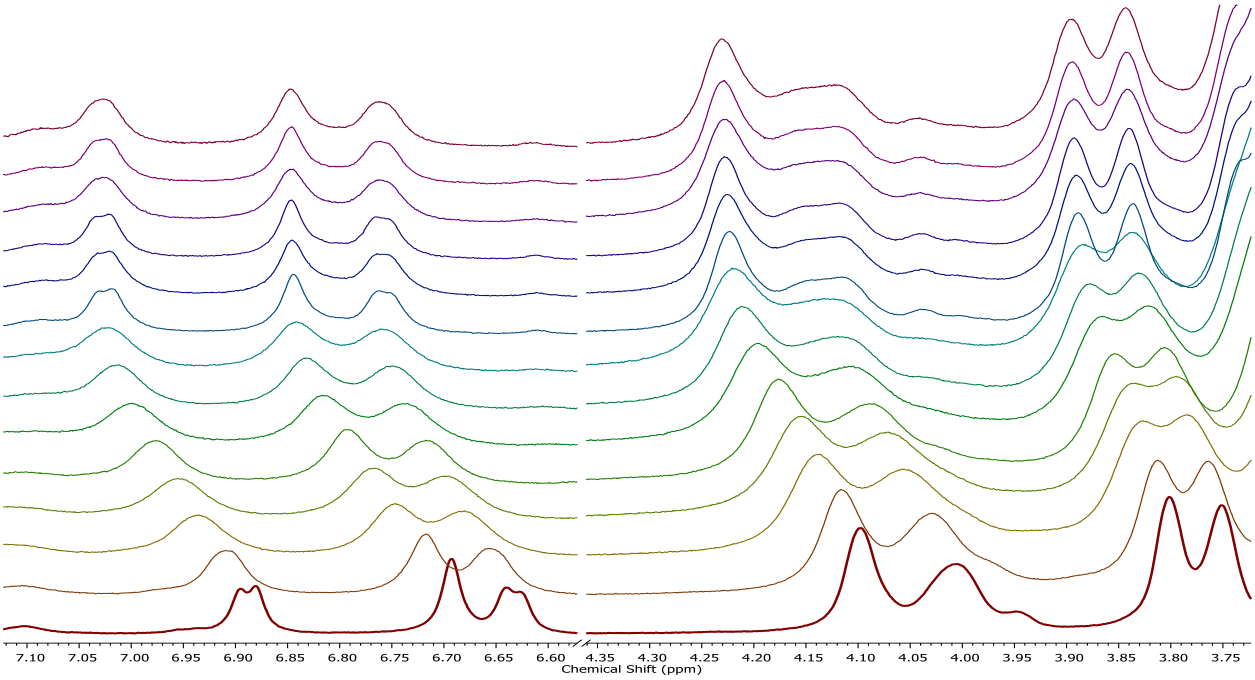

E34 ^{1}H NMR Titration of **3Fe(CO)$_2$** with $NaBH_4$. Waterfall plot of spectra. CD_3CN (500 MHz)

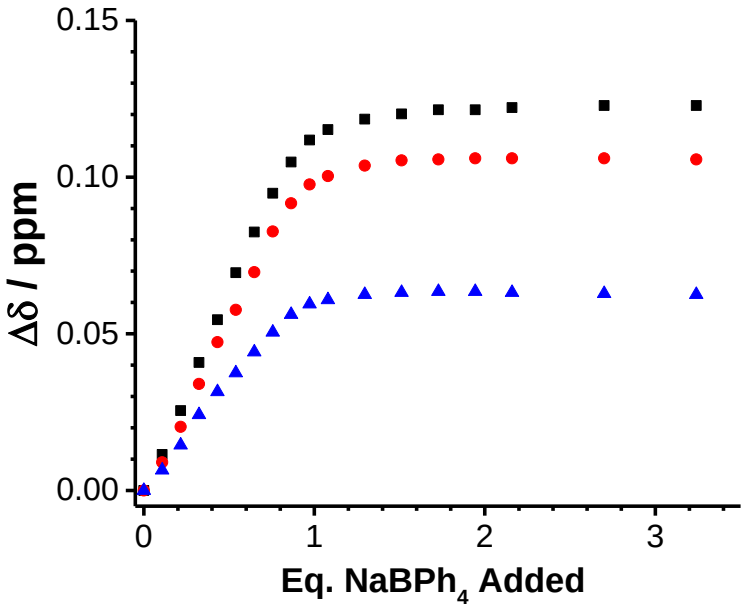

E35 ^{1}H NMR Titration of **3Fe(CO)$_2$** with NaBPh$_4$. Binding isotherms

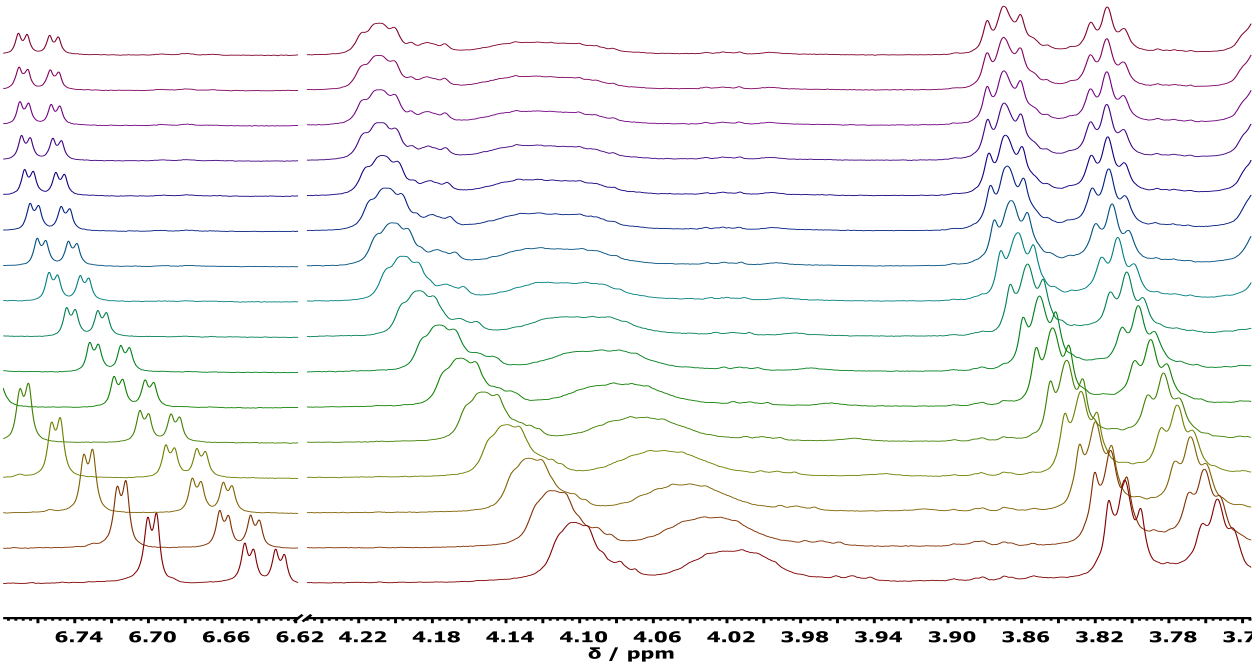

E36 ^{1}H NMR Titration of **3Fe(CO)$_2$** with NaBPh$_4$. Waterfall plot of spectra. CD_3CN (500 MHz)

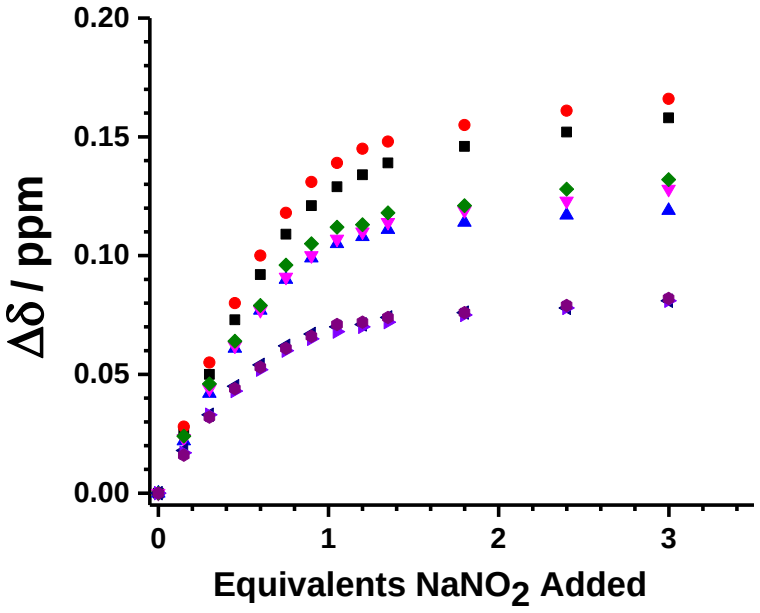

E37 ^{1}H NMR Titration of **3Fe(CO)$_2$** with $NaNO_2$. Binding isotherms.

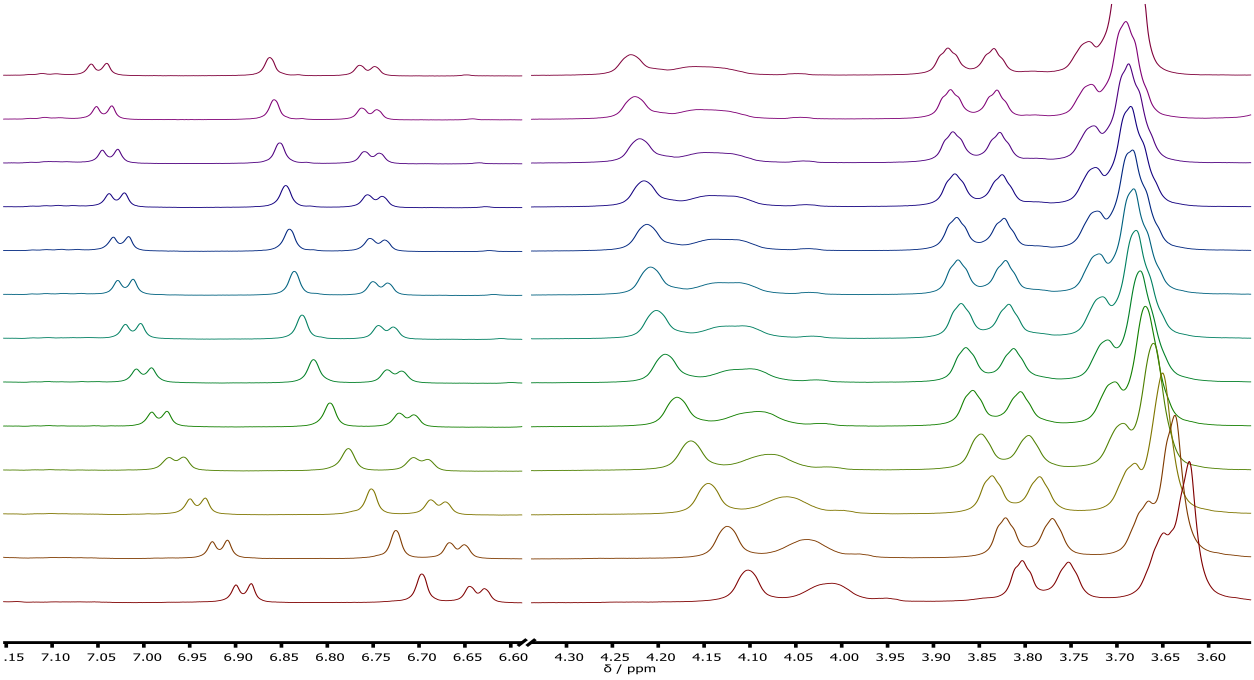

E38 ^{1}H NMR Titration of **3Fe(CO)$_2$** with $NaNO_2$. Waterfall plot of spectra. CD_3CN (500 MHz)

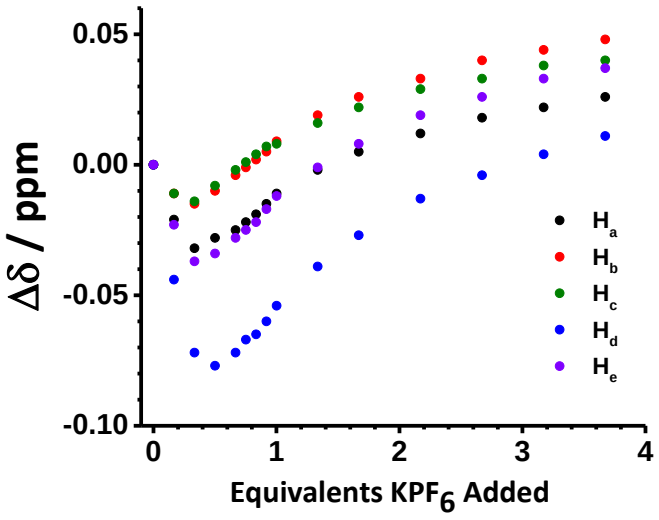

E39 ^{1}H NMR Titration of **3Fe(CO)$_2$** with KBPh$_4$. Binding isotherms.

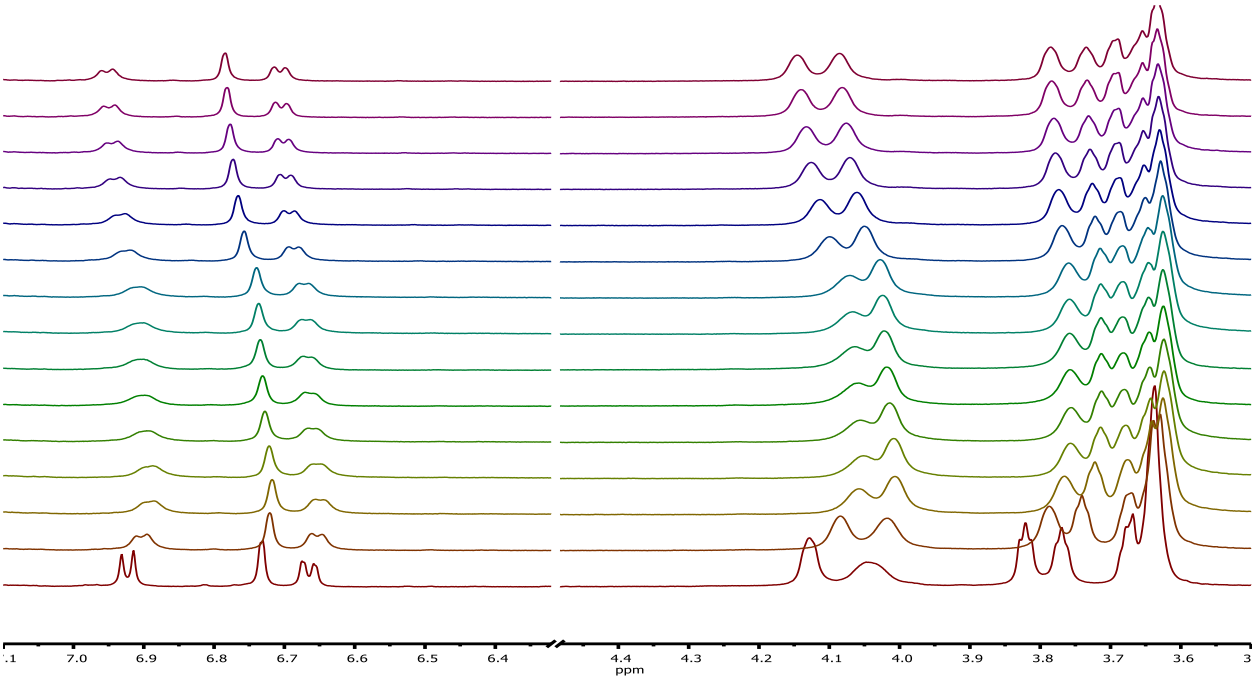

E40 ^{1}H NMR Titration of **3Fe(CO)$_2$** with KBPh$_4$. Waterfall plot of spectra. CD_3CN (500 MHz)

7.5 Mössbauer Spectra

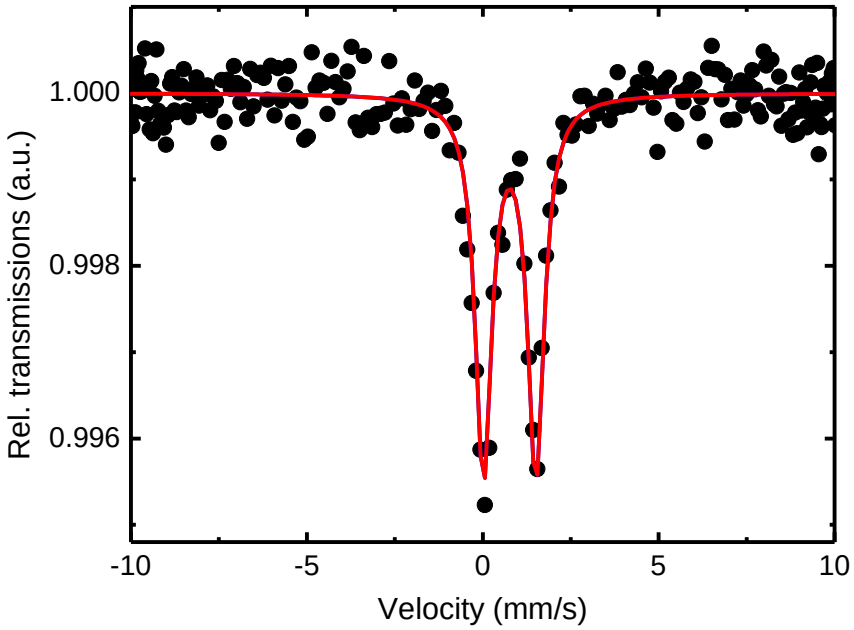

E41 Room Temperature Zero-field Mössbauer spectrum of **3FeCl$_2$**. Isomershift, δ = 0.87(1) mm/s, Quadrupole splitting, ΔE_Q = 1.49(2) mm/s, Line width, Γ = 0.56(3) mm/s.

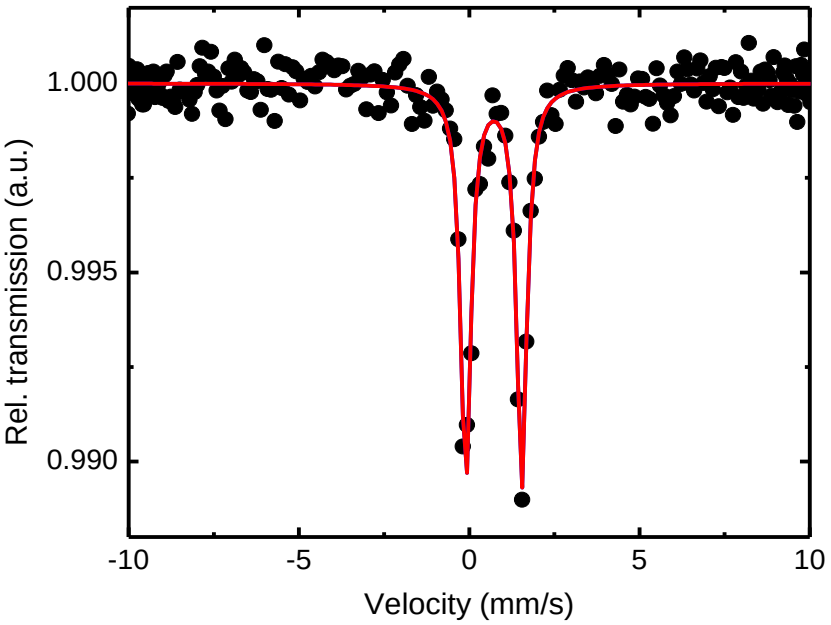

E42 Room Temperature Zero-field Mössbauer spectrum of **3FeBr$_2$**. Isomershift, δ = 0.821(5) mm/s, Quadrupole splitting, ΔE_Q = 1.644(7) mm/s, Line width, Γ = 0.36(1) mm/s.

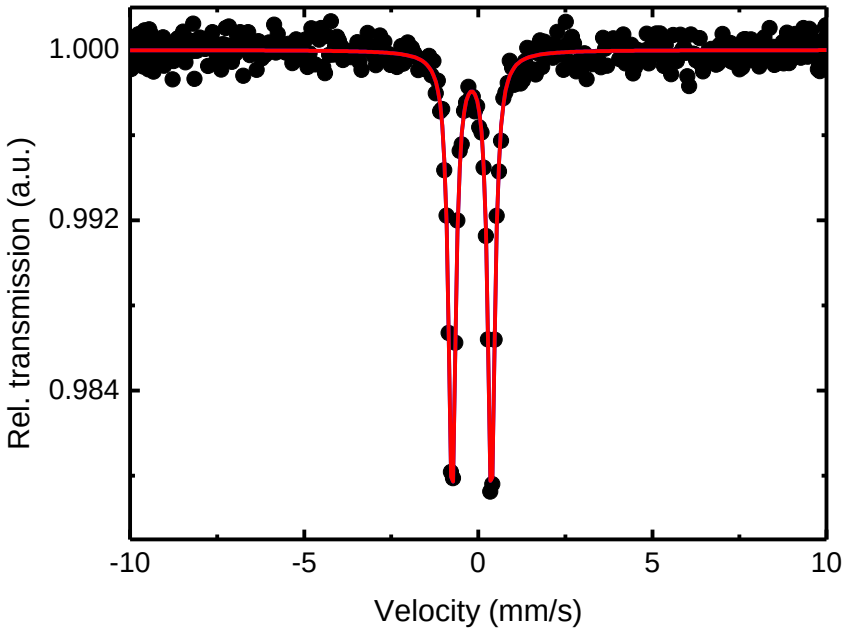

E43 Room Temperature Zero-field Mössbauer spectrum of **3Fe(CO)$_2$**. Isomershift, δ = - 0.088(3) mm/s, Quadrupole splitting, ΔE_Q = 1.126(4) mm/s, Line width, Γ = 0.246(5) mm/s.

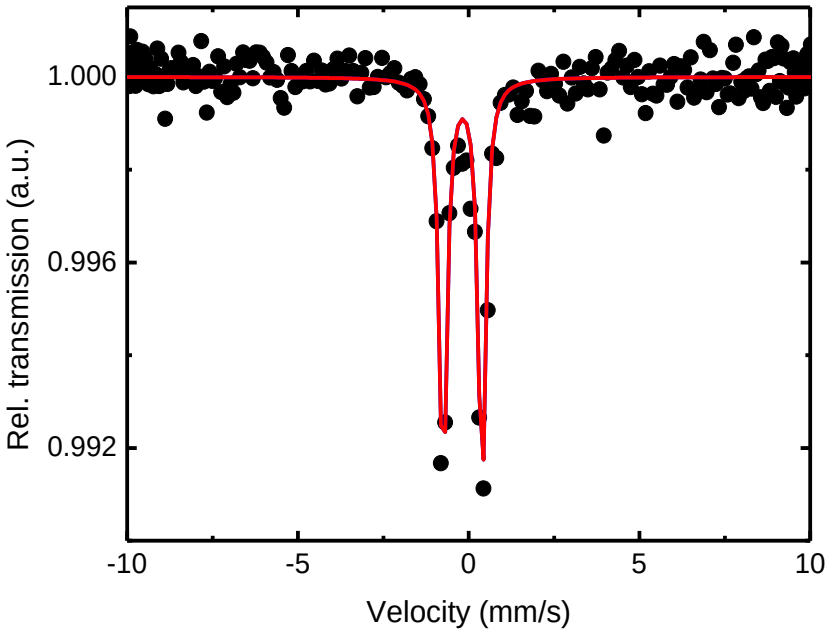

E44 Room Temperature Zero-field Mössbauer spectrum of **[3Fe(CO)$_2$Na][PF$_6$]**. Isomershift, δ = - 0.08(4) mm/s, Quadrupole splitting, ΔE_Q = 1.18(2) mm/s, Line width, Γ = 0.26(6) mm/s.

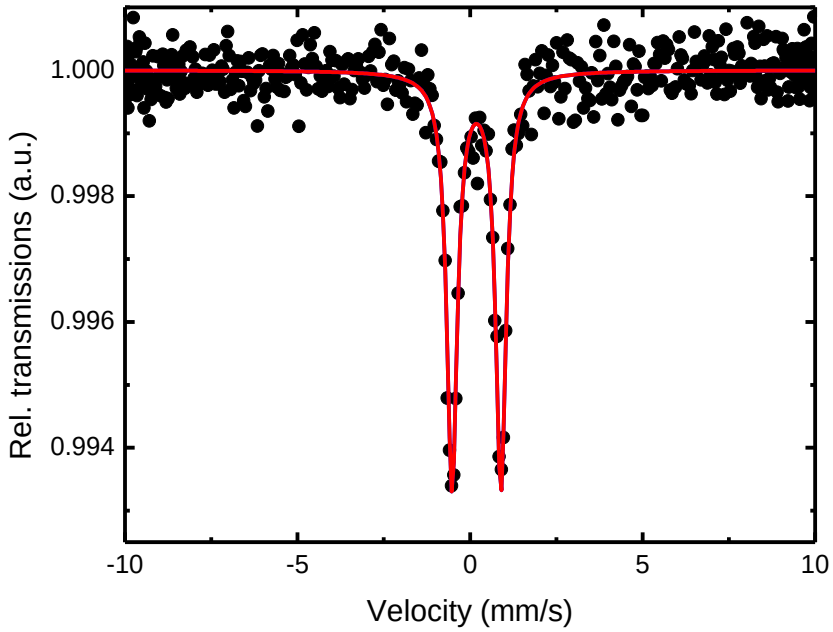

E45 Room Temperature Zero-field Mössbauer spectrum of **[3Fe(CO)$_2$Na][NO$_2$]**. Isomershift, δ = 0.286(5) mm/s, Quadrupole splitting, ΔE_Q = 1.471(9) mm/s, Line width, Γ = 0.37(1) mm/s.

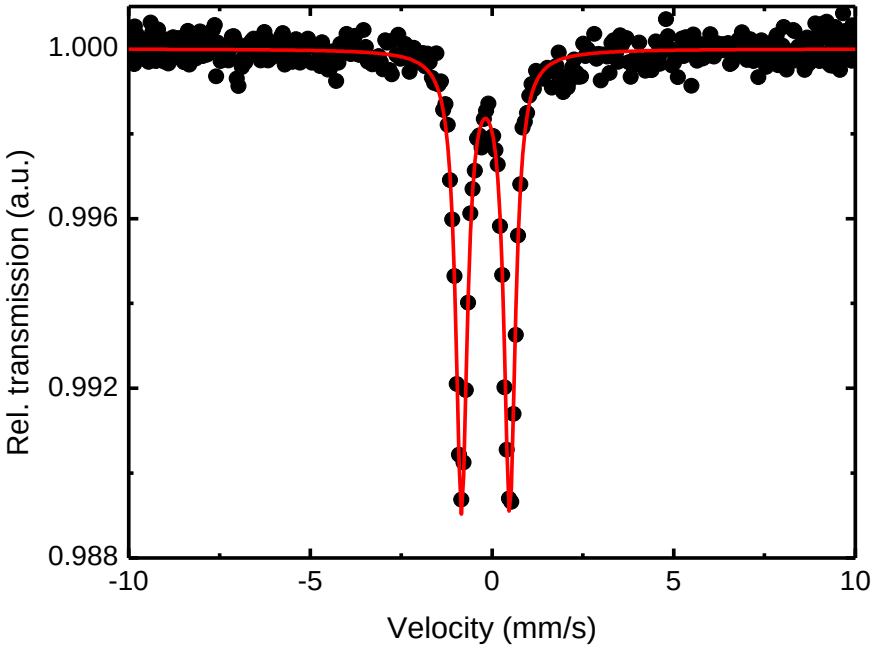

E46 Room Temperature Zero-field Mössbauer spectrum of **[3Fe(CO)$_2$Na][BPh$_4$].** Isomershift, δ = - 0.077(5) mm/s, Quadrupole splitting, ΔE_Q = 1.339(9) mm/s, Line width, Γ = 0.39(1) mm/s.

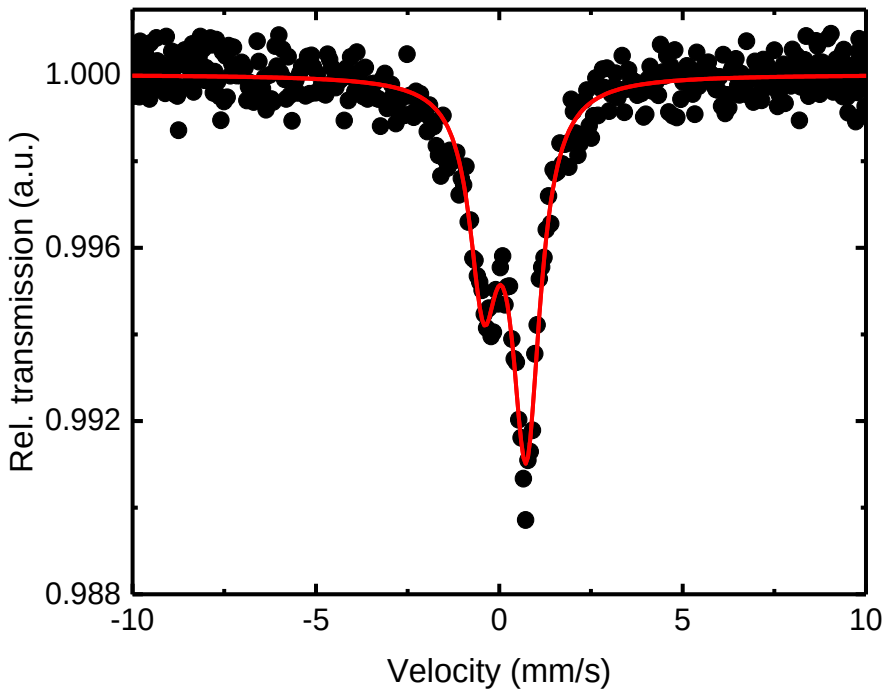

E47 Room Temperature Zero-field Mössbauer spectrum of **$[3Fe(NO)_2Na][PF_6]_2$**. Isomershift, δ = 0.25(1) mm/s, Quadrupole splitting, ΔE_Q = 1.16(2) mm/s, Line width, Γ = 0.92(3) mm/s.

7.6 Crystallographic Data

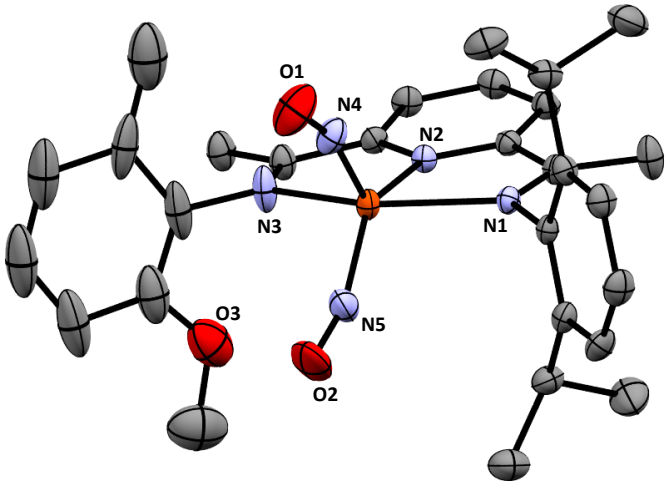

E48 Solid state structure at 30% probability of **$2Fe(NO)_2[PF_6]$**. The H atoms and PF_6^- counter ion have been omitted for clarity. Selected bond lengths (Å): Fe(1)-N(1), 2.220(3); Fe(1)-N(2), 2.078(3); Fe(1)-N(3), 2.160(4); Fe(1)-N(4), 1.691(4); Fe(1)-N(5), 1.693(5); C(2)-C(3), 1.484(5); and C(7)-C(8), 1.477(6). Selected bond angles (˚): N(1)Fe(1)N(3), 147.1(1); N(2)Fe(1)N(5), 131.5(2); Fe(1)N(4)O(1), 160.8(4); Fe(1)N(5)O(2), 160.1(5).

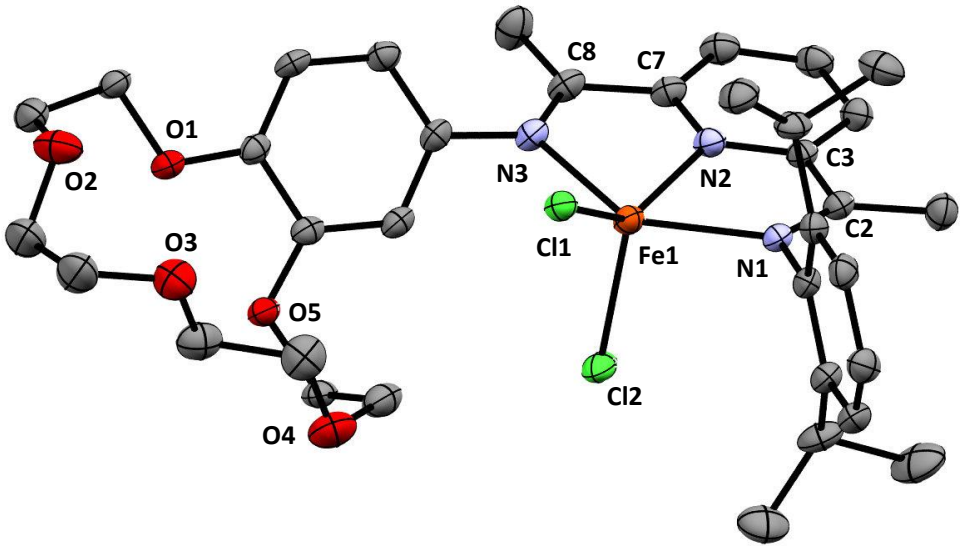

E49 Solid state structure at 30% probability of **$3FeCl_2$**. The H atoms have been omitted for clarity. Selected bond lengths (Å): Fe(1)-N(1), 2.252(4); Fe(1)-N(2), 2.116(4); Fe(1)-N(3), 2.233(3); C(2)-N(1), 1.288(7); C(8)-N(3), 1.295(7); C(2)-C(3), 1.480(7); and C(7)-C(8), 1.486(8). Selected bond angles (˚): Cl(1)Fe(1)N(2), 140.3(1); and N(1)Fe(1)N(3), 144.2(1).

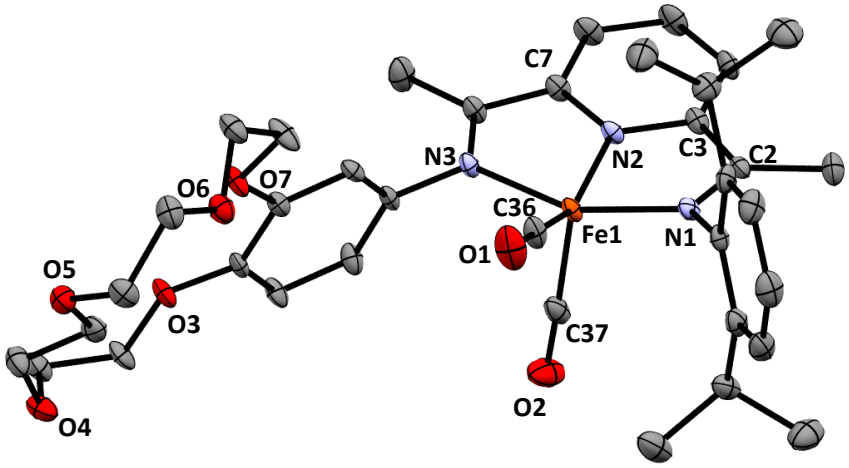

E50 Solid state structure at 30% probability of **3Fe(CO)$_2$**. The H atoms have been omitted for clarity. Selected bond lengths (Å): Fe(1)−C(36), 1.784(5); Fe(1)−C(37), 1.783(5); Fe(1)−N(1), 1.943(4); Fe(1)−N(2), 1.840(3); Fe(1)−N(3), 1.936(4); C(2)−N(1), 1.324(5); C(8)−N(3), 1.325(5); C(7)−C(8), 1.427(6); and C(2)−C(3), 1.436(7). Selected bond angles (°): N(2)Fe(1)C(36), 148.4(2); N(1)Fe(1)N(3), 156.3(2); and C(36)Fe(1)C(37), 97.7(2).

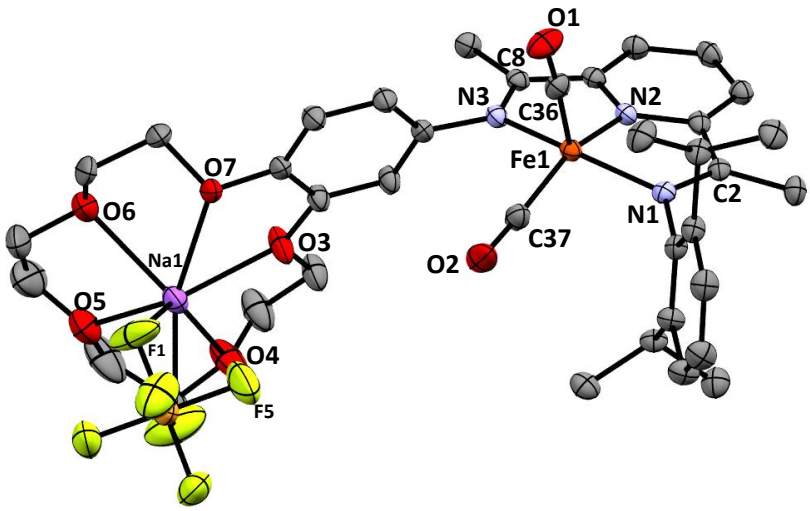

E51 Solid state structure at 30% probability of **[3Fe(CO)2Na][PF$_6$]**. The H atoms have been omitted for clarity. Selected bond lengths (Å): Fe(1)−C(36), 1.764(4); Fe(1)−C(37), 1.787(4); Fe(1)−N(1), 1.959(3); Fe(1)−N(2), 1.856(3); Fe(1)−N(3), 1.949(3); C(2)−N(1), 1.325(4); C(8)−N(3), and 1.333(4). Selected bond angles (°): C(36)Fe(1)C(37), 94.0(2); N(2)Fe(1)C(37), 153.9(2); and N(1)Fe(1)N(3), 153.6(1).

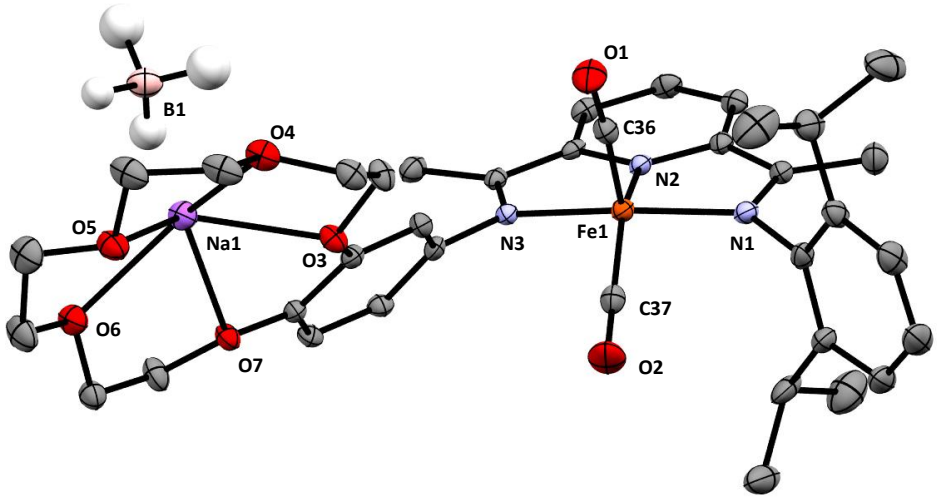

E52 Solid state structure at 30% probability of **[3Fe(CO)2Na][BH_4]**. The H atoms have been omitted for clarity. Selected bond lengths (Å): Fe(1)−C(36), 1.772(5); Fe(1)−C(37), 1.782(5); Fe(1)−N(1), 1.961(3); Fe(1)−N(2), 1.855(3); Fe(1)−N(3), 1.981(3); C(2)−N(1), 1.338(6); C(8)−N(3), and 1.337(5). Selected bond angles (°): C(36)Fe(1)C(37), 98.2(2); N(2)Fe(1)C(37), 150.1(2); and N(1)Fe(1)N(3), 155.7(1).

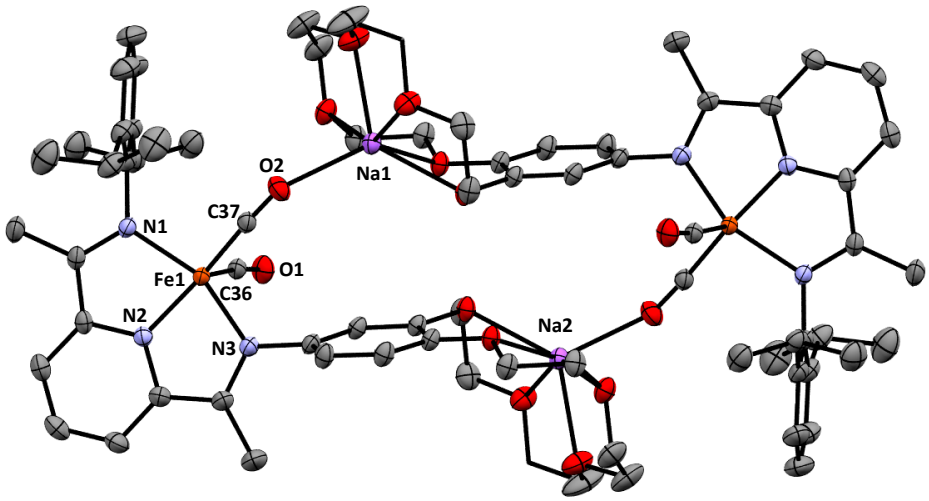

E53 Solid state structure at 30% probability of **[3Fe(CO)2Na][BPh_4]**. The H atoms have been omitted for clarity. Selected bond lengths (Å): Fe(1)−C(36), 1.776(3); Fe(1)−C(37), 1.770(2); Fe(1)−N(1), 1.966(2); Fe(1)−N(2), 1.847(2); Fe(1)−N(3), 1.945(2); C(2)−N(1), 1.323(2); C(8)−N(3), and 1.324(2). Selected bond angles (°): C(36)Fe(1)C(37), 97.1(1); N(2)Fe(1)C(37), 152.35(9); and N(1)Fe(1)N(3), 155.42(7).

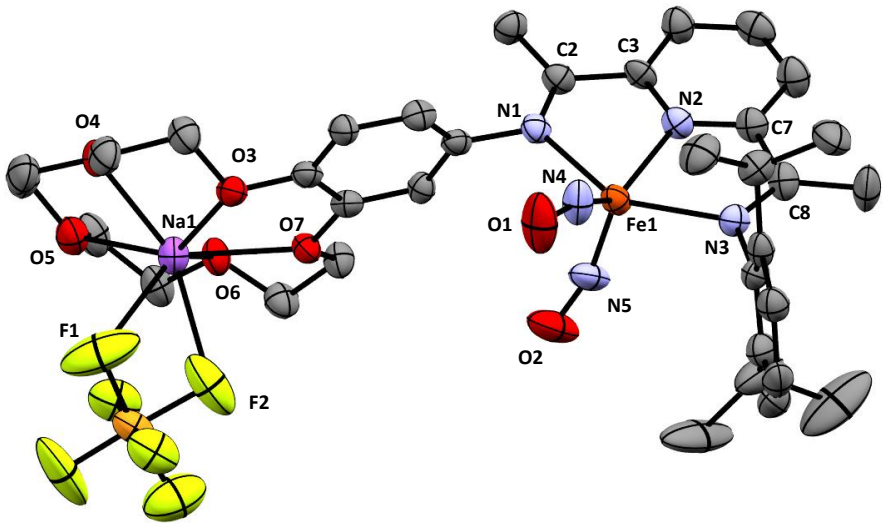

E54 Solid state structure at 30% probability of **[3Fe(NO)$_2$Na][PF$_6$]**. The H atoms and one PF_6^- have been omitted for clarity. Selected bond lengths (Å):. Fe(1)−N(1), 2.113(8); Fe(1)−N(2), 2.071(7); Fe(1)−N(3), 2.202(8); Fe(1)−N(4), 1.692(9); Fe(1)−N(5), 1.684(9); N(1)−C(2), 1.29(1); N(3)−C(8), 1.29(1); C(2)-C(3), 1.47(1); and C(7)-C(8), 1.49(1). Selected bond angles (°): N(4)Fe(1)N(5), 109.3(4); N(2)Fe(1)N(4), 135.6(4); N(1)Fe(1)N(3), 147.6(3); Fe(1)N(4)O(1), 157.9(9); and Fe(1)N(5)O(2), 161.3(8).

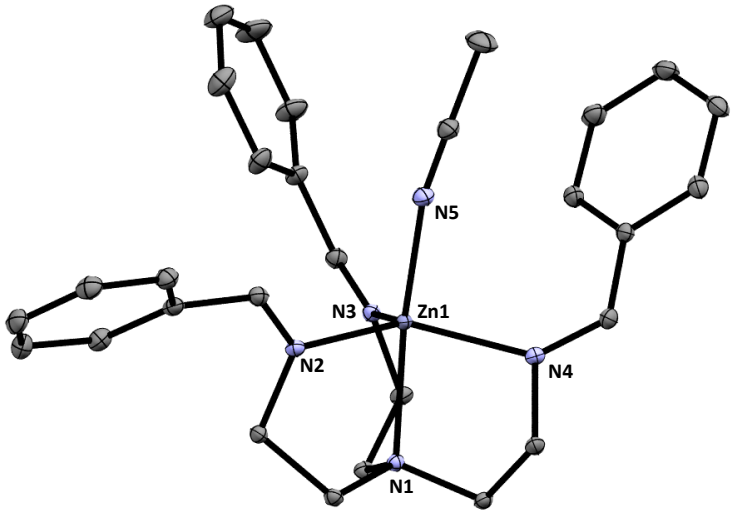

E55 Solid state structure at 30% probability of **4Zn(NCMe)[OTf]$_2$**. The H atoms and both triflates have been omitted for clarity. Selected bond lengths (Å): Zn(1)-N(1), 2.2058; Zn(1)-N(2), 2.0667; Zn(1)-N(3), 2.0710; Zn(1)-N(4), 2.0996; and Zn(1)-N(5), 2.0810. Selected bond angles (˚): N(1)Zn(1)N(5), 168.80; and N(2)Zn(1)N(4), 131.97.

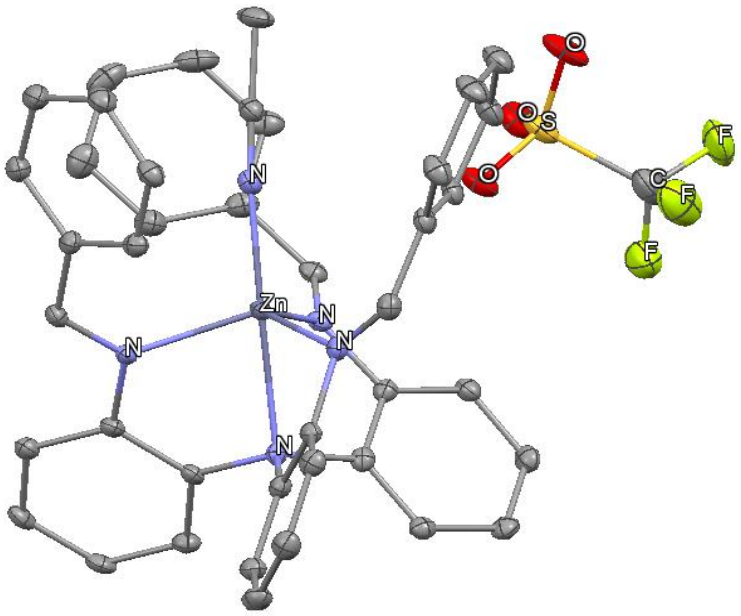

E56 Solid state structure at 30% probability of **5Zn(NCMe)[OTf]$_2$**. The H atoms and second triflate have been omitted for clarity.

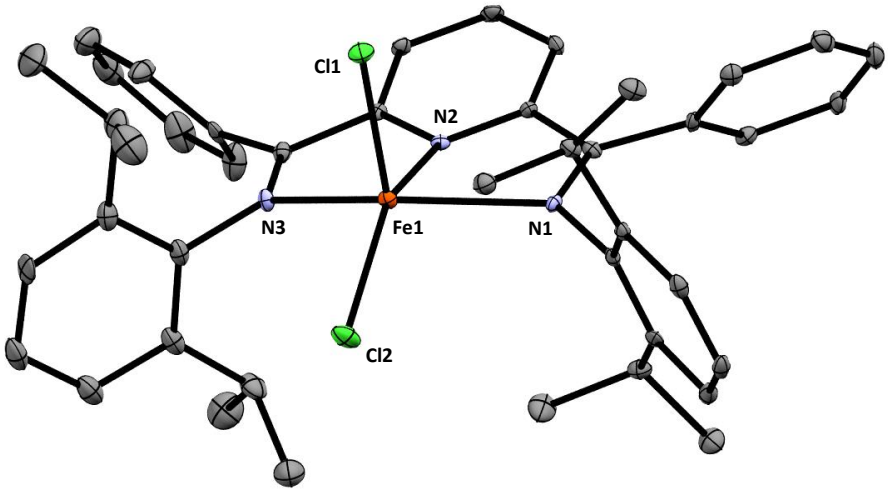

E57 Solid state structure at 30% probability of **7FeCl$_2$**. The H atoms have been omitted for clarity. Selected bond lengths (Å): Fe(1)-Cl(1), 2.3502(8); Fe(1)-Cl(2), 2.3100(9); Fe(1)-N(1), 2.380(3); Fe(1)-N(2), 2.184(2); Fe(1)-N(3), 2.345(3). Selected bond angles (˚): N(1)Fe(1)N(3), 138.22(9); Cl(2)Fe(1)N(2), 143.31(6).

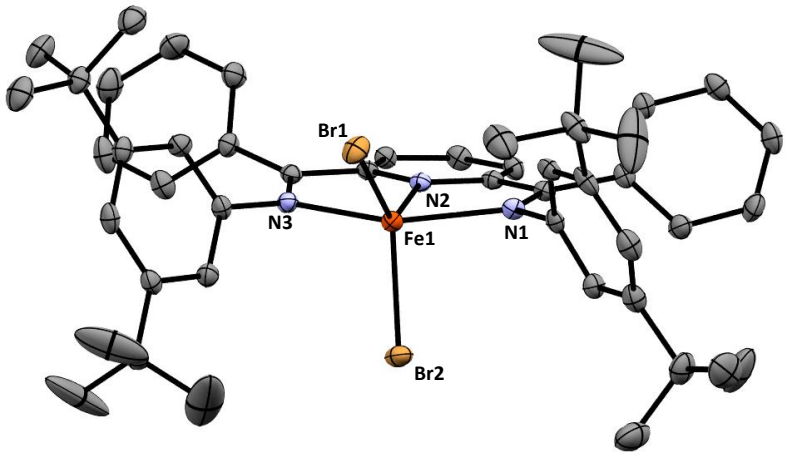

E58 Solid state structure at 30% probability of **8FeBr$_2$**. The H atoms have been omitted for clarity. Selected bond lengths (Å): Fe(1)-Br(1), 2.4405(6); Fe(1)-Br(2), 2.4526(7) ; Fe(1)-N(1), 2.211(3); Fe(1)-N(2), 2.082(3); Fe(1)-N(3), 2.205(3); N(1)-C(1), 1.298(4); N(3)-C(7), 1.295(5); C(1)-C(2), 1.495(5); and C(6)-C(7), 1.496(4). Selected bond angles (˚): Br(1)Fe(1)Br(2), 126.17(2); N(1)Fe(1)N(3), 147.9(1); and Br(1)Fe(1)N(2), 128.01(8).

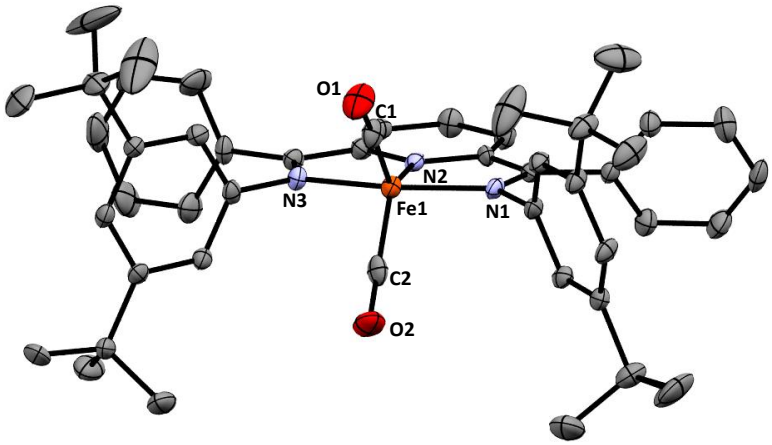

E59 Solid state structure at 30% probability of **8Fe(CO)$_2$**. The H atoms have been omitted for clarity. Selected bond lengths (Å): Fe(1)-C(1), 1.795(8); Fe(1)-C(2), 1.796(8); Fe(1)-N(1), 1.948(6); Fe(1)-N(2), 1.851(5); Fe(1)-N(3), 1.944(5); N(1)-C(3), 1.350(9); N(3)-C(9), 1.34(1); C(3)-C(4), 1.42(1); and C(8)-C(9), 1.43(1). Selected bond angles (˚): C(1)Fe(1)C(2), 94.4(3); N(1)Fe(1)N(3), 158.7(2); and N(2)Fe(1)C(2), 134.2(3).

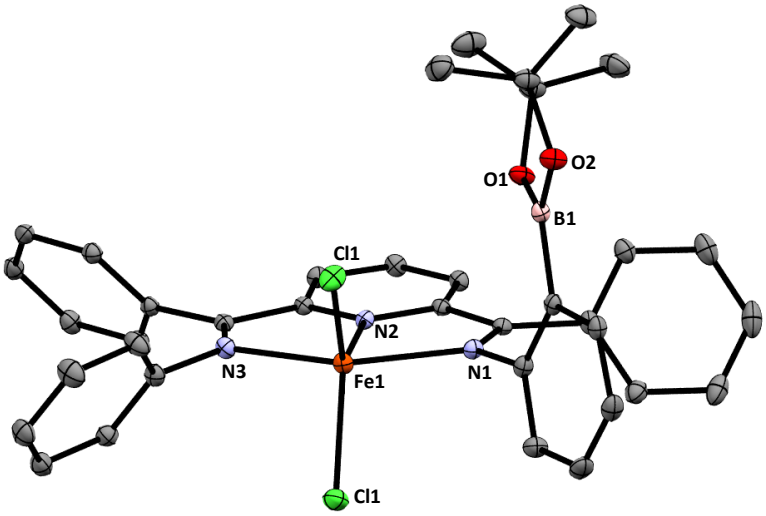

E60 Solid state structure at 30% probability of **9FeCl$_2$**. The H atoms have been omitted for clarity. Selected bond lengths (Å): Fe(1)-Cl(1), 2.2761(6); Fe(1)-Cl(2), 2.2822(6); Fe(1)-N(1), 2.177(2); Fe(1)-N(2), 2.045(2); Fe(1)-N(3), 2.176(2); N(1)-C(1), 1.287(3); N(3)-C(7), 1.297(2); C(1)-C(2), 1.481(2); and C(6)-C(7), 1.476(3). Selected bond angles (˚): Cl(1)Fe(1)Cl(2), 122.96(2); and N(1)Fe(1)N(3), 148.91(6).

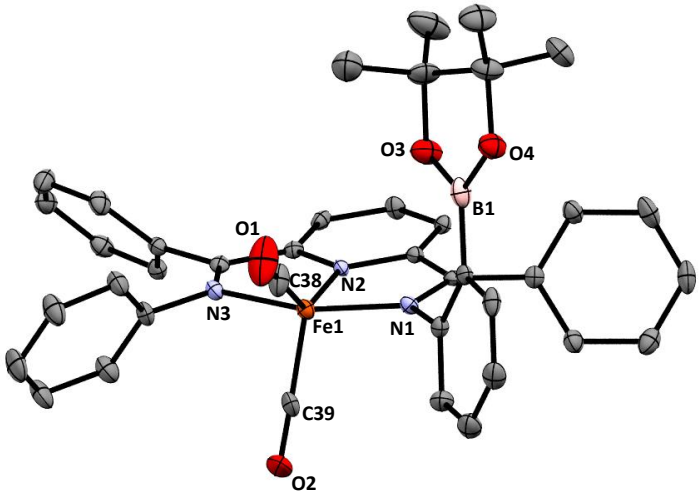

E61 Solid state structure at 30% probability of **9Fe(CO)$_2$**. The H atoms have been omitted for clarity. Selected bond lengths (Å): Fe(1)-C(38), 1.766(3); Fe(1)-C(39), 1.771(5); Fe(1)-N(1), 1.942(3); Fe(1)-N(2), 1.838(3); Fe(1)-N(3), 1.950(2); N(1)-C(1), 1.326(5); N(3)-C(7), 1.331(4); C(1)-C(2), 1.427(4); and C(6)-C(7), 1.431(6). Selected bond angles (˚): C(38)Fe(1)C(39), 97.6(2); N(1)Fe(1)N(3), 159.0(1); and N(2)Fe(1)C(38), 137.6(2).

References

(1) Meyer, F.; Tolman, W. B. Forums on Small-Molecule Activation: From Biological Principles to Energy Applications. *Inorg. Chem.* **2015**, *54*, 5039–5039.

(2) Nielsen, A. *Ammonia: Catalysis and Manufacture*; Springer Berlin Heidelberg: Berlin, Heidelberg, 1995.

(3) Ely, J. C.; Neal, C. R.; Kulpa, C. F.; Schneegurt, M. A.; Seidler, J. A.; Jain, J. C. Implications of Platinum-Group Element Accumulation along U.S. Roads from Catalytic-Converter Attrition. *Environ. Sci. Technol.* **2001**, *35*, 3816–3822.

(4) Mizuno, N.; Misono, M. Heterogeneous Catalysis. *Chem. Rev.* **1998**, *98*, 199–217.

(5) Beller, M. Homogeneous Catalysis for Fine Chemical Synthesiss — New Trends and Perspectives —. In *Studies in Surface Science and Catalysis*; Elsevier, 1997; Vol. 108, pp 1–16.

(6) Zastrow, M. L.; Pecoraro, V. L. Designing Functional Metalloproteins: From Structural to Catalytic Metal Sites. *Coord. Chem. Rev.* **2013**, *257*, 2565–2588.

(7) Burgess, B. K.; Lowe, D. J. Mechanism of Molybdenum Nitrogenase. *Chem. Rev.* **1996**, *96*, 2983–3012.

(8) Kandemir, T.; Schuster, M. E.; Senyshyn, A.; Behrens, M.; Schlögl, R. The Haber–Bosch Process Revisited: On the Real Structure and Stability of “Ammonia Iron” under Working Conditions. *Agnew. Chem., Int. Ed.* **2013**, *52*, 12723–12726.

(9) Smith, B. Nitrogenase Reveals Its Inner Secrets. *Science* **2002**, *297*, 1654–1655.

(10) Wood, S.; Cowie, A. *A Review of Greenhouse Gas Emission Factors for Fertiliser Production.*; 2004; p 20.

(11) Holt, J. M.; Klinger, A. L.; Yarian, C. S.; Keelara, V.; Ackers, G. K. Asymmetric Distribution of Cooperativity in the Binding Cascade of Normal Human Hemoglobin. 1. Cooperative and Noncooperative Oxygen Binding in Zn-Substituted Hemoglobin. *Biochemistry* **2005**, *44*, 11925–11938.

(12) Jeoung, J.-H.; Dobbek, H. Carbon Dioxide Activation at the Ni,Fe-Cluster of Anaerobic Carbon Monoxide Dehydrogenase. *Science* **2007**, *318*, 1461–1464.

(13) Yao, Q.; Peng, D.-C. Nitrite Oxidizing Bacteria (NOB) Dominating in Nitrifying Community in Full-Scale Biological Nutrient Removal Wastewater Treatment Plants. *AMB Express* **2017**, *7*.

(14) Borovik, A. S. Bioinspired Hydrogen Bond Motifs in Ligand Design: The Role of Noncovalent Interactions in Metal Ion Mediated Activation of Dioxygen. *Acc. Chem. Res.* **2005**, *38*, 54–61.

(15) Vallee, B. L.; Williams, R. J. Metalloenzymes: The Entatic Nature of Their Active Sites. *Proc. Natl. Acad. Sci. U. S. A.* **1968**, *59*, 498–505.

(16) Lothian, A.; Hare, D. J.; Grimm, R.; Ryan, T. M.; Masters, C. L.; Roberts, B. R. Metalloproteomics: Principles, Challenges and Applications to Neurodegeneration. *Front Aging Neurosci* **2013**, *5*.

(17) Ibers, J.; Holm, R. Modeling Coordination Sites in Metallobiomolecules. *Science* **1980**, *209*, 223–235.

(18) Lippard, S. J.; Berg, J. M. *Principles of Bioinorganic Chemistry*; University Science Books: Mill Valley, Calif, 1994.

(19) Schilter, D.; Camara, J. M.; Huynh, M. T.; Hammes-Schiffer, S.; Rauchfuss, T. B. Hydrogenase Enzymes and Their Synthetic Models: The Role of Metal Hydrides. *Chem. Rev.* **2016**, *116*, 8693–8749.

(20) Darensbourg, M. Y.; Lyon, E. J.; Zhao, X.; Georgakaki, I. P. The Organometallic Active Site of [Fe]Hydrogenase: Models and Entatic States. *Proc. Natl. Acad. Sci. U. S. A.* **2003**, *100*, 3683–3688.

(21) Shook, R. L.; Borovik, A. S. Role of the Secondary Coordination Sphere in Metal-Mediated Dioxygen Activation. *Inorg. Chem.* **2010**, *49*, 3646–3660.

(22) Moore, C. M.; Szymczak, N. K. Redox-Induced Fluoride Ligand Dissociation Stabilized by Intramolecular Hydrogen Bonding. *Chem. Comm.* **2015**, *51*, 5490–5492.

(23) Matson, E. M.; Bertke, J. A.; Fout, A. R. Isolation of Iron(II) Aqua and Hydroxyl Complexes Featuring a Tripodal H-Bond Donor and Acceptor Ligand. *Inorg. Chem.* **2014**, *53*, 4450–4458.

(24) Blackman, A. G. The Coordination Chemistry of Tripodal Tetraamine Ligands. *Polyhedron* **2005**, *24*, 1–39.

(25) Ford, C. L.; Park, Y. J.; Matson, E. M.; Gordon, Z.; Fout, A. R. A Bioinspired Iron Catalyst for Nitrate and Perchlorate Reduction. *Science* **2016**, *354*, 738–741.

(26) Gibson, V. C.; Spitzmesser, S. K. Advances in Non-Metallocene Olefin Polymerization Catalysis. *Chem. Rev.* **2003**, *103*, 283–316.

(27) Bart, S. C.; Chłlopek, K.; Bill, E.; Bouwkamp, M. W.; Lobkovsky, E.; Neese, F.; Wieghardt, K.; Chirik, P. J. Electronic Structure of Bis(Imino)Pyridine Iron Dichloride, Monochloride, and

Neutral Ligand Complexes: A Combined Structural, Spectroscopic, and Computational Study. *J. Am. Chem. Soc.* **2006**, *128*, 13901–13912.

(28) Kendall, A. J.; Zakharov, L. N.; Gilbertson, J. D. Synthesis and Stabilization of a Monomeric Iron(II) Hydroxo Complex via *Intra* Molecular Hydrogen Bonding in the Secondary Coordination Sphere. *Inorg. Chem.* **2010**, *49*, 8656–8658.

(29) Kwon, Y. M.; Delgado, M.; Zakharov, L. N.; Seda, T.; Gilbertson, J. D. Nitrite Reduction by a Pyridinediimine Complex with a Proton-Responsive Secondary Coordination Sphere. *Chem. Comm.* **2016**, *52*, 11016–11019.

(30) Thammavongsy, Z.; Seda, T.; Zakharov, L. N.; Kaminsky, W.; Gilbertson, J. D. Ligand-Based Reduction of CO_2 and Release of CO on Iron(II). *Inorg. Chem.* **2012**, *51*, 9168–9170.

(31) Stein, L. Y.; Klotz, M. G. The Nitrogen Cycle. *Curr. Biol.* **2016**, *26*, R94–R98.

(32) Shaver, M. P.; Fryzuk, M. D. Activation of Molecular Nitrogen: Coordination, Cleavage and Functionalization of N2 Mediated By Metal Complexes. *Adv. Synth. Catal.* **2003**, *345*, 1061–1076.

(33) Hill, R. D.; Rinker, R. G.; Wilson, H. D. Atmospheric Nitrogen Fixation by Lightning. *J. Atmos. Sci.* **1980**, *37*, 179–192.

(34) Huntrieser, H.; Schlager, H.; Roiger, A.; Lichtenstern, M.; Schumann, U.; Kurz, C.; Brunner, D.; Schwierz, C.; Richter, A.; Stohl, A. Lightning-Produced NOx over Brazil during TROCCINOX: Airborne Measurements in Tropical and Subtropical Thunderstorms and the Importance of Mesoscale Convective Systems. *Atmos. Chem. Phys.* **2007**, 27.

(35) *Micro-Organisms in Action: Concepts and Applications in Microbial Ecology*, 2nd ed.; Lynch, J. M., Hobbie, J. E., Eds.; Blackwell Scientific Publications: Oxford [England] ; Boston, 1988.

(36) Canfield, D. E.; Glazer, A. N.; Falkowski, P. G. The Evolution and Future of Earth's Nitrogen Cycle. *Science* **2010**, *330*, 192–196.

(37) Raymond, J.; Siefert, J. L.; Staples, C. R.; Blankenship, R. E. The Natural History of Nitrogen Fixation. *Mol. Biol. Evol.* **2004**, *21*, 541–554.

(38) Hatzenpichler, R. Diversity, Physiology, and Niche Differentiation of Ammonia-Oxidizing Archaea. *Appl. Environ. Microbiol.* **2012**, *78*, 7501–7510.

(39) Xu, G.; Fan, X.; Miller, A. J. Plant Nitrogen Assimilation and Use Efficiency. *Annu Rev Plant Biol* **2012**, *63*, 153–182.

(40) King, A. M.; Boyle, D.; Jensen, V. B.; Fogg, G. E.; Harter, T. Report for the State Water Resources Control Board Report to the Legislature. 61.

(41) Judd, E. T.; Stein, N.; Pacheco, A. A.; Elliott, S. J. Hydrogen Bonding Networks Tune Proton-Coupled Redox Steps during the Enzymatic Six-Electron Conversion of Nitrite to Ammonia. *Biochemistry* **2014**, *53*, 5638–5646.

(42) Li, Y.; Hodak, M.; Bernholc, J. Enzymatic Mechanism of Copper-Containing Nitrite Reductase. *Biochemistry* **2015**, *54*, 1233–1242.

(43) Scheidt, W. R.; Duval, H. F.; Neal, T. J.; Ellison, M. K. Intrinsic Structural Distortions in Five-Coordinate (Nitrosyl)Iron(II) Porphyrinate Derivatives. *J. Am. Chem. Soc.* **2000**, *122*, 4651–4659.

(44) Nasri, H.; Ellison, M. K.; Chen, S.; Huynh, B. H.; Scheidt, W. R. Sharing the π-Bonding. An Iron Porphyrin Derivative with Trans, π-Accepting Axial Ligands. Synthesis, EPR and Mössbauer Spectra, and Molecular Structure of Two Forms of the Complex Nitronitrosyl(α,α,α,α-Tetrakis(*o*-Pivalamidophenyl)-Porphinato)Ferrate(II). *J. Am. Chem. Soc.* **1997**, *119*, 6274–6283.

(45) Wyllie, G. R. A.; Scheidt, W. R. Solid-State Structures of Metalloporphyrin NO_x Compounds. *Chem. Rev.* **2002**, *102*, 1067–1090.

(46) Einsle, O.; Messerschmidt, A.; Huber, R.; Kroneck, P. M. H.; Neese, F. Mechanism of the Six-Electron Reduction of Nitrite to Ammonia by Cytochrome *c* Nitrite Reductase. *J. Am. Chem. Soc.* **2002**, *124*, 11737–11745.

(47) Silaghi-Dumitrescu, R. Linkage Isomerism in Nitrite Reduction by Cytochrome Cd_1 Nitrite Reductase. *Inorg. Chem.* **2004**, *43*, 3715–3718.

(48) McEvoy, J. P.; Brudvig, G. W. Water-Splitting Chemistry of Photosystem II. *Chem. Rev.* **2006**, *106*, 4455–4483.

(49) Umena, Y.; Kawakami, K.; Shen, J.-R.; Kamiya, N. Crystal Structure of Oxygen-Evolving Photosystem II at a Resolution of 1.9 Å. *Nature* **2011**, *473*, 55–60.

(50) Vrettos, J. S.; Limburg, J.; Brudvig, G. W. Mechanism of Photosynthetic Water Oxidation: Combining Biophysical Studies of Photosystem II with Inorganic Model Chemistry. *Biochim. Biophys. Acta, Bioenerg.* **2001**, *1503*, 229–245.

(51) Tsui, E. Y.; Tran, R.; Yano, J.; Agapie, T. Redox-Inactive Metals Modulate the Reduction Potential in Heterometallic Manganese-Oxido Clusters. *Nat. Chem.* **2013**, *5*, 293–299.

(52) Bakou, A.; Ghanotakis, D. F. Substitution of Lanthanides at the Calcium Site(s) in Photosystem II Affects Electron Transport from Tyrosine Z to P680+. *Biochim. Biophys. Acta, Bioenerg.* **1993**, *1141*, 303–308.

(53) Beer, P. D. Transition Metal and Organic Redox-Active Macrocycles Designed to Electrochemically Recognize Charged and Neutral Guest Species. In *Advances in Inorganic Chemistry*; Elsevier, 1992; Vol. 39, pp 79–157.

(54) Reath, A. H.; Ziller, J. W.; Tsay, C.; Ryan, A. J.; Yang, J. Y. Redox Potential and Electronic Structure Effects of Proximal Nonredox Active Cations in Cobalt Schiff Base Complexes. *Inorg. Chem.* **2017**, *56*, 3713–3718.

(55) Cammarota, R. C.; Lu, C. C. Tuning Nickel with Lewis Acidic Group 13 Metalloligands for Catalytic Olefin Hydrogenation. *J. Am. Chem. Soc.* **2015**, *137*, 12486–12489.

(56) Gibson, V. C.; Redshaw, C.; Solan, G. A. Bis(Imino)Pyridines: Surprisingly Reactive Ligands and a Gateway to New Families of Catalysts. *Chem. Rev.* **2007**, *107*, 1745–1776.

(57) Addison, A. W.; Rao, T. N.; Reedijk, J.; van Rijn, J.; Verschoor, G. C. Synthesis, Structure, and Spectroscopic Properties of Copper(II) Compounds Containing Nitrogen–sulphur Donor Ligands; the Crystal and Molecular Structure of Aqua[1,7-Bis(N-Methylbenzimidazol-2'-Yl)-2,6-Dithiaheptane]Copper(II) Perchlorate. *J. Chem. Soc., Dalton Trans.* **1984**, No. 7, 1349–1356.

(58) Evans, D. F. A New Type of Magnetic Balance. *J. Phys. E: Sci. Instrum.* **1974**, *7*, 247–249.

(59) Blake, E. T.; Cashman, P. J.; Thornton, J. I. Determination of Magnetic Moments in Solution by Nuclear Magnetic Resonance Spectrometry. *Anal. Chem.* **1973**, *45*, 367–369.

(60) Britovsek, G. J. P.; Clentsmith, G. K. B.; Gibson, V. C.; Goodgame, D. M. L.; McTavish, S. J.; Pankhurst, Q. A. The Nature of the Active Site in Bis(Imino)Pyridine Iron Ethylene Polymerisation Catalysts. *Catal. Commun.* **2002**, *3*, 207–211.

(61) Berben, L. A. Catalysis by Aluminum(III) Complexes of Non-Innocent Ligands. *Chem. Eur. J. 21*, 2734–2742.

(62) Atkins, P. W. *Shriver & Atkins' Inorganic Chemistry*; W.H. Freeman and Co.: New York, 2010.

(63) Delgado, M.; Ziegler, J. M.; Seda, T.; Zakharov, L. N.; Gilbertson, J. D. Pyridinediimine Iron Complexes with Pendant Redox-Inactive Metals Located in the Secondary Coordination Sphere. *Inorg. Chem.* **2016**, *55*, 555–557.

(64) Bindfit http://app.supramolecular.org/bindfit/.

(65) Fielding, L. Determination of Association Constants (Ka) from Solution NMR Data. *Tetrahedron* **2000**, *56*, 6151–6170.

(66) Hou, Y. C.; Janczuk, A.; Wang, P. G. Current Trends in the Development of Nitric Oxide Donors. *Curr. Pharm. Des.* **1999**, *5*, 417–441.

(67) Pulukkody, R.; Darensbourg, M. Y. Synthetic Advances Inspired by the Bioactive Dinitrosyl Iron Unit. *Acc. Chem. Res.* **2015**, *48*, 2049–2058.

(68) Matson, E. M.; Park, Y. J.; Fout, A. R. Facile Nitrite Reduction in a Non-Heme Iron System: Formation of an Iron(III)-Oxo. *J. Am. Chem. Soc.* **2014**, *136*, 17398–17401.

(69) Delgado, M.; Gilbertson, J. D. Ligand-Based Reduction of Nitrate to Nitric Oxide Utilizing a Proton-Responsive Secondary Coordination Sphere. *Chem. Comm.* **2017**, *53*, 11249–11252.

(70) Kwon, Y. Synthesis & Reactivity of Iron (II) Pyridinediimine Complexes For the Reduction of Nitrite, 2016.

(71) Gans, P.; Sabatini, A.; Sacconi, L. Infrared Spectra and Bonding in Transition Metal Nitrosyl Complexes. *Inorg. Chem.* **1966**, *5*, 1877–1881.

(72) Tsai, M.-L.; Tsou, C.-C.; Liaw, W.-F. Dinitrosyl Iron Complexes (DNICs): From Biomimetic Synthesis and Spectroscopic Characterization toward Unveiling the Biological and Catalytic Roles of DNICs. *Acc. Chem. Res.* **2015**, *48*, 1184–1193.

(73) Ye, S.; Neese, F. The Unusual Electronic Structure of Dinitrosyl Iron Complexes. *J. Am. Chem. Soc.* **2010**, *132*, 3646–3647.

(74) Enemark, J. H.; Feltham, R. D. Principles of Structure, Bonding, and Reactivity for Metal Nitrosyl Complexes. *Coord. Chem. Rev.* **1974**, *13*, 339–406.

(75) Uyeda, C.; Peters, J. C. Selective Nitrite Reduction at Heterobimetallic CoMg Complexes. *J. Am. Chem. Soc.* **2013**, *135*, 12023–12031.

(76) Burns, K. T.; Marks, W. R.; Cheung, P. M.; Seda, T.; Zakharov, L. N.; Gilbertson, J. D. Uncoupled Redox-Inactive Lewis Acids in the Secondary Coordination Sphere Entice Ligand-Based Nitrite Reduction. *Inorg. Chem.* **2018**.

(77) Haas, R. M.; Hern, Z.; Sproules, S.; Hess, C. R. An Unsymmetric Ligand Framework for Noncoupled Homo- and Heterobimetallic Complexes. *Inorg. Chem.* **2017**, *56*, 14738–14742.

(78) Brown, E. C.; Johnson, B.; Palavicini, S.; Kucera, B. E.; Casella, L.; Tolman, W. B. Modular Syntheses of Multidentate Ligands with Variable N-Donors: Applications to Tri- and Tetracopper(i) Complexes. *Dalton Trans.* **2007**, No. 28, 3035.

(79) Jones, M. B.; MacBeth, C. E. Tripodal Phenylamine-Based Ligands and Their Co^{II} Complexes. *Inorg. Chem.* **2007**, *46*, 8117–8119.

(80) Dedieu, A. *Transition Metal Hydrides*; Wiley-VCH: New York; Chichester, 1992.

(81) Lohr, T. L.; Marks, T. J. Orthogonal Tandem Catalysis. *Nat. Chem.* **2015**, *7*, 477–482.

(82) DuBois, D. L.; Blake, D. M.; Miedaner, A.; Curtis, C. J.; DuBois, M. R.; Franz, J. A.; Linehan, J. C. Hydride Transfer from Rhodium Complexes to Triethylborane. *Organometallics* **2006**, *25*, 4414–4419.

(83) Mock, M. T.; Potter, R. G.; O'Hagan, M. J.; Camaioni, D. M.; Dougherty, W. G.; Kassel, W. S.; DuBois, D. L. Synthesis and Hydride Transfer Reactions of Cobalt and Nickel Hydride Complexes to BX_3 Compounds. *Inorg. Chem.* **2011**, *50*, 11914–11928.

(84) Knopf, I.; Cummins, C. C. Revisiting CO_2 Reduction with $NaBH_4$ under Aprotic Conditions: Synthesis and Characterization of Sodium Triformatoborohydride. *Organometallics* **2015**, *34*, 1601–1603.

(85) Wiedner, E. S.; Chambers, M. B.; Pitman, C. L.; Bullock, R. M.; Miller, A. J. M.; Appel, A. M. Thermodynamic Hydricity of Transition Metal Hydrides. *Chem. Rev.* **2016**, *116*, 8655–8692.

(86) Curtis, C. J.; Miedaner, A.; Ellis, W. W.; DuBois, D. L. Measurement of the Hydride Donor Abilities of $[HM(Diphosphine)_2^+$ Complexes (M = Ni, Pt) by Heterolytic Activation of Hydrogen. *J. Am. Chem. Soc.* **2002**, *124*, 1918–1925.

(87) Jeletic, M. S.; Helm, M. L.; Hulley, E. B.; Mock, M. T.; Appel, A. M.; Linehan, J. C. A Cobalt Hydride Catalyst for the Hydrogenation of CO_2: Pathways for Catalysis and Deactivation. *ACS Catal.* **2014**, *4*, 3755–3762.

(88) Crugeiras, J.; Rios, A.; Riveiros, E.; Richard, J. P. Substituent Effects on Electrophilic Catalysis by the Carbonyl Group: Anatomy of the Rate Acceleration for PLP-Catalyzed Deprotonation of Glycine. *J. Am. Chem. Soc.* **2011**, *133*, 3173–3183.

(89) Miller, A. J. M.; Labinger, J. A.; Bercaw, J. E. Trialkylborane-Assisted CO_2 Reduction by Late Transition Metal Hydrides. *Organometallics* **2011**, *30*, 4308–4314.

(90) Cheung, P. M.; Berger, R.; Zakharov, L. N.; Gilbertson, J. D. Square Planar Cu(I) Stabilized by a Pyridinediimine Ligand. *Chem. Commun.* No. 52, 4156–4159.

(91) Esteruelas, M. A.; López, A. M.; Méndez, L.; Oliván, M.; Oñate, E. Preparation, Structure, and Ethylene Polymerization Behavior of Bis(Imino)Pyridyl Chromium(III) Complexes. *Organometallics* **2003**, *22*, 395–406.

(92) Bianchini, C.; Mantovani, G.; Meli, A.; Migliacci, F.; Zanobini, F.; Laschi, F.; Sommazzi, A. Oligomerisation of Ethylene to Linear α-Olefins by New Cs- and C1-Symmetric [2,6-Bis(Imino)Pyridyl]Iron and -Cobalt Dichloride Complexes. *Eur. J. Inorg. Chem. 2003*, 1620–1631.